



<https://theses.gla.ac.uk/>

Theses Digitisation:

<https://www.gla.ac.uk/myglasgow/research/enlighten/theses/digitisation/>

This is a digitised version of the original print thesis.

Copyright and moral rights for this work are retained by the author

A copy can be downloaded for personal non-commercial research or study, without prior permission or charge

This work cannot be reproduced or quoted extensively from without first obtaining permission in writing from the author

The content must not be changed in any way or sold commercially in any format or medium without the formal permission of the author

When referring to this work, full bibliographic details including the author, title, awarding institution and date of the thesis must be given

Enlighten: Theses

<https://theses.gla.ac.uk/>
research-enlighten@glasgow.ac.uk

ELECTRON MICROSCOPE STUDIES of ORGANIC CRYSTALS

by

CATHERINE HELEN McCONNELL

A thesis submitted for the degree of
Doctor of Philosophy
to the Department of Chemistry
of the University of Glasgow

SEPTEMBER, 1988.

© Catherine H. McConnell, 1988.

ProQuest Number: 10998196

All rights reserved

INFORMATION TO ALL USERS

The quality of this reproduction is dependent upon the quality of the copy submitted.

In the unlikely event that the author did not send a complete manuscript and there are missing pages, these will be noted. Also, if material had to be removed, a note will indicate the deletion.



ProQuest 10998196

Published by ProQuest LLC (2018). Copyright of the Dissertation is held by the Author.

All rights reserved.

This work is protected against unauthorized copying under Title 17, United States Code
Microform Edition © ProQuest LLC.

ProQuest LLC.
789 East Eisenhower Parkway
P.O. Box 1346
Ann Arbor, MI 48106 – 1346

ACKNOWLEDGEMENTS.

I would like to express my thanks to Dr. John Fryer, my Supervisor at the University of Glasgow, for all his advice and encouragement throughout the course of my research. Thanks are also due to Dr. Tom Baird and to my colleagues and friends in the Electron Microscopy group for many interesting and helpful discussions, and to David Thom for technical assistance.

I am very grateful for having had the opportunity of carrying out part of my work at the Fritz-Haber-Institut der Max-Planck-Gesellschaft in Berlin, and would like to thank Prof. Elmar Zeitler for allowing me the use of the facilities at the F.H.I. and for his interest in my work. Others at the Institut whose advice and assistance are greatly appreciated are: Dr. F. Zemlin, Herr E. Beckmann, Herr J. Jäger, Dr. M. van Heel and Dr. G. Harauz.

Warmest thanks to Dr. Douglas Dorset for his enthusiastic advice concerning the "Paraffin" section of this thesis, and for three enjoyable weeks spent working in his laboratory at the Medical Foundation of Buffalo.

Lastly, I gratefully acknowledge the work put into this thesis by my parents, Jean and Sandy McConnell, who typed and proof-read it meticulously.

SUMMARY.

This thesis is arranged in two parts; after an introductory chapter on the theory of image formation in the electron microscope, Chapters 2 to 5 are concerned with the problem of radiation damage to the specimen in the microscope, and Chapters 6 and 7 describe studies of crystalline paraffins by electron microscopy.

Radiation damage to the specimen has long been recognised as a major hindrance to image-formation and diffraction studies in electron microscopy, especially of organic and biological material. Changes may occur in the structure of the specimen under the beam, leading to a false picture of the material, or the structure may be destroyed altogether before any detail can be recorded.

Among the methods commonly used to counteract radiation damage are: cooling the specimen stage of the microscope in the hope of "freezing in" severed radicals, using minimum dose techniques in combination with image processing to extract information from low-contrast negatives, and coating the specimen with a thin layer of an amorphous conducting material such as evaporated carbon.

In this study, the effect of combining some of these techniques is investigated, in particular the protective effect of an encapsulating carbon coat at various temperatures - room temperature down to 10K.

A group of compounds which is highly sensitive to radiation damage is that of the crystalline paraffins. An understanding of the behaviour of long-chain paraffins may be important to the elucidation of the structures of some polymers and biological lipids, especially when the effect of the presence of chains of more than one length is taken into account.

In the second section of the thesis, high resolution images have been taken of crystals of pure paraffins and of their solid solutions, in two orientations: the long axis may be viewed directly at room temperature, but image processing has been applied to the projection of the small (ab) unit cell face. Defects in the crystal lattice planes have been observed, and the variation in the interlamellar spacing according to the composition of solid solutions has been measured.

TABLE of CONTENTS.

ACKNOWLEDGEMENTS.

SUMMARY.

	<u>Page No</u>
<u>CHAPTER 1:</u> Introduction. The Transmission Electron Microscope.	1
1.1 The Development of the Electron Microscope.	2
1.2 Applications.	3
1.3 The Lens System, and the Electron Gun.	4
1.4 Coherence.	6
1.5 The Scattering of Electrons.	14
1.6 The Microscope as an Electron Diffraction Camera.	17
1.7 Electron Crystallography.	19
 <u>CHAPTER 2:</u> Radiation Damage.	 23
2.1 Transfer of Energy to the Specimen.	24
2.2 Secondary Processes in the Specimen.	34
2.3 Detection and Measurement of Radiation Damage.	39
2.4 Reduction of Radiation Damage in the Electron Microscope.	47
 <u>CHAPTER 3:</u> Experimental Techniques.	 57
3.1 Microscopes Used in Room Temperature and Low Temperature Studies.	58
3.2 The Minimum Dose System (MDS).	59
3.3 Densitometry and Digitisation of Images.	61
3.4 Image Processing.	62
3.5 The Optical Bench.	67

TABLE of CONTENTS (Contd.)

<u>CHAPTER 4:</u>	Epitaxial Preparation of Specimens.	69
4.1	Epitaxy	70
4.2	Preparation of Epitaxial Films by Evaporation.	72
4.3	Thickness Measurement of Epitaxial Films in the "Deeko 250" Microscope.	75
4.4	Preparation of Paraffin Specimens.	77
<u>CHAPTER 5:</u>	Radiation Damage Results and Discussion.	83
5.1	Radiation Damage Measurements at Room Temperature.	84
5.2	Extinction Dose Results for Metal-Free Phthalocyanine.	85
5.3	Extinction Dose Results for Coronene and Ovalene.	88
5.4	Results of Extinction Dose Measurements at Very Low Temperatures (<15K)	92
5.5	Radiation Damage Results from the Variable-Temperature Electron Microscope "Deeko 250".	94
5.6	Calculation of D_e for Metal-Free Phthalocyanine.	99
5.7	The Dependence of Radiation Sensitivity on the Number of Layers in a Langmuir-Blodgett Film.	102
<u>CHAPTER 6:</u>	The Paraffins - Introduction.	104
6.1	Growth of Paraffin Crystals.	105
6.2	Packing Behaviour of Paraffins.	107
6.3	Solid Solutions.	117
6.4	Vegard's Law.	121

TABLE of CONTENTS (Contd.)

CHAPTER 7:	The Paraffins - Results and Discussion.	123
7.1	Low Magnification Images of Paraffins in the $hk0$ Orientation.	124
7.2	High Resolution Electron Microscopy of Paraffins in the $hk0$ Orientation.	125
7.3	Image Processing of Paraffins ($hk0$ Orientation)	128
7.4	Fourier Reconstructions of Paraffins in the $0kl$ Orientation.	130
7.5	High Resolution Imaging of Paraffins in the $0kl$ Orientation.	133
	(i) The Pure Paraffins.	134
	(ii) Solid Solutions.	136
7.6	Changes in Lattice Spacings of Solid Solutions of Paraffins.	142
CHAPTER 8:	Conclusions.	147
8.1	Radiation Damage.	148
8.2	The Paraffins.	149
REFERENCES		152

CHAPTER 1 - INTRODUCTION:

The Transmission Electron Microscope.

- 1.1 The Development of the Electron Microscope.
- 1.2 Applications.
- 1.3 The Lens System, and the Electron Gun.
- 1.4 Coherence.
- 1.5 The Scattering of Electrons.
- 1.6 The Microscope as an Electron Diffraction Camera.
- 1.7 Electron Crystallography.

1. INTRODUCTION: THE TRANSMISSION ELECTRON MICROSCOPE.

1.1 The Development of the Electron Microscope.

The electron microscope is analogous to the light microscope in that it consists of a source of radiation, a specimen-stage and a series of lenses to magnify and project an image of the scattered beams coming from the specimen. In the nineteenth century, Abbe realised that the resolution of the optical microscope was limited by the wavelength of light; the resolution limit is not sharp but is approximately equal to $k \lambda / A$ where k is a constant, λ is the wavelength of the illumination and A is the numerical aperture of the objective lens. For illumination by visible light, the smallest resolvable object is about 200 nm; however, during the first decades of the 20th century discoveries were made which led to the invention of a microscope which exploited radiation of a shorter wavelength than light and was therefore capable of much higher resolution.

In 1924 de Broglie formulated the relationship between a particle's momentum and its wavelength; two years later Schrödinger published his equation completely describing the wave properties of matter. In 1927 Davisson and Germer showed that, like X-rays, electrons were diffracted by single crystals of nickel, and in the same year Busch demonstrated experimentally that it was possible to construct a magnetic lens for the focussing of electrons.

In 1932 Max Knoll and Ernst Ruska built their first Transmission Electron Microscope at the Technische Hochschule, Berlin (Knoll & Ruska 1932), and a year later achieved a resolution surpassing that of the light microscope (5nm, Ruska, 1934). The instrument has been developed over 50 years to the point where atomic resolution may be achieved with suitable specimens, and it is even possible to observe the movement of columns of gold atoms at the edge of a gold single crystal - a video camera attached to the microscope permits recording (Bovin et al 1985).

1.2 Applications.

The technique of electron microscopy may be applied to many different kinds of specimens, for example negatively-stained biological membranes, thin sections of metallurgical specimens, metal oxides and other inorganic materials, cokes and carbons, and organic crystals (details of the methods involved are given in Kay 1965).

This project deals with organic crystals, and the microscopy of these involves special problems. The irradiation of crystals by electrons with the high energies generated in the electron microscope causes damage to most materials in time but the damage inflicted on organic crystals can destroy their structure even in the short time it takes to choose an area of specimen, bring it into focus and record an image. Consequently

the micrograph must be taken at the minimum possible electron dose while still allowing sufficient electrons to interact with the specimen and with the photographic emulsion to extract the maximum possible amount of information. This will be discussed further in the chapter on radiation damage.

A careful choice must therefore be made of beam current, aperture sizes, magnification, exposure time and type of photographic emulsion used, in order to obtain the optimum amount of information on the film. Optical densitometry and image processing facilities can extract information from noisy images by various methods, and this reduces the necessary exposure of the specimen to the electrons during recording. In addition, modern microscopes often have a facility which allows a suitable area to be selected by observation of its diffraction pattern, then an adjacent area is used for focussing and astigmatism correction. The beam only returns to the chosen area when the camera shutter opens, thus exposing the crystal only while the recording is being made. The amount of defocus can be checked afterwards. A more detailed description of these techniques is given in Section 3.2.

1.3 The Lens System and the Electron Gun.

A schematic diagram of a conventional Transmission Electron Microscope is shown in Fig. 1.1, and ray diagrams for the transmission image and diffraction modes in Fig. 1.2.

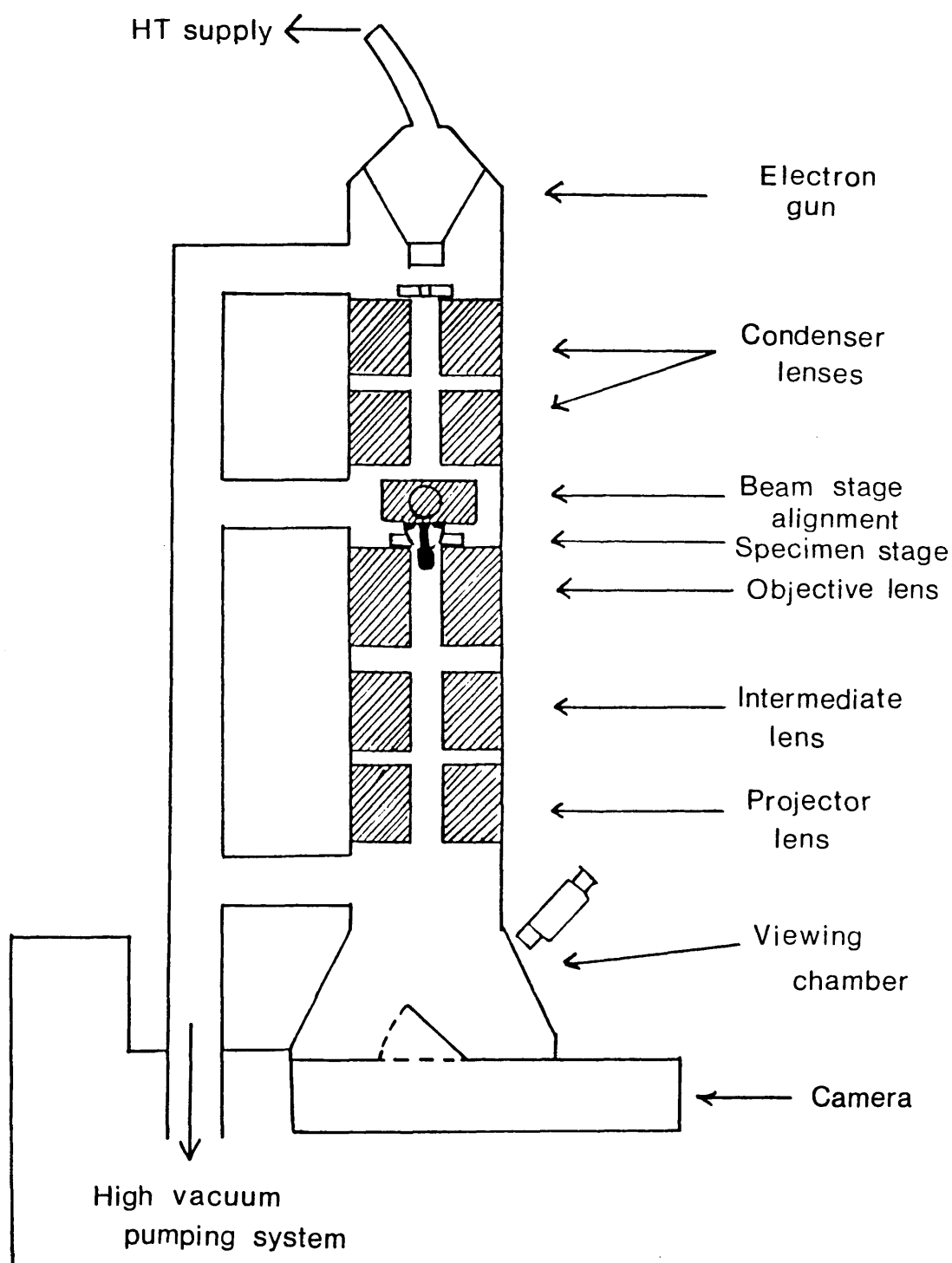


Fig. 1.1: Arrangement of Lenses in the Electron Microscope.
(after Watt 1985)

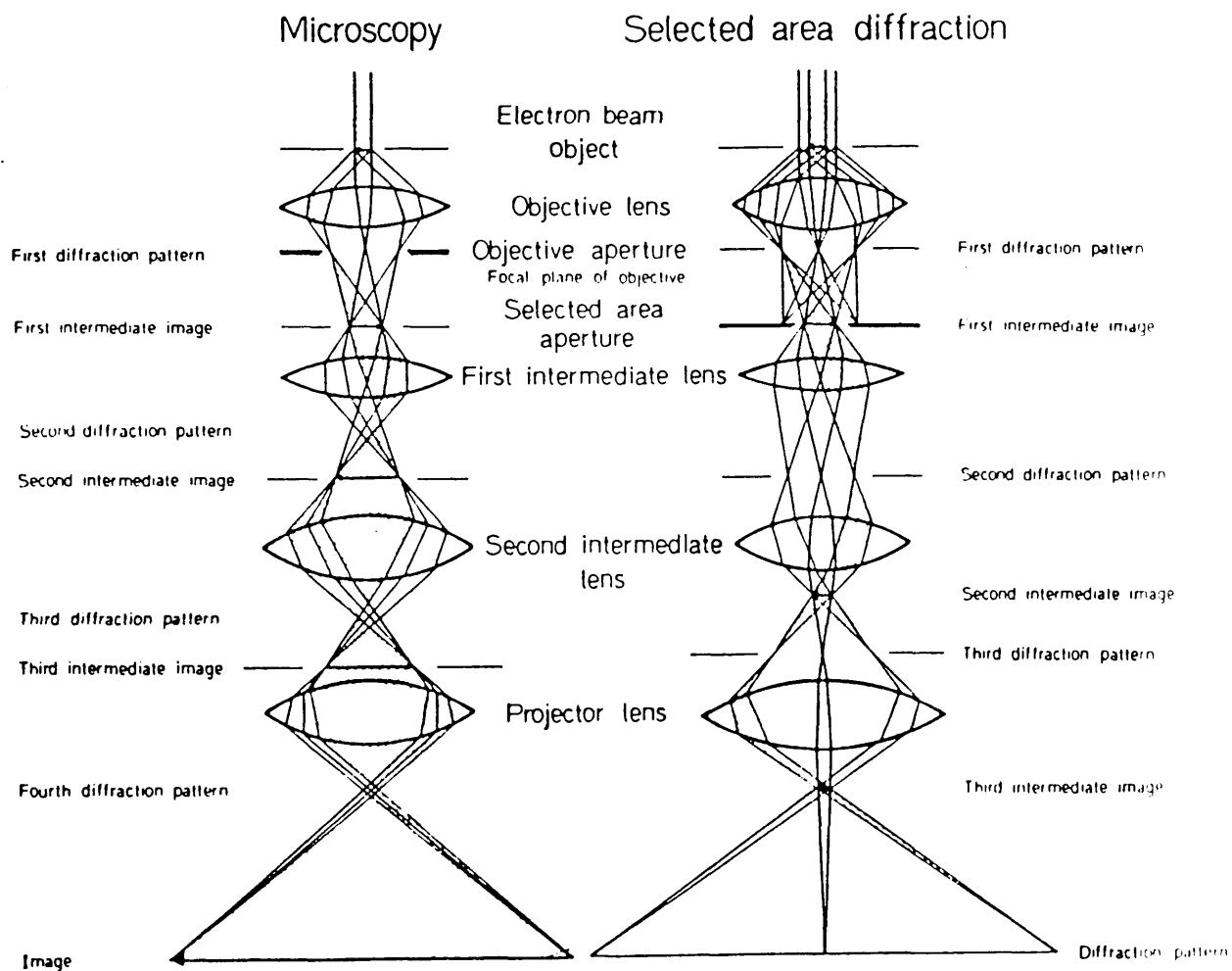


Fig. 1.2: Ray diagrams for the Transmission and Diffraction Modes of the Electron Microscope.

The microscope consists of a long column continuously evacuated by means of rotary and diffusion pumps to a pressure of 10^{-6} torr or less. Electrons are accelerated from the gun at the top of the column towards an anode at earth potential. A typical accelerating voltage for a commercial microscope is 100 kV, but microscopes of 200 or 500 kV are becoming increasingly more common, and microscopes have been built with up to 3 MeV accelerating potential.

Having passed through an aperture in the anode, the electron beam is then collimated by the condenser system, which consists of an aperture to allow only the coherent electrons in the centre of the beam to pass by, and two or more condenser lenses. The electrons then interact with the specimen. The undeflected beam, together with electrons scattered elastically by the specimen, is then collected and magnified by the objective lens. Further magnification (up to $10^6\times$) is effected by the projector lens(es) and the final image is projected on to a fluorescent screen which may be raised to expose a photographic plate.

The electron gun is commonly a tungsten hairpin filament, but a lanthanum hexaboride filament can give improved coherence and a source brightness which is higher by a factor of 10 (Ahmed 1971). A field emission source, consisting of a single crystal

tungsten wire, has a brightness a hundred times greater than the LaB_6 filament, but requires a surrounding vacuum of 10^{-10} torr. Two important features of the electron source are its brightness and its coherence. Brightness is defined as the current density per unit solid angle (Grundy & Jones, 1976) and is given by:

$$B = i_c / \pi \beta^2 \quad [1.1]$$

where i_c is the current density at the crossover (that is, the spot where the accelerated electrons are brought to a focus within the field of the electrodes) and β the semi-angular aperture. Substituting the Langmuir formula for the maximum value of i which can be focussed into a spot,

$$i = \frac{i_o e V \beta^2}{k T_o} \quad [1.2]$$

into equation [1.1] gives as maximum brightness

$$B = \frac{i_o e V}{\pi k T_o} \quad [1.3]$$

where V and T_o are the voltage and temperature of the filament and k is Boltzmann's constant.

1.4 Coherence.

The coherence of a source of electrons refers to the ability of the waves produced by it to interfere with each other. The

source in an electron microscope is taken to lie in the exit plane of the final condenser lens, coincident with the illuminating aperture, and each point in the aperture is taken to be a point source of electrons.

The spatial coherence width X_c is the width at the object plane which is irradiated by the coherent illumination. The scattered waves from two atoms separated by less than X_c therefore interfere and their complex amplitudes add to give a cosine-modulated atomic scattering factor. If the distance between the atoms is much greater than X_c no interference can occur as the electrons are scattered incoherently and the intensities add together linearly.

The theory of partial coherence describes the intermediate cases (Spence 1981).

The coherence width is related to θ_c , the semi-angle subtended by the beam at the specimen, by the expression:

$$X_c = \frac{\lambda}{2\pi\theta_c} \quad [1.4]$$

To obtain phase-contrast effect, θ_c must be chosen so that X_c is larger than the coarsest detail of interest in the specimen. When this condition is met, images can be formed with optimum contrast at the Scherzer focus, defined in equation [1.16].

Elastic scattering is dependent upon the atomic number of the scattering object, and for crystalline materials it obeys the Bragg relationship

$$n\lambda = 2d \sin \theta \quad [1.5]$$

where d is the lattice spacing

θ is the angle of scattering

n is an integer

Elastic scattering gives rise to phase contrast which is very dependent on the diameter of the objective aperture, as this prevents widely-scattered beams from contributing to the image. For thick specimens elastic scattering may give rise to "deficiency contrast" where dark contrast is observed when the electrons are scattered too widely to pass through the aperture.

The total intensity transmitted can be written as

$$I = I_0 e^{-\sigma_s t} \quad [1.6]$$

where t is the specimen thickness

I_0 is the incident intensity

σ_s is the total scattering cross-section and is related to α_a the scattering cross-section for a single atom by:

$$\sigma_s = N \sigma_a = \frac{N_o \rho \sigma_a}{A} \quad [1.7]$$

where N is the number of atoms per unit volume,

N_o is Avogadro's number,

ρ is the density of the material and

A is the atomic weight of the atoms.

It follows that for an amorphous specimen, if $\sigma_s t$ is constant, no contrast will be observed, as the scattering intensities will be constant from every part of the specimen.

Inelastic scattering occurs when the electrons transfer part of their energy to the atoms of the specimen, undergoing a change in their own energy and hence their wavelength. The scattered waves contribute an out-of-focus background to the image which reduces the contrast of the elastic image. The variation in wavelength combines with other energy fluctuations in the electron microscope to form the chromatic aberration term of the transfer function.

If $\phi(x,y)$ is the projection in the beam direction of the potential distribution of a thin specimen, and $\sigma = \frac{\pi}{\lambda E}$ is the interaction constant, the transmission function $q(xy)$ may be written

$$q(xy) = e^{-i\sigma\phi(xy)} \quad [1.8]$$

The amplitude distribution of the Fraunhofer diffraction pattern in the back focal plane is represented by the Fourier Transform of equation (1), which is modified by a phase factor χ to account for the aberrations inevitably present in the objective lens.

$$\psi_{(u,v)} = \mathcal{F} \left[e^{-i\sigma\phi(xy)} \right] e^{i\chi_{(uv)}} \quad [1.9]$$

u and v are reciprocal space co-ordinates, where $u = x/f \lambda$ and $v = y/f \lambda$.

Where an objective aperture is present, equation [1.9] is further modified by an aperture function $A(u,v)$ which has a value of 1 inside the aperture and 0 outside it.

In equation [1.9],

$$\chi = \frac{2\pi}{\lambda} \left(\Delta f \frac{\alpha^2}{2} - C_s \frac{\alpha^4}{4} \right) \quad [1.10]$$

where α is the angle of scattering

C_s is the spherical aberration

constant

Δf is the amount of defocus

For thin, light-atom specimens, it is possible to make the approximation

$$q(xy) = 1 - i\sigma\phi_{(xy)} \quad [1.11]$$

and the net amplitude in the back focal plane is given by:

$$\psi_{(uv)} = \delta_{(uv)} + \sigma\phi_{(uv)} \sin\chi_{(uv)} - i\sigma\phi_{(uv)} \cos\chi_{(uv)} \quad [1.12]$$

This represents the sum of the transmitted beam (uv), and the amplitudes of the scattered beams (the complex terms). The amplitude at the image plane is given by the Fourier Transform of equation [1.12] which, in the absence of an aperture, is given by

$$\psi_{(xy)} = 1 + \mathcal{F}[\sigma\phi_{(uv)} \sin\chi_{(uv)}] - i\mathcal{F}[\sigma\phi_{(uv)} \cos\chi_{(uv)}] \quad [1.13]$$

The observed intensity of the image is then

$$I_{(xy)} = \psi\psi^* = 1 + 2\sigma\phi_{(xy)} * \mathcal{F}[\sin\chi_{(uv)}] \quad [1.14]$$

where $*$ represents a convolution integral.

For phase contrast imaging it is desirable that $\sin\chi$ should have a value near 1 for the range of periodicities to be resolved. Then the image intensity approximates to:

$$I = 1 + 2\sigma\phi_{(xy)} \quad [1.15]$$

$\sin \chi$ is called the contrast transfer function. It is oscillatory in nature and so has different values at different spatial frequencies; this means that on varying the defocus value, a lattice image of a certain periodicity will undergo variations in, or reversal of, contrast. Fig. 1.3 shows a plot of $\sin \chi$ against reciprocal periodicity $1/d \text{ \AA}^{-1}$ and it applies to a 100kV instrument with a high resolution pole-piece ($C_s = 0.67 \text{ mm}$), the JEOL 100C microscope used in part of this work. The diameter of the objective aperture limits the maximum angle of the scattered electrons which are permitted to contribute to the image. The optimum defocus value for normal applications of the microscope is that for which the transfer function value is constant and near unity over the desired range of spatial frequencies. This ensures that any observed periodic structure within the range is imaged without reversal of contrast. The optimum defocus value is given by

$$\Delta f' \doteq 1.2 \sqrt{C_s \lambda} \quad [1.16]$$

The way in which the range of spatial frequencies observable without contrast reversal is limited by the C_s value of the objective is illustrated in Fig. 1.4 in which the curves are plotted at the optimum defocus value in each case. Eisenhandler and Siegel (1966) calculated the Scherzer cut-off to be

$$d_{\min} = 0.65 C_s^{1/4} \lambda^{3/4} \quad [1.17]$$

Fig. 1.3: Phase Contrast Transfer Functions for a range of defocus values, $\Delta z = 0, 200 \text{ \AA}$ and 600 \AA underfocus with $\sim 50 \text{ }\mu\text{m}$ objective aperture cut-off.

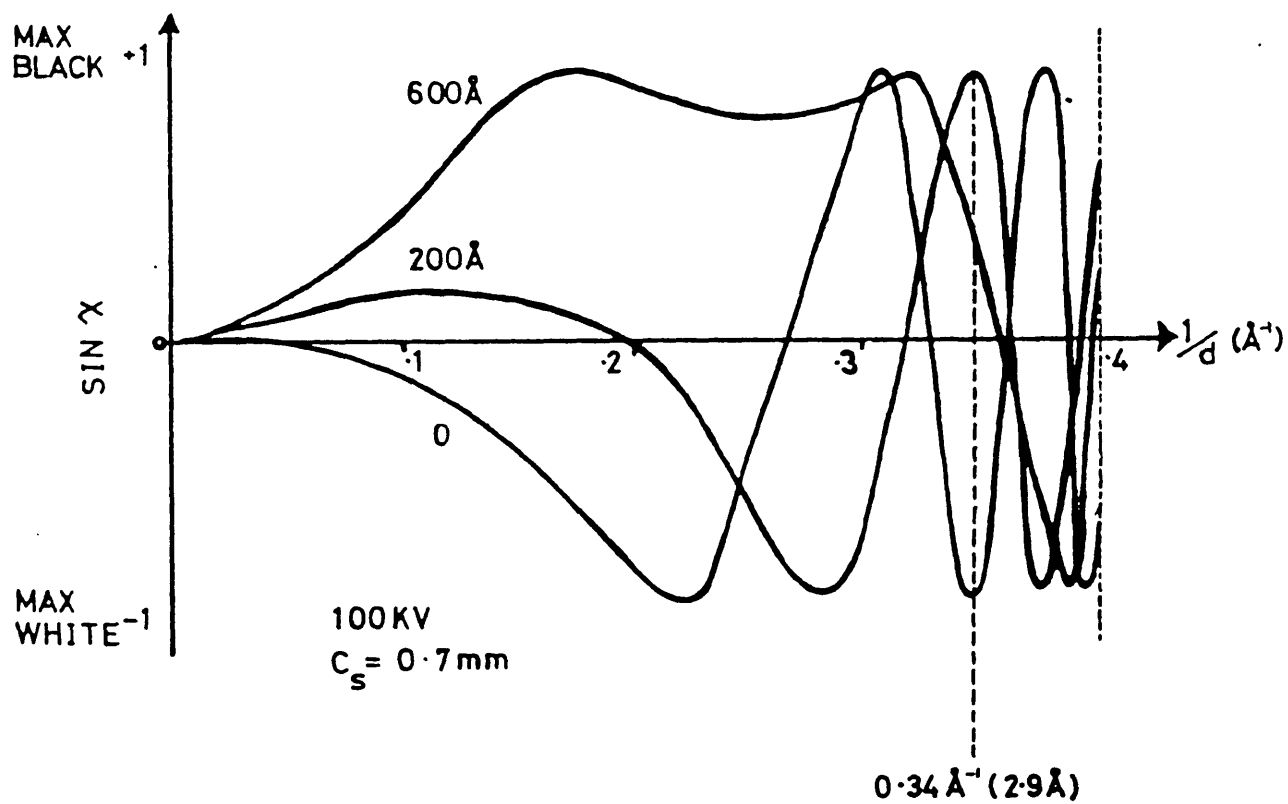
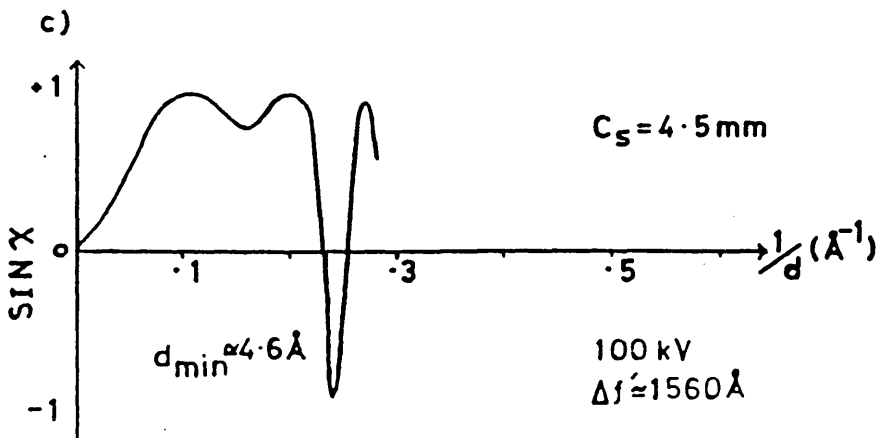
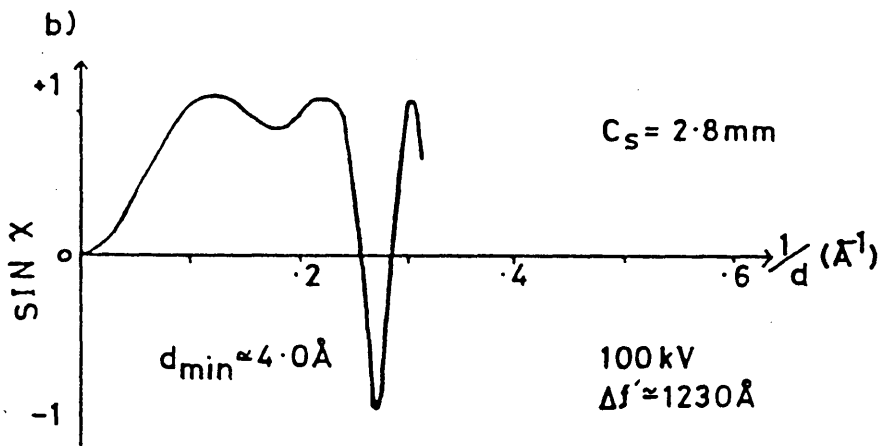
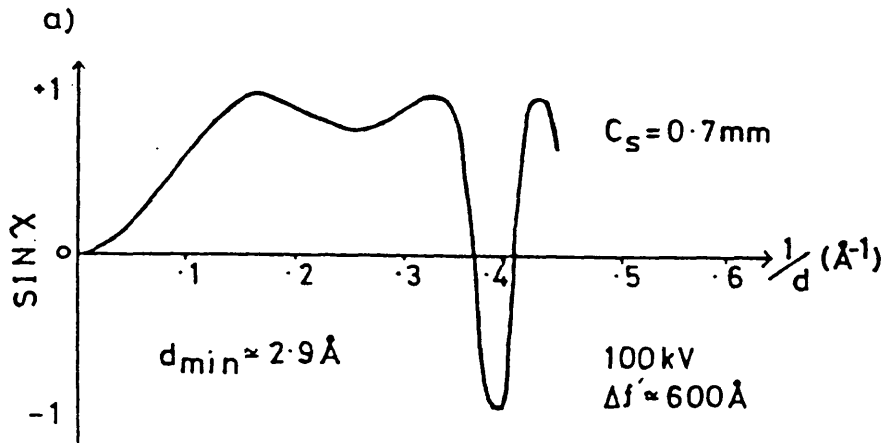


Fig. 1.4 Optimum defocus phase contrast transfer curves for increasing spherical aberration coefficient

a) $C_s = 0.7 \text{ mm}$ (JEOL 100C),
b) $C_s = 2.8 \text{ mm}$, and
c) $C_s = 4.5 \text{ mm}$.



It is possible to resolve structures with a periodicity outwith the range limited by the Scherzer cut-off by choosing a defocus value which will show the required frequency in high contrast (or high reverse contrast). An example of this is shown in Fig. 1.3 where 2.9 Å periodicity could be imaged with high contrast at 200 Å underfocus or with reversed contrast at 0 underfocus. It must be borne in mind when interpreting such an image, however, that the contrast of other periodicities may be altered, leading to false detail in the micrograph.

The source of electrons is not, however, a perfectly coherent point source. For practical purposes it is thought of as disc-shaped and incoherent, and this, combined with electronic instabilities, imposes a "damping envelope" on the objective lens transfer function with the form:

$$A(K) = P(K) \exp \left\{ i \chi(K) \right\} \exp \left\{ \frac{-\pi^2 \Delta^2 \lambda^2 K^4}{2} \right\} \gamma \left(\frac{\nabla \chi}{2\pi} \right) \quad [1.18]$$

$$\text{where } \chi(K) \text{ is equal to } \pi \Delta f \lambda K^2 + \frac{\pi C_s \lambda^3 K^4}{2}$$

K is the scattering angle:

$$K = \frac{\sin \theta}{\lambda} = (u^2 + v^2)^{1/2} ; \text{ and}$$

$$\Delta = C_c \left[\frac{\sigma^2(V_0)}{V_0^2} + \frac{4\sigma^2(I_0)}{I_0^2} + \frac{\sigma^2(E_0)}{E_0^2} \right]^{1/2}$$

$\sigma^2(V_0)$ and $\sigma^2(I_0)$ are variances in fluctuations of accelerating voltage and lens current respectively.

C_c is the chromatic aberration constant.

The effect of this envelope function on the transfer function is shown in Fig. 1.5. Physically the result of partial coherence is an attenuation of contrast in regions where the slope of $\chi(k)$ is large, while contrast is preserved where the slope is small. A full description of coherence effects is given by Spence (1981).

1.5 The Scattering of Electrons.

Several mathematical theories have been developed to account for the transmission of phase and amplitude contrast in the electron microscope, the simplest being the kinematical scattering model (Vainshtein 1964) which is dependent for its effectiveness on assumptions which severely limit its applicability. The kinematic theory explains best the scattering from thin specimens of low atomic weight, where an electron is scattered no more than once during its passage through the specimen, and where the intensities of the scattered beams are very small compared to that of the central beam (Spence 1981). When these rigorous conditions are not satisfied, the more complex dynamical model must be introduced

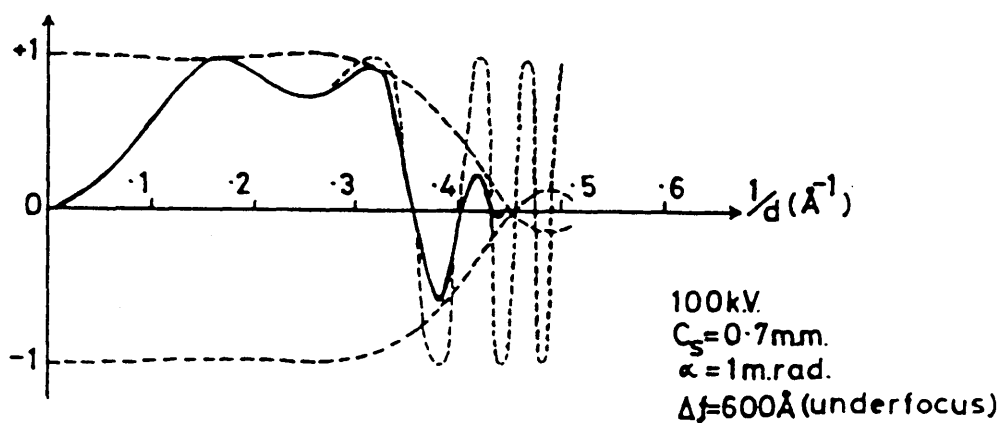


Fig. 1.5

Optimum defocus PCTF. modified by partial coherence for specimen illumination angle $\alpha = 1 \text{ mrad.}$
 The dashed line represents the damping envelope function.
 The full line is the product of $\sin \chi$ and this function.
 The continuation of the undamped function is represented by dots.

back into the main beam. With sufficient thickness of crystal, a dynamical equilibrium is set up between the main and scattered beams, and their observed intensities become independent of crystal thickness. The correspondence between each image point and the object point from which it arises is no longer linear, so for structural imaging the crystals must be kept sufficiently thin for the kinematical approximation to apply (about 150 Å for light atoms, thinner when a heavier atom is present). Dynamical scattering may be approached either by a wave-optical formulation, in which the changes in amplitude of the main and scattered beams are calculated, or by a wave-mechanical calculation in which the steady-state wavefunction describing the behaviour of an electron moving in a potential $V(\underline{r})$ obeys Schrödinger's wave equation

$$\nabla^2 \psi(\underline{r}) + \left(\frac{8\pi^2 m e}{h^2} \right) [E + V(\underline{r})] \psi(\underline{r}) = 0 \quad [1.19]$$

where

$$\nabla^2 = \frac{d^2 \psi}{dx^2} + \frac{d^2 \psi}{dy^2} + \frac{d^2 \psi}{dz^2}$$

ψ is the wavefunction such that

ψ^2 is the probability of the electron being present in a unit volume

$V(\underline{r})$ is the electrostatic potential

The two methods are described in Hirsch et al (1965), and shown to be equivalent.

In the two-beam dynamical theory, the changes in amplitudes of only the main beam and one scattered beam are considered, as they pass through a distance dz in the crystal (see Fig. 1.6.). In this diagram, χ is the wave vector "in vacuo" of an electron with energy eE , and χ' is the wave vector of the scattered wave, and has the same magnitude as χ .

$\chi' = \chi + \underline{g} + \underline{s}$ where s is a small vector accounting for a slight deviation from the Bragg reflecting position.

The values of \emptyset_c and \emptyset_g vary with the depth in the crystal, and waves scattered through a Bragg angle, where $\chi \rightarrow \chi'$ or $\chi' \rightarrow \chi$, will be in phase with each other.

The wave function describing the electrons propagating in a column of crystal is given as:

$$\psi(\underline{r}) = \phi_0(z) \exp(2\pi i \underline{\chi} \cdot \underline{r}) + \phi_g(z) \exp(2\pi i \underline{\chi}' \cdot \underline{r}) \quad [1.20]$$

For more complex calculations the multi-slice technique is used, in which the crystal is divided into n slices and the propagation of the wave computed for each slice. This technique is described by Cowley (1975).

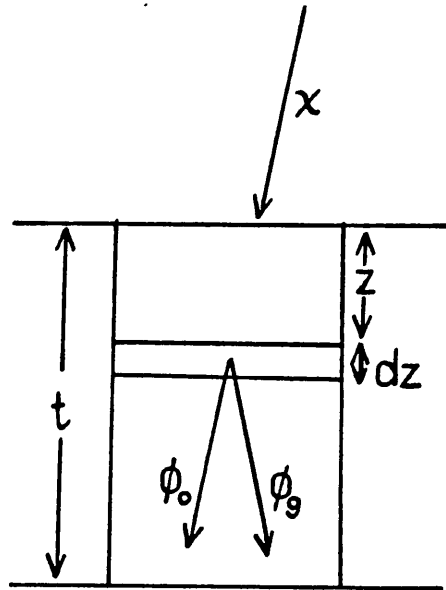


Fig. 1.6: Transmitted and Diffracted Waves ϕ_0 and ϕ_g , propagating through an element dz of a column of crystal (after Hirsch et al 1965).

1.6 The Microscope as an Electron Diffraction Camera.

The electron microscope may be adjusted for use as a diffraction camera simply by setting the excitation of the projector lenses so that the diffraction pattern occurring at the back focal plane is focussed on the viewing screen, as shown in Fig. 1.2.

When the diffraction pattern from a particular crystal is required, it is possible to choose the size of the specimen area from which the diffracted beams are to come by inserting an aperture below the objective lens. If the magnification of the lens (usually about 40-100X) and the diameter of the aperture (perhaps 20-100 Å) are known, then the area defined at the specimen is also known, subject to the objective spherical aberration and focussing errors (Agar 1960). Both the specimen and the selected area aperture must be in focus on the image plane. From Bragg's law, in order to interfere, the waves coming from the specimen must obey the equation

$$n\lambda = 2d \sin \theta \quad [1.21]$$

where d is the lattice spacing

θ is the scattering angle

λ is the wavelength

n is an integer

To define the points at which scattering occurs, the "Ewald Sphere" was constructed (Figs. 1.7 and 1.8). Where this sphere intersects a reciprocal lattice point, the Bragg equation is satisfied and reflection occurs. The wavelength of the electron is very small (0.037 \AA at 100 kV), so the radius of curvature $1/\lambda$ is therefore large in comparison to the reciprocal lattice spacings. For many purposes the Ewald sphere may be thought of as a flat surface; this is not the case for example for X-rays, where the wavelength of the radiation is considerably larger. In a crystal of finite thickness, reciprocal lattice points take the form of "spikes" whose length is inversely proportional to the number of planes in the crystal (Fig. 1.8); the Ewald sphere may intersect many of these spikes, and the diffraction pattern seen on the screen is a projection of the intersections. To calculate spacings on a diffraction pattern, the simple relationship $R = L \tan 2\theta$ is applied, as illustrated in Fig. 1.9.

Since θ is very small, $\tan 2\theta \doteq 2 \sin \theta \doteq 2\theta$ and combining this with the Bragg equation

$$R d = \lambda L \quad [1.22]$$

L is the effective camera length which is determined by the operating conditions of the objective and projector lenses, but in practice the value of L is set as a constant for given conditions - its value is calibrated using a specimen crystal

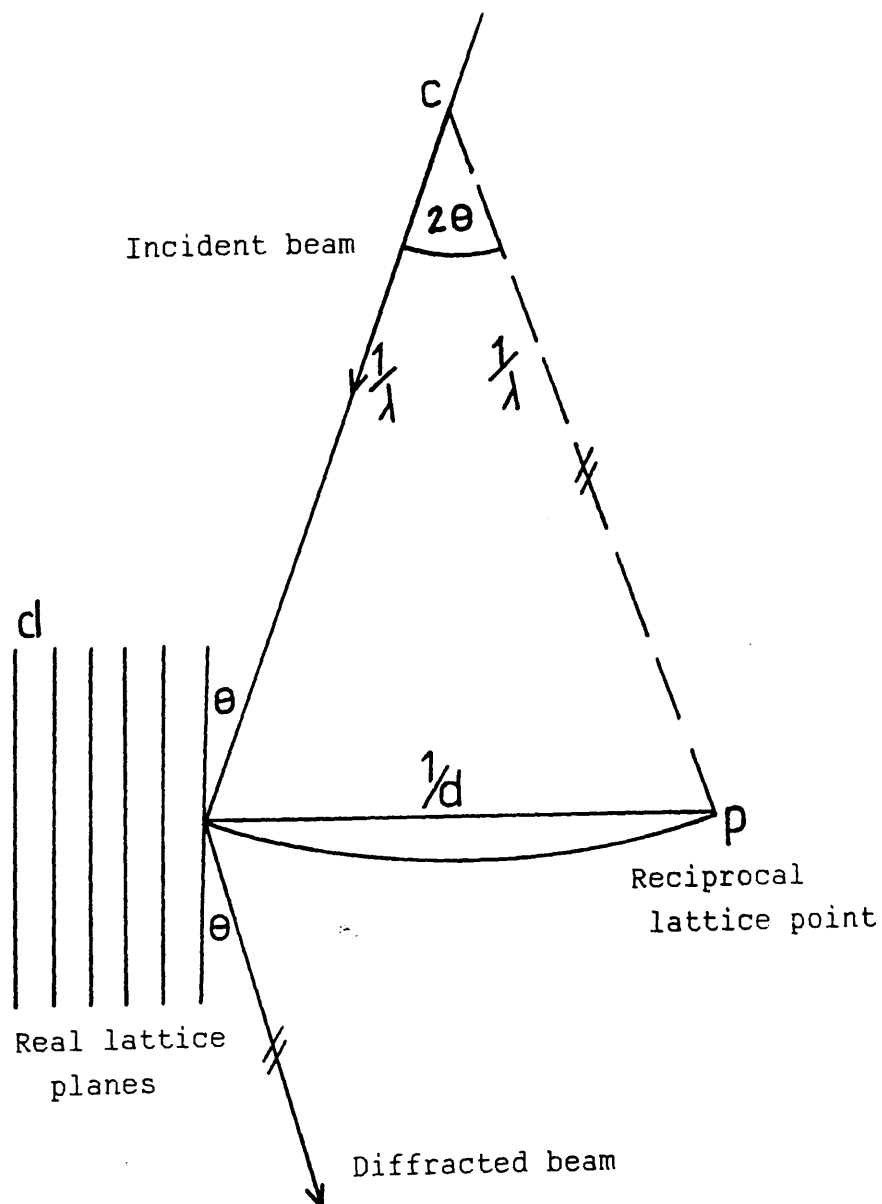


Fig. 1.7: Construction of the Ewald Sphere.

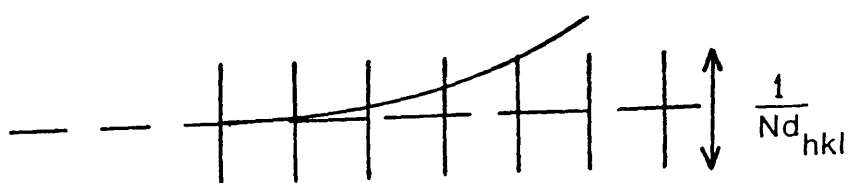


Fig. 1.8: Intersection of the Ewald Sphere with reciprocal lattice spikes

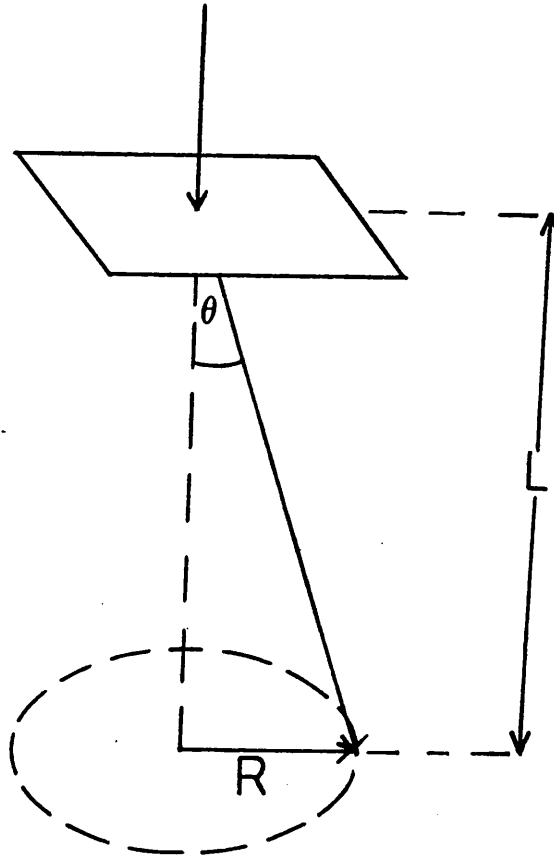


Fig. 1.9 The effective camera length for a diffraction pattern

of known lattice spacing d ; R can be measured directly from a micrograph. Spherical aberration may cause the objective focal length to shorten for large values of θ ; this causes the value of Rd to become slightly smaller for large values of R , but if a standard is used which produces similar sized diffraction rings to the unknown, then a sufficiently high degree of accuracy should be attainable in lattice measurements.

Unknown compounds may be identified from the characteristic spacings and intensities of their powder diffraction patterns, many of which have been tabulated by the Joint Committee on Powder Diffraction Standards (Pennsylvania 1971). The diffraction pattern gives information about the crystallinity and orientation of the specimen - this will be demonstrated in the chapter on paraffins. For details of electron diffraction see Kay (1965).

1.7 Electron Crystallography.

Electron diffraction may be applied to the determination of crystal structure in a manner analogous to X-ray crystallography, and the technique is particularly useful for crystals which are too small to be suitable for single crystal X-ray analysis. The narrow scattering angles of the diffracted electrons and the short wavelength of the irradiating beam compared to the values for X-rays lead to a Ewald sphere with a

large radius of curvature which may be thought of as nearly planar.

Unit cell dimensions are determined by measuring the spacings on the diffraction pattern; geometrical formulae relate observed spacings to the sets of planes for the various possible space groups. Two dimensions of the unit cell are usually directly observable, the third may be obtained with the aid of a goniometer stage or by forcing the specimen to crystallise in an orthogonal orientation, as described in Section 4.4.

Under kinematical conditions, the intensity of a diffraction spot is proportional to F^2 where F is the "structure factor" of a substance and is defined as

$$F_{hkl} = \sum_{r=1}^N f_r \exp 2\pi i (hx_r + ky_r + lz_r) \quad [1.23]$$

f_r is the scattered amplitude from atom r and the exponential term represents the phase of the scattered wave.

h, k, l , are the Miller indices of the scattering planes, and x, y and z are the co-ordinates of the atoms in the unit cell.

Equation 1.23 may be rewritten as:

$$F_{hkl} = \sum_{r=1}^N f_r \left[\cos 2\pi(hx + ky + lz) + i \sin 2\pi(hx + ky + lz) \right] \quad [1.24]$$

which may be simplified to

$$F_{hkl} = \sum_{r=1}^N f_r \cos 2\pi(hx + ky + lz) \quad [1.25]$$

where a centre of symmetry exists in the unit cell, causing the second term to be cancelled by the corresponding term for the atom at $(-x, -y, -z)$.

The expression for the electrostatic potential at point XYZ in a unit cell is:

$$\rho_{(xyz)} = \frac{1}{V} \sum_{h=-\infty}^{\infty} \sum_{k=-\infty}^{\infty} \sum_{l=-\infty}^{\infty} F_{hkl} \exp - 2\pi i(hX + kY + lZ) \quad [1.26]$$

and it is the Fourier transform of the structure-factor expression (equation 1.23). Hence it should be possible to calculate the electrostatic potential, and from it the structure, of the unit cell from the amplitudes and phases of the scattered waves. The amplitudes may be calculated from

the intensities of the reflection, but phases cannot be calculated directly, and so a Patterson function is computed:

$$P_{uvw} = \frac{1}{V} \sum_{h=-\infty}^{\infty} \sum_{k=-\infty}^{\infty} \sum_{l=-\infty}^{\infty} |F_{hkl}|^2 \cos 2\pi(hU + kV + lW) \quad [1.27]$$

This produces a map of interatomic vectors from which possible structures may be deduced.

Refinement of the calculated structure may be carried out by the least-squares method (as described for example in Ladd and Palmer, 1985) until a physically and chemically feasible structure is obtained, in which the observed and calculated structure factors are in good agreement.

Descriptions of Patterson and other methods of crystal structure analysis may be found in Vainshtein (1964). A recent review by Dorset (1985) described the application of such methods to thin crystals of paraffins and other small organic molecules, taking into account the effects of crystal thickness (n-beam dynamical scattering) and bend contours on crystal analysis by electron diffraction.

CHAPTER 2: RADIATION DAMAGE.

- 2.1 Transfer of Energy to the Specimen.
- 2.2 Secondary Processes in the Specimen.
- 2.3 Detection and Measurement of Radiation
 Damage.
- 2.4 Reduction of Radiation Damage in the
 Electron Microscope.

CHAPTER 2 - RADIATION DAMAGE.

2.1 Transfer of Energy to the Specimen.

The resolution attainable on an electron micrograph is not dependent on electron optical and instrumental factors alone; the irreversible changes wrought in the structure of the specimen by the incident ionising radiation play a crucial role in limiting the amount of observed detail. In the case of most organic crystals, the changes may take place well within the time required to choose a suitable area of specimen, adjust the focus and expose a photographic plate for long enough to achieve the desired optical density. This chapter is concerned with the mechanisms, detection and reduction of radiation damage in the electron microscope.

When a beam of electrons hits a thin specimen, most of its energy is transmitted, but some is transferred to the atoms of the specimen by means of various interactions, some of which cause ionisation and bond breakage within molecules.

The amount of energy deposited in a specimen by an electron beam is calculated by the Bethe formula (Bethe 1933), which must be relativistically corrected to take into account energies of up to 1 MeV (Glaeser 1971, Reimer 1975) -

$$-\frac{dE}{dx} = 0.1535 \frac{\rho}{\beta^2} \frac{Z}{A} \log \left[\frac{T^2(T+2)E_0^2}{2I^2} + (1-\beta^2) \right] + \left[\frac{(T^2/8 - (2T+1)) \log 2}{(T+1)^2} \right] \quad [2.1]$$

$$\begin{aligned}
 -\frac{dE}{dx} &= \text{rate of energy loss} \\
 \rho &= \text{density of specimen} \\
 Z &= \text{atomic number} \\
 A &= \text{atomic mass of specimen} \\
 E_0 &= m_0 c^2 \\
 T &= E/E_0 \\
 I &= \text{mean ionisation potential} \\
 \beta &= v/c, \text{ where } v \text{ is the velocity of} \\
 &\quad \text{the incident electrons.}
 \end{aligned}$$

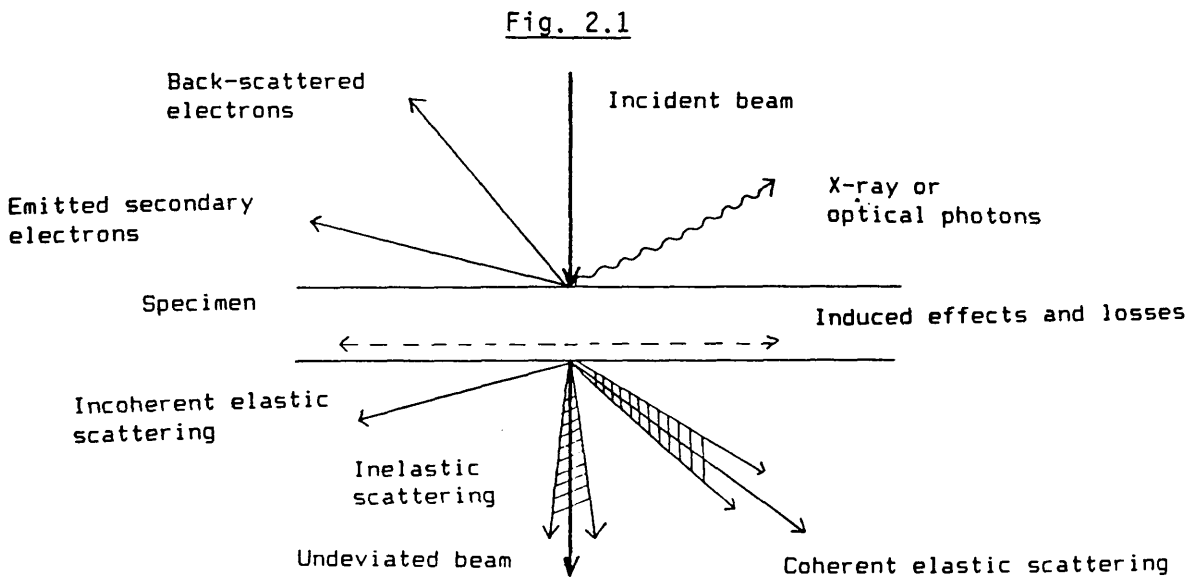
The main features of this equation are that the amount of absorbed energy (the amount of inelastically scattered electrons) varies as the atomic number of the specimen atoms, the path length (thickness and density) and the inverse square of the accelerating voltage of the microscope. The equation may be simplified to:

$$-\frac{dE}{dx} = \beta^2 = \left(\frac{v}{c}\right)^{-2} \quad [2.2]$$

There is much experimental evidence to confirm this dependence of radiation damage on the velocity of the electrons, both at around the 100kV value common to most commercial electron microscopes (Reimer 1965, Grubb and Groves 1971) and at higher accelerating voltages (Martinez et al 1982).

Reimer (1975) points out that as photographic recording is also an ionisation process it too shows a dependence on the square of the voltage and therefore a highly sensitive emulsion must be used in microscopy at high voltages.

The various interactions which the specimen may undergo on irradiation can be summarised in the following diagram (after Grundy & Jones 1976)



The interactions of most interest in conventional transmission electron microscopy are inelastic and elastic scattering. Elastic scattering causes negligible damage and is the main contributor to imaging; inelastic scattering, where energy is transferred to the specimen atoms, causes damage to the specimen and an increase in background noise in the image.

The possibility also exists that an atom may suffer a direct hit by an electron and be displaced from the lattice. The amount of energy transferred in a collision is expressed as

$$E_m = \frac{2E(E + 2m_0 c^2)}{M c^2} \sin^2 \frac{\theta}{2} \quad [2.3]$$

where M and m_0 are the masses of the atomic nucleus and electron respectively, c is the velocity of light and θ is the scattering angle. Although $m_0 \ll M$, the atom may still acquire enough energy to escape from its lattice site. Cosslett (1970) gives the threshold energy for the displacement of a carbon atom by an electron as 27 keV, assuming a binding energy of 5 keV. Such "knock-on" events are comparatively rare; the ratio of the cross-sections for electronic and nuclear interactions is:

$$\frac{\sigma_e}{\sigma_n} \doteq \frac{M}{mZ} \frac{T_{\min}^n}{T_{\min}^e} \doteq 40 \quad [2.4]$$

(non-relativistic approximation) (Hobbs 1984).

Where T_{\min}^n and T_{\min}^e are the minimum transferable energies involved in each type of collision, since energy transfer is not continuous but occurs in quanta.

Thus it is normally the ratio of elastic to inelastic interactions which is of interest in radiation damage studies. However Symons (1982) considers that even atomic collisions with insufficient energy to cause "knock-on" damage may still give rise to a local shock-wave with enough energy to cause mass loss from the surface of the specimen.

The ratio of inelastic to elastic collisions was calculated by Lenz who gives a ratio of

$$n = \frac{\sigma_{\text{inelastic}}}{\sigma_{\text{elastic}}} = \frac{20}{Z} \quad [2.5]$$

for an element; an experimental value of 6 has been quoted for the constant (Zeitler 1982). Z is the atomic number of the element. As Z increases, the proportion of elastic scattering increases due to the deflection of incoming electrons by the large atomic nucleus, while for light atoms this effect is reduced by shielding by the valence electrons (Egerton 1976).

For a compound, Egerton gives as the scattering ratio n :

$$n \doteq \frac{26 \sum_j Z_j^{1/3} N_j}{\sum_j Z_j^{4/3} N_j} \quad [2.6]$$

where N_j is the number of atoms of type j per molecule.

Purely organic materials have a high value for n , organometallic compounds a lower one due to the presence of a heavy atom; for example, n for citric acid has a value of 3.55 while for lead citrate it is 0.93.

On irradiation, an overall reduction in n has been observed for organic compounds which is consistent with mass spectroscopic evidence for loss of hydrogen from the molecules leaving a carbon residue.

Radiolysis occurs where the ionising radiation results in an electronic excitation which is localised over very few bonds and has a lifetime longer than an atom vibration period ($\sim 10^{-13}$ s). The potential energy of the excitation must be greater than the displacement energy of the atom in its excited state, and a nucleus must be able to acquire sufficient momentum from the excitation energy to be displaced (Hobbs 1984). Organic compounds are susceptible to radiolysis because unlike metals they cannot delocalise the electronic excitations along a conduction band, so a bond is likely to break before the energy can be dissipated. For this reason purely aliphatic molecules are less stable than those with conjugated double bonds.

Where a free radical mechanism is involved in a radiation-induced reaction, the conditions prevailing in the microscope

may be approximated by an Electron Spin Resonance spectrometer, although a few important differences between the two techniques must be borne in mind. The bulk E.S.R. specimen may have different properties from the thin film used in electron microscopy, and the applied radiation dose in the electron microscope might be $\sim 10^{25}$ eV/g for carbonaceous material as opposed to only 6×10^{20} eV/g in the E.S.R. spectrometer (Box 1975).

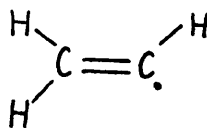
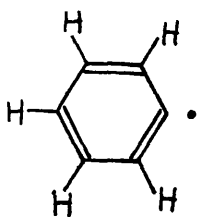
A free radical contains an unpaired electron and its reaction with another radical ($R^\cdot + R^\cdot \longrightarrow R_2$) is dependent on its diffusion rate through the matrix. The radical may react with a neutral molecule to produce another radical:



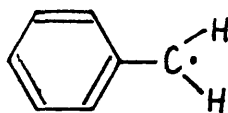
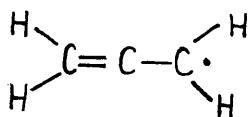
Another frequent reaction is the abstraction of hydrogen from the molecule $R'H$:



This only occurs when the $R-H$ bond is stronger than $R'-H$; phenyl and vinyl radicals are particularly efficient at hydrogen abstraction:

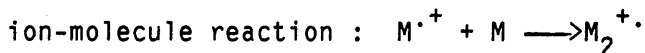


whereas radicals in which the unpaired electron is conjugated to a double bond are less reactive



(Henglein 1984)

Molecules and ions with a radical centre may undergo a variety of reactions. A few examples are:



A more complete list of possible reactions is given in O'Donnell & Sangster 1970, Henglein 1984, etc.

The reaction is terminated by the formation of a neutral species or stable ion. A diffusing electron may also be trapped either physically by a lattice defect or chemically by an electron scavenger such as a sulphur or a halogen atom, which reacts with it to form a stable ion.

Many authors use as their measure of damage the radiolysis yield or "G" value where G stands for the number of fragmented molecules per 100 eV of absorbed energy (Reimer 1965, Bernsen & Reimer 1981, Reimer & Spruth 1982, Fryer 1984).

This gives a total number of damaged molecules after irradiation, irrespective of the mechanism by which it occurred. Reimer (1965) gives an extensive list of G values for various organic molecules. Radiolysis occurs with some specificity; different sites of attack and leaving groups have different G values, and this depends on the length of the hydrocarbon chain and the nature of the side group. G_{H_2} is at its highest (3.8 - 5.6) for saturated hydrocarbons; unsaturated hydrocarbons undergo polymerisation and cross-linking, liberating less hydrogen ($G_{H_2} = 0.8-1.2$) but having an extremely high G_M (the total number of changes occurring in the molecules) of $11-10^4$. Molecules containing a carboxyl group tend to have lower G values as this group is a good scavenger of hydrogen atoms; carboxylic acids and alcohols liberate water molecules, although $G_{H_2} > G_{H_2O}$.

The least easily ruptured bonds are those of the aromatic hydrocarbons, which may be a consequence of the ability of these molecules to spread the energy acquired during excitation over all the conjugated carbon-carbon bonds preventing one particular C-C or C-H bond from breaking. The energy may be dissipated by the molecule returning to its ground state as

fluorescence, which is a characteristic property of many polycyclic hydrocarbons (Friedlander et al 1964). Bond scission generally occurs at any alkyl side-chains the ring may possess.

Aromatic molecules may also have scavenging properties towards dissociated hydrogen atoms, and may even protect a more radiation-sensitive molecule if a mixture is irradiated. For example the value of G_{H_2} for cyclohexane drops dramatically on the addition of benzene molecules to form a mixture (O'Donnell & Sangster 1970) while an aryl cyclo-alkane appears to be protected by its own substituent - the value of G_{H_2} is linear with composition in a benzene mixture.

2.2 Secondary Processes in the Specimen.

Once the energy of the irradiation has been deposited in the specimen it may be dissipated in a number of ways, not all of them destructive. There may be emission of electromagnetic radiation in the X-ray, ultraviolet or visible regions of the spectrum which leaves the specimen atoms undamaged and in the ground state.

However, in many substances including the organics, the excitation of the specimen electrons leads to the formation of ions and radicals, causing alterations to the chemical properties of the molecules and to the structure of their crystal lattice. These alterations may lead to bond-scission and mass loss, cross-linking of polymers and the diffusion and capture of radicals.

Small gaseous molecules may be released from an organic crystal as a result of bond scission, e.g. H_2 , H_2O , CO , CO_2 and CH_4 . This causes an overall loss of mass in the specimen which may be detected simply by weighing, or by measuring the difference in image contrast, or by measuring changes in the refractive index of the substance caused by changes in its internal structure.

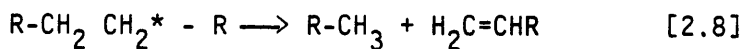
Although the specimen size required is too large for this to be a practicable method of routine mass-loss analysis of a specimen on a standard microscope grid, irradiation experiments on a larger scale have been carried out on various polymers where the change in weight was used as a measure (Bahr et al 1965, Brockes 1957).

Measurements of contrast may be offset by the formation of a contamination layer at high doses, which renders results unreliable.

Cross-linking of Polymers.

It has been suggested that radical sites may migrate along or across the chains until two become adjacent and react to form a bond (Dole et al 1954, O'Donnell & Sangster 1970).

Scission Reaction:



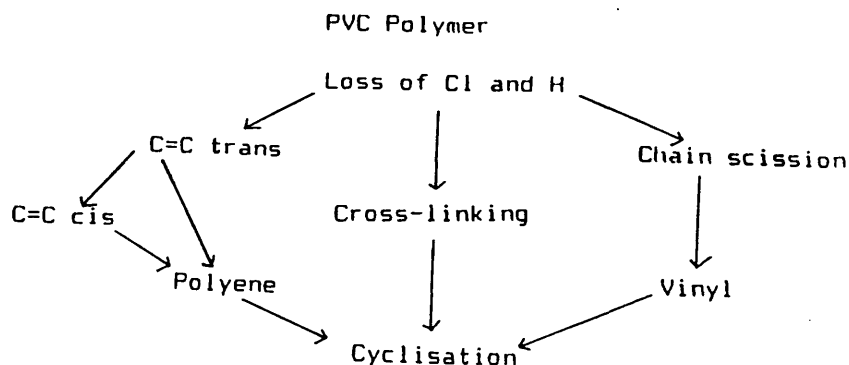
* denotes an excited or ionised molecule.

Cross-linking and scission may occur simultaneously, and the ratio depends on the temperature, crystallinity, steric factors and the presence or absence of air.

It has been observed that in general, for a vinyl-type polymer, degradation usually occurs where there is a tetra-substituted carbon atom in the main chain (O'Donnell & Sangster 1970). The presence of oxygen may cause the formation of peroxy species, which prevent the recombination of the broken bond and so leads to degradation.

Examples of the behaviour of different polymers subjected to irradiation may be found in "The Radiation Chemistry of Macromolecules" (ed. Malcolm Dole, Academic Press 1972).

The possible reactions of irradiated poly(vinyl chloride) may be represented diagrammatically by:



After D. Vesely (1984).

The end products appear to consist of relatively stable compounds with conjugated double bonds - for example, the polyene and cyclic structures.

Re-formation of broken bonds is possible, leaving the original or near original structure, due to the "cage effect" which holds the severed species in its place in the crystal lattice and prevents it from diffusing away (Grubb 1974, Clark et al 1980). This effect is particularly relevant in the study of alkyl halides, as the large size of a halide ion prevents it from diffusing as quickly through the lattice as the H_2 molecules formed on removal of hydrogen ions or radicals, which are liberated in large amounts from organic molecules. The substitution of chlorine or bromine at the peripheral hydrogen

positions of phthalocyanine gives an increased lifetime with the ratio $RH : RCl : RBr = 1 : 3 : 4$ (Fryer & Holland 1983).

The phthalocyanines are particularly stable to irradiation, probably because of their ability to delocalise the energy of the primary collision over the extended aromatic system. They are especially suitable for damage studies because of their crystal growth characteristics, and because their stability allows molecular images to be recorded and damaged areas to be identified from the images (Uyeda et al 1973, Murata et al 1976, Fryer & Holland 1983).

One such study (Fryer 1984) shows, on sequential molecular images of hexadecabromo copper phthalocyanine, the spreading of the damaged area outwards from an initially damaged area. It is apparent that a crystallite is first affected where an edge is exposed, for example, at a grain boundary, rather than at a perfectly crystalline area, and that the rate of damage depends on the thickness of the specimen and the nature of the peripheral atoms of the molecule.

2.3 Detection and Measurement of Radiation Damage.

To study radiation damage in the electron microscope quantitatively, an accurate measurement of the current density incident on the specimen is essential, and this is usually achieved by means of a Faraday cage installed on the image plane of the microscope. Nicholson (1981) gives details of a Faraday cage rod which measures the incident electrons at the plane of the specimen, but this may not be used during an experiment. A collector plate at the image plane is less accurate but may be used continuously.

The current density j on the specimen is related to the current I detected by the Faraday cage by the equation

$$j = \frac{\epsilon_F I M^2}{A_F} \quad [2.9]$$

where ϵ_F is the collector efficiency of the plate taking into account the back scattering of electrons from the plate.

M is the total image magnification.

A_F is the area of the Faraday cage.

The most commonly used units are coulombs per square centimetre, or electrons per square Ångstrom per second:

$$1 \text{ C/cm}^2 = 624.2 \text{ e}^-/\text{\AA}^2$$

Measurement of j allows the determination of the total exposure to electrons

$$q = jt \quad [2.10]$$

where

t = time (seconds)

It can be seen that for a constant current density on the image plane (and hence on the photographic plate or other recording medium) the beam current density on the specimen increases as the square of the magnification. Therefore the magnification should not be set any higher than necessary for the imaging of beam-sensitive specimens.

Microscopy of such specimens involves striking a balance between magnification, film speed and grain size, applied dose, resolution and contrast.

The relationship between the number of electrons interacting with the specimen and the object contrast observed on the plate is:

$$Cd > \frac{5}{\sqrt{f N_{cr}}} \quad [2.11]$$

(Rose 1948, Glaeser 1975)

where C = object contrast (a typical value may be 0.1)

d = minimum object size to be seen (i.e. required resolution)

N_{cr} = critical exposure ($e^-/\text{\AA}^2$)

f = utilisation factor, which accounts for the fact that not all the electrons interacting with the specimen are involved in forming the image.

The constant 5 is the signal to noise ratio empirically taken to be 5 by Rose (1948).

Even if f were unity, according to this equation, to attain a resolution of 10\AA with $C = 0.1$ and the signal to noise ratio 5, an applied total dose of $N_{cr} > 25e^-/\text{\AA}^2$ would be required, which is more than enough to destroy most organic specimens at room temperature. Fortunately low dose recording followed by computer averaging techniques allows this limitation to be overcome to some extent. These techniques will be further described in Chapter 3.

Boudet and Kubin (1982) have calculated signal to noise ratios in terms of the number of electrons forming each part of the image and the fractions of the incident beam involved for bright and dark field images; they conclude that for substances with a critical dose of less than 0.25 C/cm^2 ($1.56 \times 10^2 e^-/\text{\AA}^2$; this includes aliphatic and polymeric hydrocarbons) the

limiting factor for resolution is not statistical noise but the sensitivity of the photographic emulsion.

There are two categories of detection method for radiation damage in the electron microscope; firstly those which measure damage "in situ", as a function of exposure, electron energy and temperature. These include mass loss, the fading of electron diffraction patterns and lattice contrast, and changes in certain spectroscopic properties (electron energy loss spectroscopy, X-ray microanalysis). Then there are methods in which a pre-irradiated sample is analysed outside the microscope. For example, the rupture and cross-linking of infra-red active bonds in organic compounds may be followed by infra-red spectroscopy (a fairly thick specimen is required for this), or the visible absorption spectrum may give information where an evaporated dye has been irradiated (Reimer 1961, 1975).

Electron energy-loss spectroscopy ("E.E.L.S.") is widely used to measure the characteristic absorptions by the specimens of energy lost by the electron beam during inelastic scattering events. These can be separated and identified as $\pi - \pi^*$ transitions, π - electron ionisation and outer shell ionisation; for example (Isaacson 1975) the K shell ionisation energies of carbon, nitrogen and oxygen (285, 395 and 535 eV

respectively) show up clearly on the spectrum for thymine and the characteristic low-lying electron energy loss spectrum (0-10eV) for acridine orange shows a marked difference in intensity before and after radiation damage has occurred.

This low-lying region is due to the $\pi - \pi^*$ transition of the aromatic ring, which appears to be destroyed by K - shell ionisation.

E.E.L.S. detects changes in molecular structure, and so complements electron diffraction studies which reveal changes in crystal lattice structure. A detailed account of E.E.L.S. is given by Egerton(1984).

The measurement of the intensity of the diffraction pattern as it fades is one of the most frequently employed methods of monitoring the extent of radiation damage in crystalline specimens. The specimen may be a single crystal giving rise to a regular array of spots, or it may be polycrystalline and produce Debye-Scherrer rings. Sometimes the total dose necessary to destroy the pattern completely is quoted; for quantitative work a microdensitometer is used to measure the reflection intensities from the micrograph and the dose required to cause the spots to fade to $1/e$ of the value of their original intensity is given, where e is the natural

logarithm base. For obvious reasons diffraction patterns in a fading series must be recorded at an exposure below the saturation of the recording medium.

The bending of a crystal under the electron beam causes deviations in diffracted beam intensities which may give misleading results in a fading series of the diffraction pattern and which must be taken into account in a crystal structure analysis (Dorset 1980).

Different reflections fade at different rates; often the higher order spots fade first leaving the lower resolution reflections. Diffraction patterns of beam-damaged paraffin crystals show the fading of the lamellar 001 spots while the reflections due to the carbon-chain zig-zag remain intense (Dorset et al 1984). The time taken for the spots to fade gives an indication of the maximum amount of resolvable detail one is likely to obtain in an image.

The fading of electron diffraction patterns as a function of specimen thickness was measured on behenic acid films by Ohno (1984) who found that in the range 25-100Å the critical dose varied linearly with specimen thickness.

Provided the kinematical approximation holds, the integral intensity I_g of a reflection is proportional to the number N of reflecting unit cells:

$$I_g = C.N \quad (\text{Siegel 1972}) \quad [2.12]$$

The intensity of a reflection is therefore directly proportional to the number of unit cells remaining intact during irradiation.

Siegel uses classical collision theory to account for the destruction of unit cells and derives an exponential relationship between the applied dose D_n and the ratio of surviving cells to the original number of cells:

$$\frac{N}{N_0} = e^{-\sigma_s D_n} \quad [2.13]$$

where σ_s is the damage cross-section. This cross-section is shown to be equal to the sum of the ionisation cross-sections of all the atoms in the cell; Siegel concludes that even once the molecules have come together to form a molecule they remain individual beam-sensitive entities, and that every ionisation leads to dissociation. He attributes the higher stability of the benzene ring to its shape; it requires more than one hit to destroy the molecule.

By studying the diffraction pattern as it fades, it is also possible to detect changes in lattice dimensions, and broadening of reflections. Orth and Fischer (1965) irradiated two polymers and a paraffin ($C_{28}H_{58}$) and measured the width at half the maximum height of the densitometer traces of the diffraction spots. With paraffin, the diffraction spots faded without broadening or shifting position; it appears that the lattice structure remains unchanged although changes similar to thermal effects occur in the immediate vicinity of the damaged bonds. The polyoxymethylene pattern behaves similarly; it is believed that here the radiation causes breaks in the main chain liberating large radicals and formaldehyde which diffuse through the lattice leaving voids and destroying the structure.

The polyethylene pattern on the other hand not only decreases in intensity but undergoes broadening and shifting of reflections. This indicates changes in the lattice vectors caused by cross-linking leading to a loss of long range order in the crystal.

2.4 The Reduction of Radiation Damage in the Electron Microscope.

The consequences of radiation damage in the electron microscope cannot be completely eliminated, but much research has been conducted into ways of reducing them as much as possible, particularly by attempting to reduce mass loss and to slow down the secondary reactions which lead to loss of crystallinity and the destruction of molecular structure.

The primary cause of radiation damage, the initial transfer of energy to the specimen, can be inhibited to some extent by the use of a high accelerating voltage, which reduces the frequency of inelastic scattering events; however, the theoretical curve of specimen lifetime against accelerating energy, calculated from equation 2.1, reaches a maximum just above 1 MeV and begins slowly to decrease thereafter (Glaeser 1971).

The lifetime of certain organic substances has been shown to be increased by a factor of 3 on increasing the voltage from 100 kV to 1 MeV (Kobayashi and Sakaoku 1965, Cosslett 1978). The Bethe equation (equations 2.1 and 2.2) predicts a variation in critical exposure with β^2 , although some investigators e.g. Howitt et al (1976) obtain a closer approximation to β^3 , using the amino acid l-valine as their sample. Smith et al (1982) report that working at 500 kV allows the observation of Sb_2S_3 at higher magnification and longer observation times than at 100 kV.

Martinez et al (1982) report experiments on l-valine, leucine and pentacene with up to 2.5 MeV electrons, in which the specimen lifetime is extended by high voltages (by a factor of 9 between 100 kV and 2.5 MeV in the case of l-valine).

The influence of specimen contamination on radiation damage is not certain; Glaeser (1975) considers that under normal operating conditions residual gases would not affect the specimen significantly. However, Hartman et al (1974) report that lattice fringes of indanthrene olive T were still visible after 20 minutes irradiation at high vacuum (three days pumping) whereas they were destroyed by the same current density in 5 minutes in the presence of residual gases (2 hours pumping). Gas pressures and crystal thicknesses are not quoted.

Halide Substitution.

The improvement of specimen lifetime by the substitution of a halide at the peripheral hydrogen positions of an organic molecule has already been mentioned (Section 2.2). Molecular images of chlorine and bromine-substituted copper phthalocyanines have been published by Fryer (1984) and Uyeda et al (1972). Clark et al (1980) studied chlorine substituted copper phthalocyanines by X-ray microanalysis and concluded that chlorine atoms and fragments containing chlorine are lost from the edges of the molecules; the diffusion of the fragments is hindered by the cage effect except where the latter is

interrupted by previous damage or by a crystallite boundary.

Kobayashi and Reimer (1975) compared the end-point doses of hexabromobenzene C_6Br_6 and tetrabromoquinone $C_6Br_4O_2$ and noted a decrease in radiation resistance of an order of magnitude on substituting oxygen atoms for two of the bromine atoms. Uyeda et al (1974) have published images in which the 4.1 Å lattice planes of tetrabromoquinone have been resolved; hence it should be possible to resolve lattice planes of hexabromobenzene in a goniometer stage.

Protective Coatings and Encapsulation.

Initial interest in the effect of coating a microscope specimen in order to protect it from damage arose from the belief that the specimen underwent a large rise in temperature upon irradiation (Reimer 1959). In spite of the high energies involved, however, it has been demonstrated that it is possible to image successfully crystals with a melting point of 40⁰-50⁰C (Keller 1961). It would appear that although the temperature of the specimen and its environment does influence the rate of structural damage, direct local heating by the beam is not a primary cause of such damage provided the specimen is in contact with a carrier foil of good thermal and electrical conductivity which allows rapid dissipation of energy (Grubb 1974).

Knapek and Dubochet (1980) found that crystals of organic and biological materials mounted on carbon support films were more resistant to radiation damage than those mounted on collodion, which has a lower thermal conductivity. Heide (1982) suggests that beryllium or beryllium oxide films should reduce local electron beam heating, and he has also calculated the rise in local temperature as it varies with beam diameter and current density at 4.2 K; provided these parameters are kept low a specimen temperature rise of only a few degrees is expected.

Experiments in which the specimen is backed with a conducting coating on both surfaces have been carried out by Salih and Cosslett (1974) who measured a three-fold improvement in specimen lifetime when coronene crystals were sandwiched between aluminium layers, and a five-fold improvement when gold was used as the coating material.

A number of different evaporated organic films were encapsulated with carbon (Fryer and Holland 1983) and the "protection factor" varied between 3 and 12 depending on the structure of the specimen. The most marked improvement on encapsulation occurred for the halogenated molecules, supporting the theory that the larger peripheral fragments are held in place by the cage effect while the smaller fragments

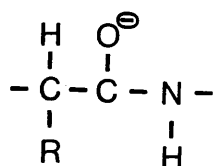
can diffuse away. A similar effect was observed with an SiO coating by Holland et al (1983) who also suggest that as the protection of the specimen was independent of the nature of the covering film, it was not a consequence of charge dissipation (see also Fryer and Holland, 1984).

The prolonging effect on the specimen lifetime when an inorganic halide was included in the sandwich between the specimen and the carbon film was investigated by Fryer et al (1984) who concluded that chloride or bromide ions combined with the activated molecules of the crystal, thus preserving them from further damage.

Low Temperature Microscopy.

It is apparent from Electron Spin Resonance studies of organic substances that many of the effects of ionising radiation are curtailed at low temperature. At room temperature the oxidation and reduction processes (loss and gain of electrons) taking place in the specimen lead to bond rupture, migration of fragments, cross-linking etc. At 4.2 K, while the same primary oxidation and reduction processes still occur, the products do not degrade until the specimen is warmed up; for example, a

peptide linkage suffers ionisation but does not break at low temperature:



(Box 1975)

Intramolecular proton and electron transfer are reduced at low temperature, as is the migration of open valences, which hinders cross-linking between molecules. Changes in conformation of damaged molecules are prevented (Box and Freund, 1966). Atomic migration and the diffusion of severed fragments are halted; The particles are "frozen in" to their place in the lattice and the chances of bond reformation are increased.

Orth and Fischer (1965) carried out an investigation on organic polymers and a paraffin in which the temperature of the specimen was raised; in each case the damage rate was accelerated.

One of the first experiments in which organic crystals were examined in the temperature range 4-300 K was carried out by Siegel (1972), who used a paraffin ($\text{C}_{32}\text{H}_{66}$) and tetracene as examples of aliphatic and aromatic compounds respectively. The destruction of the crystal lattice was measured by the fading

of the diffraction patterns, and with the specimen cooled to liquid helium temperature, Siegel observed a "latent dose" during which the intensities remained constant, and after which they started to diminish. The lifetime of the crystals was extended by up to five times on cooling from 300K to 4 K, and this was ascribed to the slowing down of secondary damage, although primary reactions continue regardless of temperature.

An initial increase in intensity of the reflections, including the undeviated beam, from the paraffin specimen was attributed to mass loss.

Another method of monitoring radiation damage applied by Siegel is the observation of the destruction of the extinction bands on a paraffin crystal. It was observed that, on irradiation at 4 K the crystal remained stable until the latent dose had been delivered, but on warming up to 300 K the effect on the extinction bands was the same as if irradiation had taken place at room temperature. These results were interpreted as indicating the "freezing in" of damaged particles at low temperature and their subsequent release on warming; after the latent dose has been absorbed however, there are sufficient detached particles present in the lattice to cause its disintegration.

Results of low temperature studies vary widely; some authors found very little change in radiation sensitivity at low temperatures (Glaeser 1971, Venables & Bassett 1967). Others have claimed spectacular results, for example Knapik and Dubochet (1980) and Dubochet et al (1981), who recorded a thirty-fold improvement in radiation resistance at 4 K for paraffin and phenylalanine, a factor of 70 for l-valine and one of 400 for ATP. However a group including Knapik and Dubochet stated in a later publication (Lepault et al 1983) that their previous results were not reproducible, and that the improvement at low temperature was not so great as had been claimed.

Most results show a protection factor at low temperatures of about 3 - 5 times. Some examples are:

<u>Author</u>	<u>Specimen</u>	<u>T(K)</u>	<u>Gain</u>
Grubb & Groves(1971)	Polyethylene	18	3
Siegel(1972)	Paraffin	4	5
	Tetracene	4	5
Salih & Cosslett(1975)	Anthracene	20	3.5
	Coronene	20	3-4
Glaeser & Taylor (1978)	Catalase	150	3
Hayward & Glaeser (1979)	Purple membrane	153	3.5-11
Chiu et al(1981)	Crotoxin	4	10

There is some disagreement among authors as to whether it is necessary to use liquid helium temperatures (~ 4 K) or whether most of the protection offered by cooling the specimen is already achieved by liquid nitrogen (77 K). Siegel (1972) observed a significant increase in latent dose below 77 K as well as an over-all increase in protection at very low temperature.

Salih and Cosslett (1975) found that the improvement in specimen lifetime for coronene was greater below liquid nitrogen temperature than between 293 K and 77 K, and suggest that two different mechanisms are involved at different temperatures: at low temperatures, while the particles are frozen into place, deterioration of the diffraction pattern is due to damage to individual molecules, while at higher temperatures thermal agitation prevents bond healing and accelerates damage.

Downing (1983) plotted the critical exposure N_e against temperature for five fatty acids between 4K and room temperature, and found that cooling with liquid helium doubled the lifetime attainable with liquid nitrogen cooling. Although the increase appears to be a continuous function of temperature, it is possible that there may be a discontinuity at the point, somewhere below 10 K, below which electrons are no longer mobile in the lattice.

In contrast to the above results, Wade (1984) found that a plot of the gain in specimen lifetime against temperature for paraffins reached a maximum of 3-4 at about 70K then levelled off, giving no additional gain on cooling to liquid helium temperature.

The International Experimental Study Group, in a collaborative review (1986), also casts doubt on the likelihood of a significant improvement in protection at very low temperatures, although uncertainty in the measurement of temperatures below 20 K makes this a more complex experimental problem than had at first been imagined.

CHAPTER 3:
EXPERIMENTAL TECHNIQUES.

- 3.1 Microscopes used in Room-Temperature and
 Low-Temperature Studies.
- 3.2 The Minimum Dose System (MDS).
- 3.3 Densitometry and Digitisation of Images.
- 3.4 Image Processing.
- 3.5 The Optical Bench.

CHAPTER 3: EXPERIMENTAL TECHNIQUES.

3.1 Microscopes used for Room-Temperature and Low-Temperature Studies.

At Glasgow, microscopy was carried out with a JEOL 100C electron microscope fitted with a high-resolution pole-piece ($C_s=0.7\text{mm}$). This microscope has a top-entry specimen stage and for radiation dose measurements a copper collector plate was placed on the image plane.

A JEOL 1200 EX was also used for room-temperature studies. This operates at 120kV and has a side entry stage. An image intensifier was used as an aid to focussing and astigmatism correction.

Microscopy at temperatures below room temperature was carried out on three different instruments:

(a) The JEOL 100B at the Medical Foundation of Buffalo was fitted with a side-entry stage. A specimen holder cooled by liquid nitrogen and incorporating a heating coil to provide a range of specimen temperatures down to about 120K was available, as well as a conventional tilting holder.

(b) The microscope used in Berlin for low-temperature

(<15K) high resolution work was built at the research department of Siemens A.G. in Munich, and has a prototype helium-cooled superconducting lens system incorporating the objective and an intermediate lens.

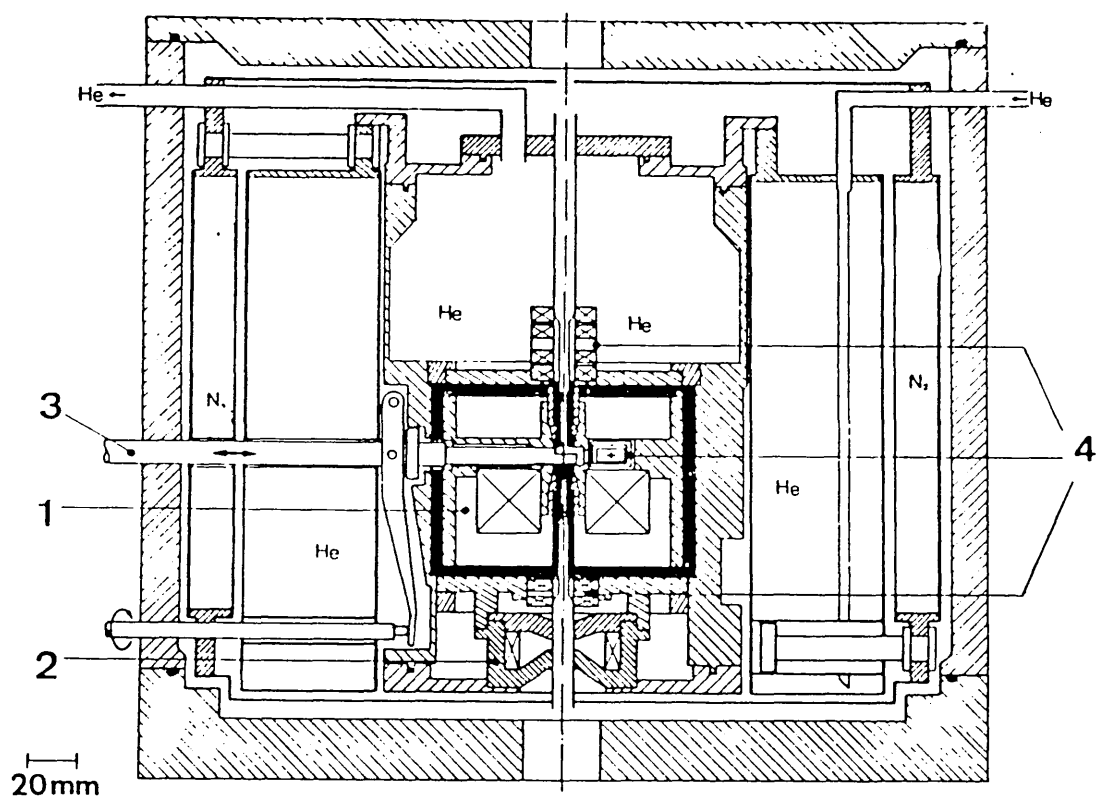
This microscope is described by Lefranc et al (1982), and a diagram of the lens is shown in Fig. 3.1. The instrument operates at an accelerating voltage of 100kV, and has a lattice resolution of about 3\AA . A minimum dose system is incorporated to reduce the exposure of the specimen to the beam (see section 3. 2).

- (c) A microscope was also available in Berlin in which the temperature of the specimen could be varied between room temperature and 8K. This was the "Deeko 250", designed to operate at up to 250kV but which was used at 100kV to allow comparison of results with those from other sources. The resolution of this instrument was poorer than that of the Siemens microscope, being about 20\AA . The design of this microscope is described in detail by Heide (1981).

3.2 The Minimum Dose System (MDS).

Micrographs of beam-sensitive materials were taken using a

Fig. 3.1 The helium-cooled superconducting objective lens with side-entry stage (Lefranc et al).



- 1: Objective lens of the shielding type
- 2: Iron circuit intermediate lens
- 3: Side-entry specimen holder
- 4: Correction systems

minimum dose technique. Accounts of the development of this technique have been published by Williams and Fisher (1970), Unwin and Henderson (1975) and Fujiyoshi (1980). Images of anthanthrene crystals have been published in which the minimum dose method was applied (Fryer 1978).

The specimen is searched with the microscope in the diffraction mode, thereby reducing the dose rate necessary to see by eye a good crystalline area. Once such an area has been found, the beam is switched by a deflector coil away from the chosen area. In a microscope fitted with an MDS facility (for example, the JEOL 1200 EX) the lens settings for imaging the chosen area may be stored in the memory and brought back to the screen when required. The focus and astigmatism are corrected in the image mode on a nearby area, possibly at a higher magnification than required on the final image, and the electron beam is only returned to the chosen area once the shutter is open. This ensures that the specimen is subjected to radiation damage only for the length of time necessary for recording. The amount of defocus can be checked after the micrograph has been taken.

In the cryomicroscope in Berlin, the search for a suitable area was carried out by defocussing the diffraction pattern and using an image intensifier to magnify the low-magnification, bright-field image found in the diffuse centre spot. The beam was then blocked by a shutter installed above the specimen

plane until the deflector coils were switched on.

The JEOL 100C has no MDS facility, but it was possible to deflect the beam away from the chosen area by switching to the dark-field mode, pre-aligned to irradiate a different area to the bright-field.

3.3 Densitometry and Digitisation of Images.

Diffraction patterns for fading series were analysed with a Joyce Loeb1 Mk III densitometer, the operation of which is described in section 5.6. The slit width for sampling was kept as narrow as possible (a typical value was 1.0 mm.)

For image processing, densitometry was carried out by means of an Optronics rotating drum microdensitometer with a $25\mu \times 25\mu$ sampling aperture, the smallest available. Wherever the detail on the micrograph was too small for this aperture size to process, a 5x enlargement on to E.M. film was made, and this was analysed. This caused a reversal of contrast in the processed image.

Improved resolution was obtained when a Datacopy series 600 flat bed microdensitometer was used for scanning images. This had a 13μ sampling aperture and was linked to an IBM 16 bit personal computer.

3.4 Image Processing.

When a low-dose micrograph is taken, no periodic detail is visible at all due to the low signal-to-noise ratio, and the micrograph appears a uniform light grey. Information is contained in the emulsion, nevertheless; it is necessary, however, to extract by means of image processing.

For a transmitted image, a signal-to-noise ratio of q is related to the statistical probability p that a structure can be distinguished from its background, by:

$$p = q / (1 + q) \quad (3.1)$$

(Misell 1978)

For the purpose of the Rose equation (equation 2.11), a minimum signal-to-noise ratio of 5 is considered acceptable, although a periodic structure lowers this figure by a factor proportional to the square root of the number of repeating units in the sample (Fryer and Smith 1982). When the signal-to-noise ratio is less than unity, a technique such as Fourier filtering must be applied to interpret the information.

In electron optics the Fourier Transform is the mathematical expression used to analyse the variation in electrostatic potential of the specimen. Similarly in image processing the variation in optical density $j(x)$ of the photographic plate

with position x is written:

$$\begin{aligned} j(x) &= \sum_h J_h \exp \left(\frac{2 \pi i h x}{\ell} \right) \\ &= \sum_h J_h \cos \left(\frac{2 \pi h x}{\ell} \right) + i \sin \left(\frac{2 \pi h x}{\ell} \right) \end{aligned}$$

Each component sinusoidal wave has frequency $\nu = h / \ell$, where ℓ is the periodicity of $j(x)$, and J_h is a weighting factor known as the Fourier coefficient. A high frequency represents high resolution detail; thus the transform provides a measure of the resolution of a micrograph. The Fourier coefficients are complex numbers requiring both amplitude and phase information for their calculation, and the expression for the coefficients is:

$$J_h = 1/\ell \int_0^\ell j(x) \exp \left(-\frac{2 \pi i h x}{\ell} \right) dx$$

In terms of amplitude and phase,

$$J_h = |J_h| \exp (i\omega_h)$$

The phase information is lost in an optical diffractogram, in which the intensity of the peaks is proportional to $|J|^2$; a numerical transform preserves both the amplitude $|J|$ and the phase ω .

A more general form for the Fourier transform is:

$$J(\underline{v}) = \int j(\underline{r}) \exp(-2\pi i \underline{v} \cdot \underline{r}) d\underline{r}$$

where \underline{r} is a vector representing co-ordinates (x,y) in the image and \underline{v} represents two dimensional frequency in the transform. Its inverse transform is:

$$j(\underline{r}) = \int J(\underline{v}) \exp(2\pi i \underline{v} \cdot \underline{r}) d\underline{v}$$

When a direct transform is followed by an inverse transform, the original function is obtained:

$$\tau^{-1} \tau [J(\underline{v})] = \tau^{-1} [j(\underline{r})] = J(\underline{v}).$$

A modified Fourier Transform equation, the Fast Fourier Transform (FFT) is applied when the transform is calculated numerically (Misell 1975).

Fourier filtering is based on the fact that the transform of a periodic structure contains the structural information (amplitude and phase) concentrated in the peaks of the transform. These peaks together represent a projection of the reciprocal lattice. The noise on the other hand is distributed at random over the whole transform, and this may be

excluded by means of a mask, thus allowing the image to be reconstructed from the signal only.

Fourier filtration may be carried out at an optical bench. Monochromatic light from a laser source is diffracted by a specimen micrograph, and the unwanted noise from the resultant diffraction pattern is filtered out by means of a cardboard mask with holes cut out at the positions of the diffracted beams (Taylor and Lipson 1964). The image is then reconstructed by means of lenses and projected on to a screen. An analogous filtering technique may be carried out numerically: the intensities of the image micrograph, as measured by microdensitometry, are digitised and stored on magnetic tape. The "power spectrum" is then calculated mathematically from the digital data. The numerical transform calculates both $|J|$ and ω , the amplitude and phase of the Fourier Transform.

The two components making up the total Fourier Transform are the signal $S(\underline{v})$ and the noise $N(\underline{v})$. Thus:

$$J(\underline{v}) = S(\underline{v}) + N(\underline{v})$$

The original image may not be visible above the noise but the peaks of the power spectrum stand out clearly from the background. The image transform is then multiplied by a "mask" $M(\underline{v})$. This is a function of unit value at the peaks

of the transform, and zero elsewhere. $M(\underline{v})$ is a convolution of a reciprocal lattice function $L(\underline{v})$ and a "window function" $W(\underline{v})$ which describes the mask hole. The image transform then becomes:

$$J(\underline{v}) \times [L(\underline{v}) * W(\underline{v})] \quad (\text{Misell 1975})$$

For a perfect lattice, the window would be defined by only one lattice point, and the average would then be taken over the entire image. However, lattice distortions and imperfections in sampling cause broadening of the peaks (as they do in optical or electron diffraction) and so the holes in the mask are made larger, limiting the degree of averaging of the image.

When an inverse transform is performed on the modified image transform, the reconstructed image has the form:

$$j(\underline{r}) * [l(\underline{r}) \times w(\underline{r})],$$

where $l(\underline{r})$ is the lattice periodicity and $w(\underline{r})$ is a measure of the number of units averaged, and $*$ denotes convolution. A large window size corresponds to averaging over a small number of unit cells in the specimen.

A practical example of the technique of image processing is shown in Plate 1. The top left-hand picture shows an area

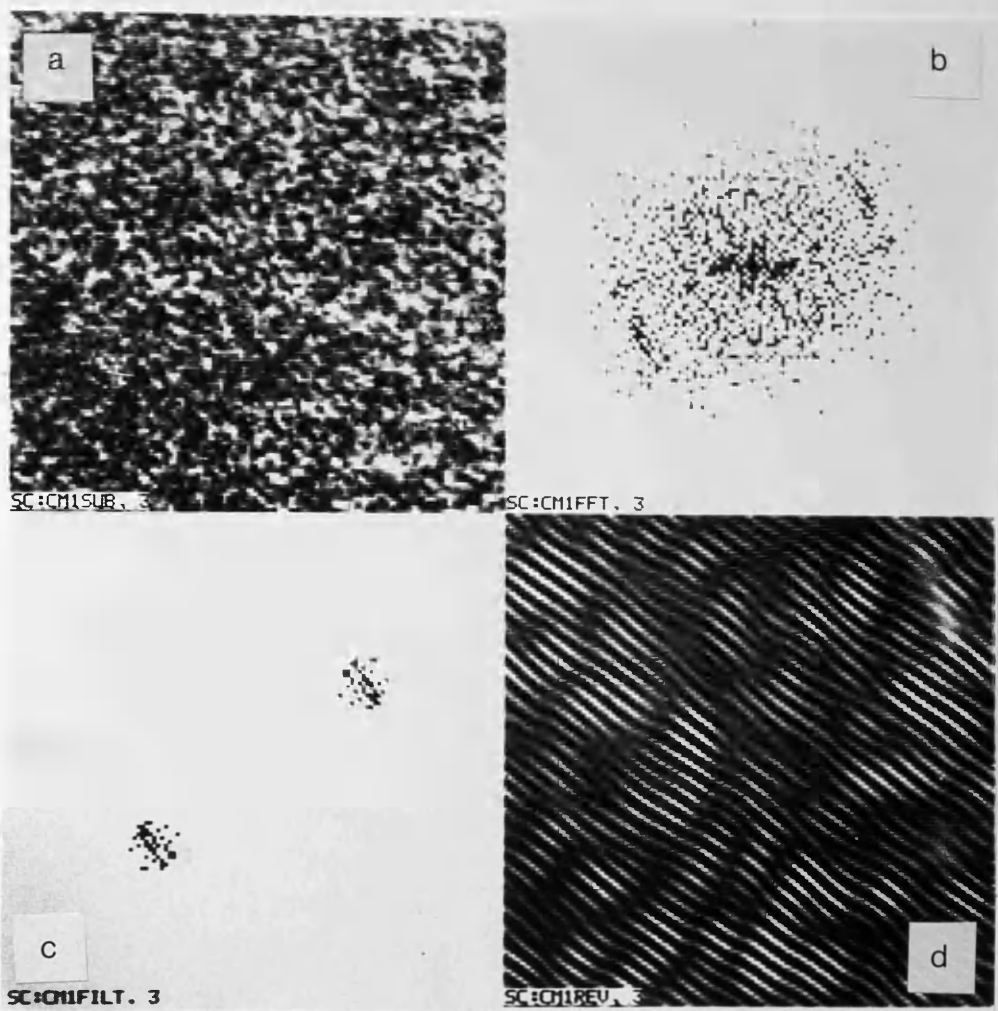


Plate 1 : The four stages of the Fourier reconstruction by the Imagic programme:

- (a) The digitised image,
- (b) The power spectrum,
- (c) The masked peaks of the power spectrum,
- (d) The reverse transform.

of digitised image, 128 x 128 picture elements in area, of a specimen of a substituted phthalocyanine. Its numerical transform is shown in picture (b). Two peaks can be distinguished among the noise.

The mask function is superimposed in picture (c), the radius of the "windows" having been chosen to include as much of the information contained in the peaks as possible, while excluding the background noise.

The inverse Fourier transform is shown in the fourth picture. The background noise has been removed, leaving an image in which the structure is visible.

It must be borne in mind that diffuse scattering carrying information about the structure may be lost in the masking process along with the random noise. A second pitfall of this type of image processing is that a mask superimposed on random noise alone will generate a spurious image, since a periodicity is imposed by the spacing of the mask windows. The random noise within each window is multiplied by one and undergoes the inverse Fourier Transform, creating a misleading image.

3.5 The Optical Bench.

As mentioned in Section 3.4, an optical bench may be used for the filtering and reconstruction of images. This type of

reconstruction was not necessary in this work since numerical methods were available; however, diffractions patterns obtained on an optical bench with a 1mW He/Ne laser source were used frequently as a measure of resolution of micrographs, to detect crystalline areas in low-dose images and to measure lattice spacings as images from their optical diffraction patterns.

A diagram of the optical bench is shown in Fig. 3.2.

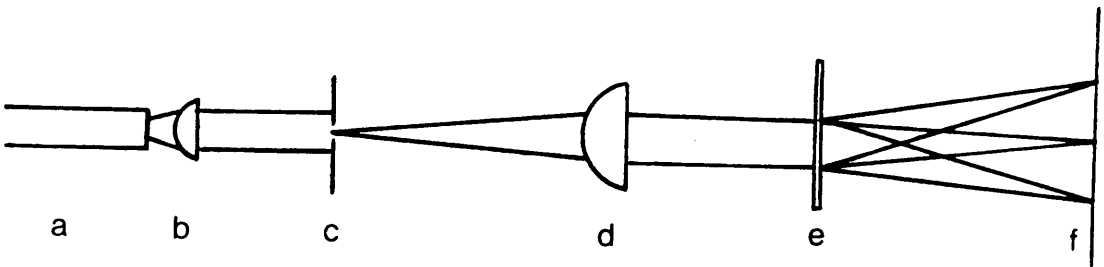


Fig. 3.2 The Optical Bench.

- a : 1 mW He/Ne laser
- b : Laser objective
- c : Pinhole
- d : Collimator lens
- e : Specimen micrograph
- f : Screen

CHAPTER 4;
EPITAXIAL PREPARATION OF SPECIMENS.

- 4.1 Epitaxy
- 4.2 Preparation of Epitaxial Films by Evaporation.
- 4.3 Thickness Measurement of Epitaxial Films in the
 "Deeko 250" Microscope.
- 4.4 Preparation of Paraffin Specimens.

CHAPTER 4: EPITAXIAL PREPARATION OF SPECIMENS.

4.1 Epitaxy.

An epitaxial layer is one in which an overgrowth is arranged on a substrate so that all of its crystals have the same orientation. Epitaxy may occur in many systems - for example, certain metals upon alkali halides, silicon upon sapphire, quartz, spinel or silicon, alkali halides upon other alkali halides or mica, and many others (Matthews 1975).

When the vapour of the overgrowth material meets the face of the substrate, nucleation must occur before a thin film will form. This involves the adsorption of sufficient molecules to form a nucleus of a critical size which is stable enough to grow before desorption occurs.

Nucleation tends to occur most readily at a defect in the substrate crystal, and the formation of stable clusters appears to depend on the rate of deposition, the temperature of the substrate and the energy relationship of the deposition process (Ueda and Mullin 1975).

Once clusters have been formed, they may grow by migrations of incoming atoms over the surface of the substrate to form islands of overgrowth material which eventually join up to form a continuous film.

For epitaxy to be energetically favourable, the lattice spacing of the overgrowth should correspond to a multiple of the lattice spacing of the substrate. The first monolayer of the overgrowth may become distorted to achieve this correspondence, or dislocations may occur between it and the substrate.

In 1949 Frank and van der Merwe studied epitaxial growth and concluded that the lattice of the overgrowth will deform to fit the substrate provided the degree of misfit is less than 9%. It is still possible, however, to deposit a monolayer at up to 14% misfit, forming a metastable state, provided the temperature is sufficiently low that the overgrowth does not acquire enough activation energy to form dislocations. The degree of misfit was defined as

$$P_0 = \frac{b - a}{a} \quad [4.1]$$

where a and b are the lattice spacings of substrate and overgrowth respectively. It was also pointed out that the exact critical misfits would vary according to the substrate and overgrowth material.

The orientation of the overgrowth also depends upon the nature of the substrate and overgrowth, and, in the case of molecular crystals of planar molecules, upon the angle which is made by the molecules with their column axis. Crystals may be orientated with their column axes parallel, perpendicular, or

at an angle to the substrate, depending on the interactions of crystal with substrate (Fryer 1979).

4.2 Preparation of Epitaxial Films by Evaporation.

Thin films of phthalocyanines and other polycyclic organic molecules were prepared under vacuum in an Edwards coating unit. Freshly-cleaved 100 faces of potassium chloride were suspended above a molybdenum boat containing crystals of the substance, and the chamber of the unit evacuated to about 10^{-6} torr. The boat was then heated to red heat until all the crystals had evaporated. It was found that when the substrate was warmed prior to evaporation, the proportion of evaporated molecules adhering to it varied considerably, making the film thickness difficult to estimate. When the crystal substrate was coated at room temperature the sticking of the film to the KCl face was more predictable, and the thickness of the film could be calculated from the formula

$$t = \frac{m}{4\pi r^2 \rho} \quad [4.2]$$

("Techniques for Electron Microscopy" ed. H. Kay, Blackwell 1965).

where

t = thickness of film

r = distance from boat to substrate

m = mass of material in boat

ρ = density of material

The crystal with the film could then be heated slowly to provide the energy for the molecules of the film to arrange themselves epitaxially.

The crystal could subsequently be covered with a layer of evaporated carbon by replacing the boat by a pair of carbon rods held together by springs and heated electrically to white heat; the crystal film with its carbon coat were then floated off on distilled water, washed and picked up on microscope grids.

For evaporated layers prepared in a similar manner in the Balzers coating unit in Berlin, a quartz thickness monitor was mounted in the belljar, level with the KCl substrate. This monitor consisted of a quartz crystal disc, the characteristic vibration frequency of which changed on being coated with an evaporated layer. A second crystal outside the system acted as a reference, and the frequency difference was displayed on a meter. An empirical relationship between thickness $t(\text{\AA})$, frequency difference $\Delta f(\text{Hz})$ and overgrowth density was given by the manufacturer as:

$$t = \frac{\Delta f}{\rho} \quad [4.3]$$

The quartz thickness monitor gave very different results from the thicknesses calculated by the mass of the evaporated crystals. Usually a lower thickness was registered by the quartz crystal, which is reasonable given that the formula yields the maximum thickness obtainable assuming that all the material sticks to the substrate on evaporation.

A link was observed between a material's density and the discrepancy between the calculated maximum thickness and the thickness registered by the monitor. Five types of material were prepared at room temperature by evaporation:

Table 4.A

	<u>Density</u>	<u>Thickness by Calcn.</u> <u>Thickness by Δf</u>	<u>"Sticking coefficient"</u>
Fully chlorinated			
Cu phthalocyanine (4 samples)	2.1	8.20 \pm 1.46	0.12
8.6% Cl-Cu-Pc (3 samples)	\sim 1.6	3.36 \pm 0.15	0.30
2.2% Cl-Cu-Pc (4 samples)	\sim 1.6	3.22 \pm 0.36	0.31
Copper phthalocyanine (1 sample)	1.6	3.20	0.31
Metal-free Pc (15 samples)	1.4	1.23 \pm 0.40	0.81

With five samples representing three different densities, the exact relationship between the sticking coefficient and the density of the crystals could not readily be derived; a linear dependence does not seem to apply. The amount of material adhering to the substrate probably depends on many factors such as the temperature of evaporation and of the substrate, the rapidity of heating, and the fineness of the powdered crystals in the boat, as well as the nature of the materials involved.

However, the grouping of results from the quartz thickness monitor according to density does indicate consistency in the readings from the monitor.

4.3 Thickness measurement of Epitaxial Films in the "Deeko 250" Microscope

Thickness determination was carried out using the relationship quoted in Reimer (1975):

$$\text{Transmission } T = I/I_0 = \exp (- x/x_k), \quad [4.4]$$

where I and I_0 are beam intensities with and without the specimen respectively, x is the mass thickness ($= \rho t$, where ρ is the density and t the thickness of the specimen) and x_k depends on the objective aperture, the electron energy and the atomic number of the material. This is only valid for simple

scattering and provided the density of the specimen is the same as that of the bulk material, but it is used here in its simple form:

$$\text{Thickness} = x_k \ln I_0/I \quad [4.5]$$

For the "Deeko 250" (see section 3.5) with the 50μ objective aperture inserted, the value of x_k has been calibrated as 29.

A specimen of metal free phthalocyanine on carbon film with a second half-covering was chosen. Its thickness was 110\AA by formula, and 100\AA by the quartz thickness monitor. Current densities were measured in the image plane, and I_0 , I_s and I_d refer to intensities at a hole in the specimen, at an uncoated area and at a coated one respectively. The results obtained are shown in table 4.B

Table 4.B.

Intensity Measurements and Thickness Calculation for Metal-free Phthalocyanine, Specimen K2

(pA)			\log_e		$\mu\text{g}/\text{cm}^2$		\AA	
I_0	I_s	I_d	I_0/I_s	I_0/I_d	ρt_s	ρt_d	t_s	t_d
0.31	0.29	0.27	0.067	0.138	1.943	4.002	138	286
1.0	0.94	0.875	0.062	0.133	1.794	3.872	128	276
1.0	0.93	0.87	0.073	0.139	2.117	4.031	151	288
2.6	2.40	2.25	0.080	0.144	2.320	4.176	166	298
6.1	5.65	6.30	0.077	0.141	2.233	4.089	160	292
mean							149	288
							± 16	± 8

The thickness of the ovalene film used for the fading-series at different temperatures (Section 5.5) was measured in a similar manner:

$$\text{Current at hole } (I_0) = 3.2 \times 10^{-11} \text{ A.}$$

$$\text{Current on film } (I_s) = 2.7 \times 10^{-11} \text{ A.}$$

$$\mathcal{X} = \mathcal{X}_k \ln \frac{3.2}{2.7} = 4.93 \times 10^{-8} \text{ } \mu\text{g}/\mu\text{m}^2$$

$$\rho = 1.8 \text{ g/cm}^3$$

$$d = \frac{\mathcal{X}}{\rho} = \frac{4.93 \times 10^{-8} \times 10^6}{1.8} = 0.027 \text{ } \mu\text{m.}$$

$$= 270 \text{ \AA}$$

The thickness of the ovalene film was estimated at 70-100 Å; the thickness of the carbon film would partially account for the difference in values.

4.4 Preparation of Paraffin Specimens.

(a) The hk0 orientation.

Lozenge-shaped crystals of paraffin, in which the chain axes are normal to the lozenge face were prepared by dissolving the paraffin crystals in warm n-hexane and depositing small drops of the solution on to carbon-coated electron microscope grids. The concentration of the solution was adjusted until an even distribution of monolamellar crystals was obtained. The thickness of these crystals was thus equal to the chain length, and the electron beam passed parallel to the c-axis of the

unit cell to form an (001) projection on the image plane, as illustrated in Fig. 4.1.

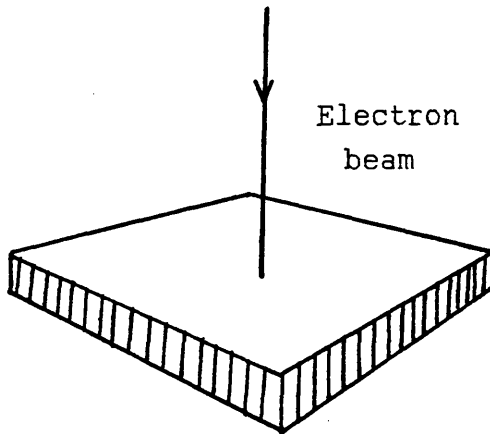


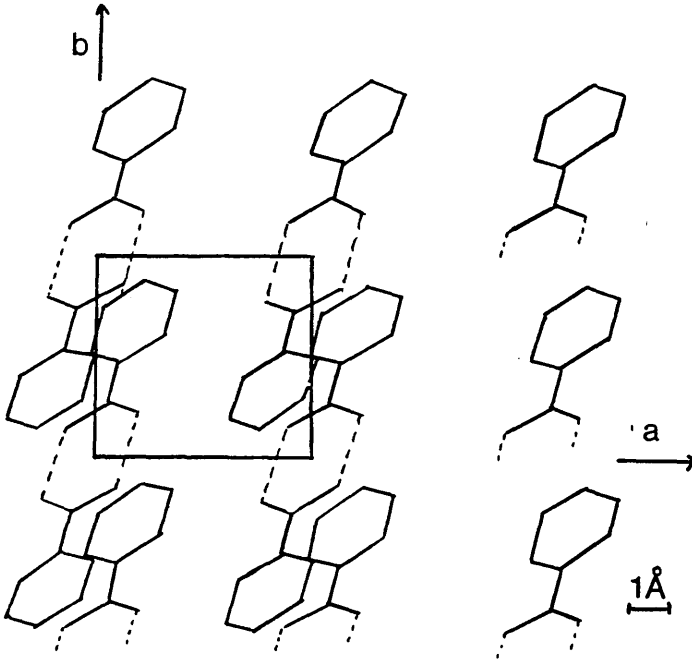
Fig. 4.1 : Solution-grown crystal of a paraffin.

(b) The 0k1 orientation.

Simple solution crystallisation does not produce a paraffin crystal which can be viewed in the 0k1 projection in the electron microscope, that is, with the long chain axis parallel to the support grid, perpendicular to the beam.

This is achieved by an epitaxial preparation method, as used for paraffins by Wittmann et al (1983) and Dorset (1985) and for several polymers by Wittmann and Lotz (1981) and Wittmann and Manley (1978).

The substrate used for this application was benzoic acid (m.pt. 122.4°C) which may be recrystallised to form large flat crystals with $\{001\}$ planes uppermost:



(after Wittmann et al 1983).

Fig. 4.2.

To prepare the specimens, crystals of the required paraffin were mixed with benzoic acid crystals, with the latter greatly in excess. The mixture was then sandwiched either between two glass microscope slides or between two freshly divided sheets of mica. An aluminium bar was heated at one end to form a temperature gradient, and the sandwich was slid slowly up and down the bar causing the crystals to melt and solidify. On cooling, the benzoic

acid crystallised from the melt first, and the paraffin then formed lath-shaped crystals on the newly formed (001) faces of the acid. The paraffin chain axis lies parallel to the a-axis in Fig.4.2 (Wittmann et al 1983). The mismatch between the paraffin and the benzoic acid b-axes is

$$P_o = \frac{b_{\text{par}} - b_{\text{BA}}}{b_{\text{BA}}} \times 100 = \frac{4.96 - 5.14}{5.14} \times 100 = -3.5\%$$

The mismatch in the a-direction is calculated using two paraffin subcells (chain zig-zags) as the repeating unit:

$$P_o = \frac{2c_{\text{subcell}} - a_{\text{BA}}}{a_{\text{BA}}} \times 100 = \frac{5.08 - 5.52}{5.52} \times 100 = -8.0\%$$

Once cool, the two slides or mica sheets were separated and coated with carbon and the combined film was floated off on a distilled water surface to be picked up on electron microscope grids. An alternative method was to include some carbon-coated grids in the sandwich. Once the slides had been cooled and separated they were placed under vacuum overnight to remove the benzoic acid by sublimation. The grids could then be peeled off the slides and used immediately.

The resultant crystals were orientated orthogonally to the solution-grown crystals enabling all three unit cell dimensions to be examined by microscopy:

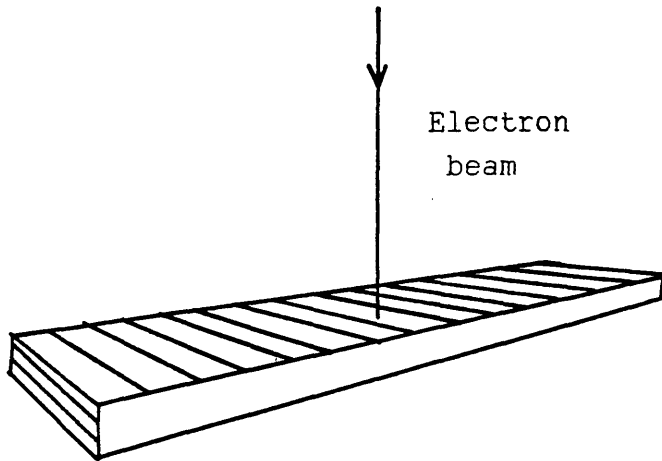


Fig. 4.3 : Epitaxially-grown crystal (after Dorset 1985)

Solid solutions of pairs of paraffins were prepared by mixing together the components in the desired proportions, then melting the mixture in an oil bath for two hours to mix the components thoroughly. After cooling, the epitaxial preparation was carried out exactly as for single-component systems. The structure of solid solutions of paraffins will be discussed in Chapter 6.

Paraffins Used in Experimental Work.

	<u>Source</u>	<u>Purity %</u> (label)	<u>M.Pt.</u> (label)	<u>M.Pt.</u> (Obs.)
$nC_{32}H_{66}$	Aldrich Chem. Co.	97%	68-70 ⁰	68-70 ^o
$nC_{33}H_{68}$	Fluka AG	Pure	*	69-71 ⁰
$nC_{34}H_{70}$	Fluka AG	Pure	70-73 ⁰	71-73 ⁰
$nC_{36}H_{74}$	Aldrich Chem Co.	Recryst		74-76 ⁰
$nC_{37}H_{76}$	Fluka AG	V.Pure (>99%)	77-79 ⁰	77-79 ⁰
$nC_{38}H_{78}$	Fluka AG	Pure	77-79 ⁰	77-79 ⁰
$nC_{44}H_{90}$	Ventron GmbH	96%		84-86 ⁰

* Theoretical melting point 71.8⁰ (Piesczek).

CHAPTER 5.

RADIATION DAMAGE RESULTS and DISCUSSION.

- 5.1 Radiation Damage Measurements at Room Temperature.
- 5.2 Extinction Dose Results for Metal-free Phthalocyanine.
- 5.3 Extinction Dose Results for Coronene and Ovalene.
- 5.4 Results of Extinction Dose Measurements at Very Low Temperatures (<15K).
- 5.5 Radiation Damage Results from the Variable-Temperature Electron Microscope "Deeko 250".
- 5.6 Calculation of D_e for Metal-Free Phthalocyanine.
- 5.7 The Dependence of Radiation Sensitivity on the Number of Layers in a Langmuir-Blodgett Film.

CHAPTER 5: RADIATION DAMAGE RESULTS and DISCUSSION.

5.1 Radiation Damage Measurements at Room Temperature

Room temperature studies were carried out on specimens of coronene, ovalene, and metal-free phthalocyanine, whose structures are shown in Figs. 5.1, 5.2 and 5.3 respectively.

Specimens were prepared as described in Section 4.2. Lattice images of coronene and ovalene are shown in Plates 2 and 3; the crystals are orientated with the ac face in the image plane.

In each case the specimen film was coated with evaporated carbon while still on the KCl substrate, then the coated film was floated off on a distilled water surface. Attempts were made to turn the film over on the water with a glass slide, in order to pick up the film on grids with the carbon layer between the specimen and the grid, but this was prevented by the surface tension of the water in spite of attempts to reduce interaction by means of a surfactant. The films were then washed, picked up on clean grids with the carbon uppermost, dried, and given a half carbon coat on the reverse side by masking half of the grid during evaporation, as depicted in Fig. 5.4.

The radiation dose necessary to destroy the lowest-order diffraction spots was measured by judging by eye the point at

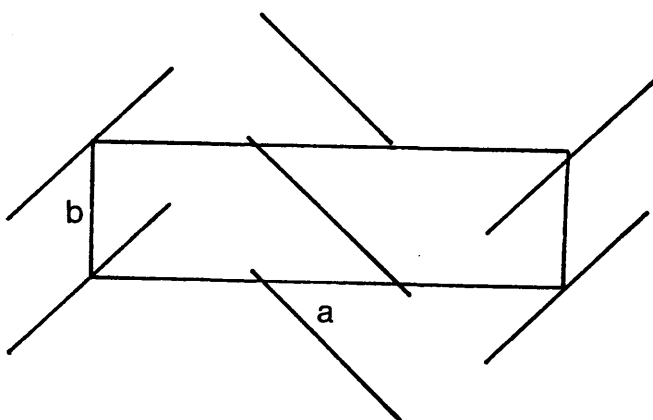
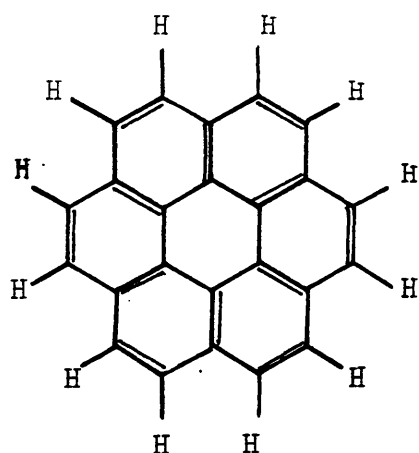


Fig. 5.1 CORONENE.

$C_{24}H_{12}$

mol. wt. = 300.3

density = 1.377

monoclinic unit cell, $P2_1/a$; 2 molecules/unit cell

$a = 16.10 \text{ \AA}$

$b = 4.695 \text{ \AA}$

$c = 10.15 \text{ \AA}$

$\beta = 110.8^\circ$

J.K. Fawcett & J. Trotter, Proc. Roy. Soc. A289 (1965) 366

J.M. Robertson & J.G. White, J. Chem. Soc. (1945) 6.7

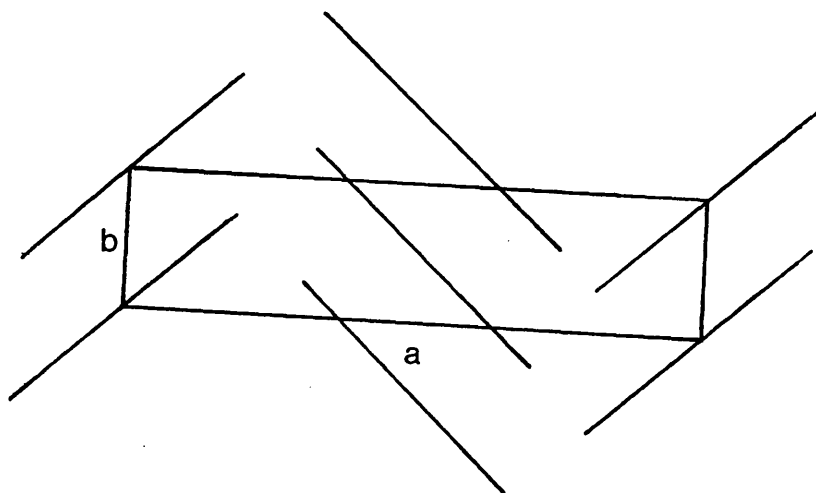
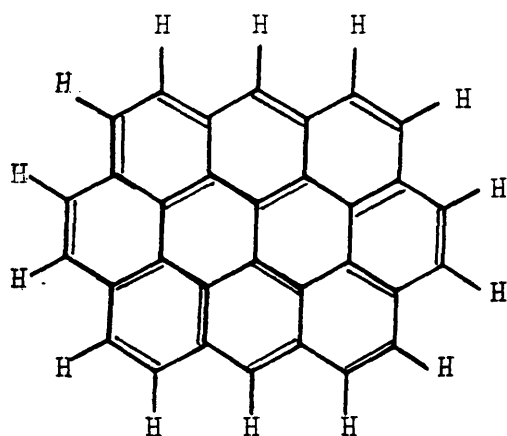


Fig. 5.2 OVALENE.

$C_{32}H_{14}$

mol. wt. = 398.4

density = 1.496

monoclinic unit cell, $P2_1/a$; 2 molecules/unit cell

$a = 19.47 \text{ \AA}$

$b = 4.70 \text{ \AA}$

$c = 10.12 \text{ \AA}$

$\beta = 105.0^\circ$

R.G. Hazel & G.S. Pawley, *Z. Kristallogr.* 137 (1973) 159

D.M. Donaldson & J.M. Robertson, *Proc. Roy. Soc.* A220 (1953) 157

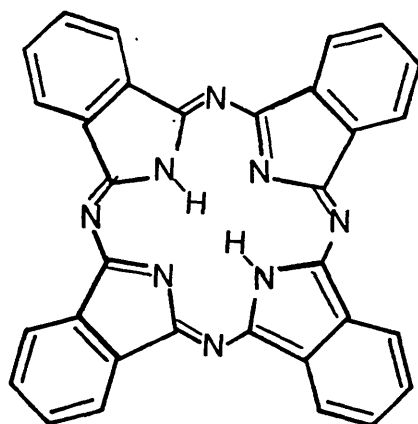


Fig. 5.3 METAL-FREE PHTHALOCYANINE.

C₃₂H₁₈N₈

mol. wt. = 514.55

density = 1.445

monoclinic unit cell, P2₁/a; 2 molecules/unit cell

a = 19.85 Å

b = 4.72 Å

c = 14.8 Å

β = 122.25°

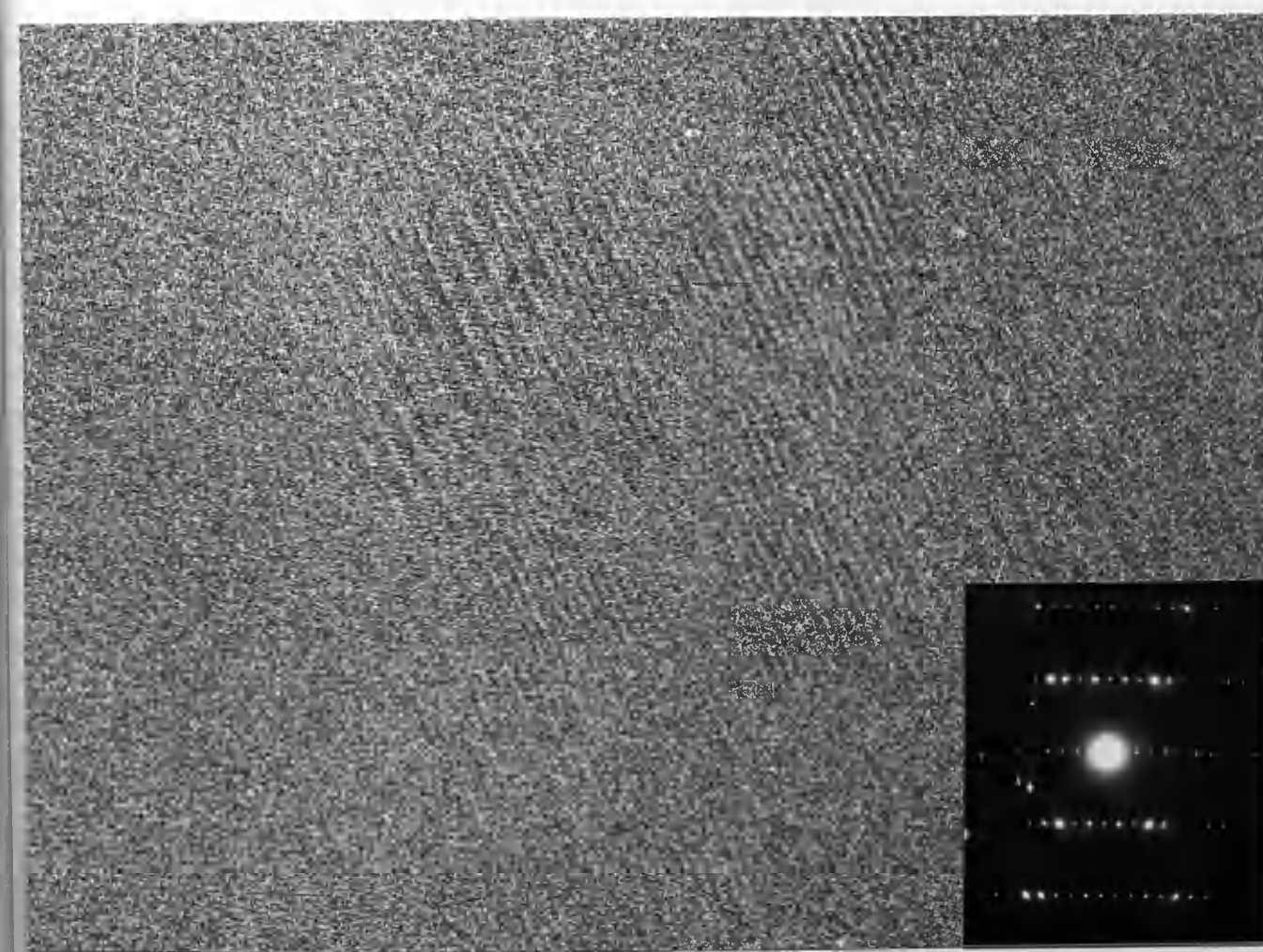
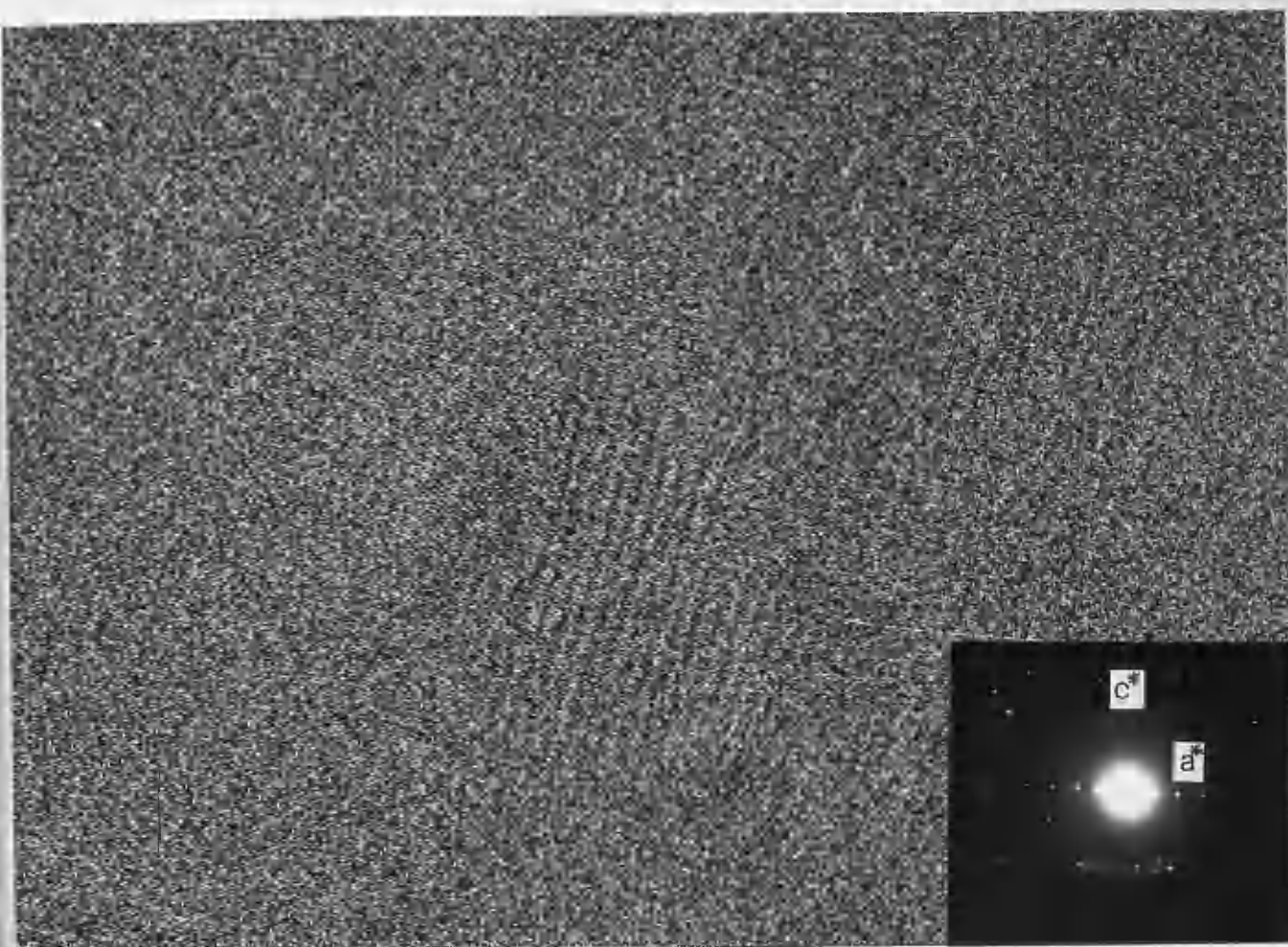
J.M. Robertson, J. Chem. Soc. (1936) 1195



Fig. 5.4 Specimen prepared for radiation damage experiments.

PLATE 2 Lattice image of coronene in an ac projection
x 1,950,000
Lattice spacings: 14.5 Å
4.47 Å

PLATE 3 Lattice image of ovalene in an ac projection
x 1,950,000
Lattice spacings: 18.7 Å
 8.6 Å
 4.37Å



which the diffraction pattern was completely destroyed, and a stop-watch was used for timing.

This electron dose will be referred to in the following results section as the "extinction dose" as this is the term used by Holland (1984); it is not to be confused with D_e , the electron dose required to cause the diffraction spots to fade to $\frac{1}{e}$ of their original intensity (see Section 5.6).

The radiation was measured by means of a copper collector plate which was situated in the plane of the viewing screen and linked to a milliammeter. The electron dose rate incident on the specimen plane could then be calculated by the following formula:

$$\text{Dose rate} = \frac{\text{Magnification}^2 \times \text{current (mA)}}{\text{area of collector plate}}$$

and converted into coulombs/cm². A back-scattering factor of 30% from the copper was assumed (Nicholson 1981).

5.2 Extinction Dose Results for Metal-Free Phthalocyanine.

The specimens used were prepared as described in Chapter 4, and half-coated with evaporated carbon (approximately 100 Å thick, measured by quartz thickness monitor). They were examined in the JEOL 100B at the Fritz-Haber-Institut, which was fitted with the same copper collector plate on the image plane as was

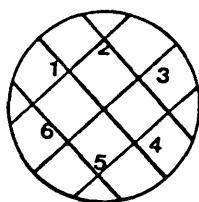
used in the JEOL 100C at Glasgow for similar experiments on coronene and ovalene (Section 5.3).

The exact boundary between the coated and the uncoated halves of the grid was not visible, but at least ten fading-times were measured for each of the six areas spread over the whole grid - a noticeable difference in specimen lifetime was expected to indicate the position of the carbon layer. The results are shown in Table 5.A.

Table 5.A. Results of Extinction Dose Measurements of
Metal-free Phthalocyanine (JEOL 100B)
Room Temperature

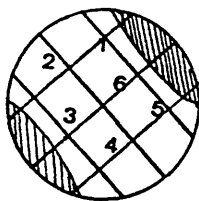
(i) Specimen P2 (Thickness, by weight only, 60 Å).

Position on Specimen Monitor Area Mean ext-dose (C/cm^2)



1	0.107	± 0.001
2	0.095	± 0.007
3	0.108	± 0.022
4	0.093	± 0.018
5	0.099	± 0.013
6	0.089	± 0.017

(ii) Specimen M4 (Thickness by weight 140 Å, by Δf 140 Å).



1	0.124	± 0.008
2	0.102	± 0.013
3	0.108	± 0.011
4	0.126	± 0.021
5	0.108	± 0.013
6	0.124	± 0.01

5.3 Extinction Dose Results for Coronene and Ovalene

Similar measurements were made on specimens of coronene and ovalene, sampling areas from the periphery and nearer the centre of the grid. The variation in beam-sensitivity at different areas did not appear to be significant; no two distinct groups of values were observed which might delineate a carbon-coated and an uncoated semi-circle (see Tables 5.B and 5.C). However, the specimens did appear to contain local variations in thickness.

The ovalene in this experiment appears to be less stable under the beam than the coronene. This is likely to be a consequence of a difference in film thickness, as the larger aromatic system would be expected to sustain a larger electron dose. The phthalocyanine is more stable to the beam than the coronene or the ovalene, but a quantitative comparison cannot be made here because of uncertainty in the thicknesses of the coronene and ovalene samples.

Discussion.

In contrast to the results of Holland (1984) and Fryer and Holland (1983), there does not appear to be a significant difference between one area of a grid and another, and there is no obvious boundary between the sandwiched area and the area with carbon on one side only.

Fryer and Holland also measured "Protection Factors" of between 3.0 and 1.4 for carbon coated metal-free phthalocyanine, depending on the thickness of the film (80-200Å). This protection factor decreases as specimen thickness increases, leading to the conclusion that the thick film acts as a "coating" on itself and that the effect of the extra layer of carbon becomes less significant.

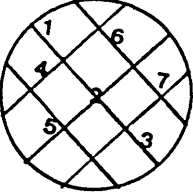
One of the main objects of the present radiation-damage experiments was to determine whether the protection factor postulated by Fryer and Holland in their room-temperature work was still effective as the temperature of the specimen was lowered, or whether the "freezing in" effect of the low temperature prevented secondary damage effects in the specimen to such an extent that the carbon coat made no further difference.

However, the above measurements do not show any evidence of the protective effect of a carbon coat, even at room temperature, although it is clear that variations in the specimen thickness do have a marked effect. If the carbon coat has no significant effect on damage rates at room temperature, it is unlikely that it will have any effect at low temperature!

Nevertheless, the studies of half-carbon coated organic specimens were continued at lower temperatures.

Table 5.B Results of Extinction Dose Measurements of Coronene
at Room Temperature (JEOL 100C)

(i) Specimen 1 (Thickness unknown, estimated 100-200 Å)

Position on Specimen Monitor	Area	Mean ext-dose (C/cm^2)	
	1	8.09×10^{-2}	$\pm 0.55 \times 10^{-2}$
	2	14.38×10^{-2}	$\pm 4.04 \times 10^{-2}$
	3	12.03×10^{-2}	$\pm 1.59 \times 10^{-2}$
	4	11.91×10^{-2}	$\pm 2.07 \times 10^{-2}$
	5	11.05×10^{-2}	$\pm 2.15 \times 10^{-2}$
	6	10.98×10^{-2}	$\pm 2.46 \times 10^{-2}$
	7	10.09×10^{-2}	$\pm 0.99 \times 10^{-2}$

(ii) Specimen 2 (As above).

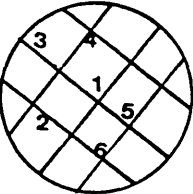
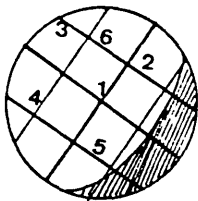
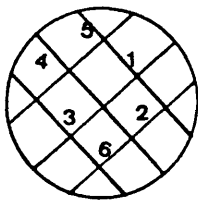
	1	10.19×10^{-2}	$\pm 2.79 \times 10^{-2}$
	2	13.05×10^{-2}	$\pm 1.46 \times 10^{-2}$
	3	10.92×10^{-2}	$\pm 1.60 \times 10^{-2}$
	4	12.27×10^{-2}	$\pm 5.28 \times 10^{-2}$
	5	8.98×10^{-2}	$\pm 0.90 \times 10^{-2}$
	6	10.05×10^{-2}	$\pm 1.05 \times 10^{-2}$

Table 5.C Results of Extinction Dose Measurements of Ovalene
at Room Temperature (JEOL 100C)

(i) Specimen 1 (approx. 100Å thick).

Position on Specimen Monitor	Area	Mean ext-dose (C/cm^2)	
	1	7.13×10^{-2}	$\pm 1.11 \times 10^{-2}$
	2	2.24×10^{-2}	$\pm 2.63 \times 10^{-2}$
	3	7.67×10^{-2}	$\pm 2.15 \times 10^{-2}$
	4	8.31×10^{-2}	$\pm 2.13 \times 10^{-2}$
	5	7.27×10^{-2}	$\pm 0.39 \times 10^{-2}$
	6	6.91×10^{-2}	$\pm 0.47 \times 10^{-2}$

(ii) Specimen 2 (approx. 100Å thick).

	1	9.44×10^{-2}	$\pm 2.58 \times 10^{-2}$
	2	7.37×10^{-2}	$\pm 1.28 \times 10^{-2}$
	3	6.47×10^{-2}	$\pm 0.82 \times 10^{-2}$
	4	7.38×10^{-2}	$\pm 1.76 \times 10^{-2}$
	5	8.55×10^{-2}	$\pm 1.66 \times 10^{-2}$
	6	7.95×10^{-2}	$\pm 1.64 \times 10^{-2}$

5.4 Results of Extinction Dose Measurements at Very Low Temperatures (<15K)

In the room temperature experiments, the grids were not placed in the specimen holder with the carbon-coated half in a predetermined orientation, as it was expected that the position of the carbon-coated semi-circle would be clear from the dose-measurements as described by Holland (1984). As it became clear that this method of finding the carbon coat was not reliable, all further experiments were carried out with the carbon-coated half clearly marked on the rim of the grid and positioned in the specimen stage in a known orientation.

The electron doses required to destroy completely the diffraction patterns of metal-free phthalocyanine, coronene and ovalene were measured at approximately 10K in the helium-cooled stage of the cryomicroscope in Berlin, and the results are tabulated in Table 5.D.

The differences in results between the coated and the uncoated specimens do not appear to be significant. Approximate protection factors are given for the effect of lowering the specimen temperature from 300K to ~ 10K.

Table 5.D Results of Extinction Dose Measurements at Very Low Temperatures (<15K).

(i) Metal-free Phthalocyanine.

<u>Specimen.</u>	<u>Thickness</u>	<u>Ext-dose C/cm²</u>	<u>Ext-dose C/cm²</u>
		(coated)	(uncoated)
Q3	By wt. 100Å, Δf60Å	0.609 ± 0.054	0.739 ± 0.052
J1	By wt. 100Å, Δf60Å	0.684 ± 0.036	0.688 ± 0.050
J3	By wt. 100Å, Δf60Å	0.695 ± 0.048	0.755 ± 0.052
K1	By wt. 110Å, Δf100Å	1.106 ± 0.074	1.130 ± 0.107

Protection factor [compared to room temperature result, Table 5A(i)] of the order of 7.

(ii) Coronene (approximately 100Å thick)

<u>Ext-dose (coated)</u>	<u>Ext-dose (uncoated)</u>
0.55 ± 0.06 C/cm ²	0.62 ± 0.12 C/cm ²

Low-temperature protection factor ~ 5.3 (ref. Table 5.B)

(iii) Ovalene (approximately 100Å thick)

<u>Ext-dose (coated)</u>	<u>Ext-dose (uncoated)</u>
0.60 ± 0.03 C/cm ²	0.70 ± 0.07 C/cm ²

Low-temperature protection factor ~ 8.5 (ref. Table 5.C)

5.5 Radiation Damage Results from the Variable-Temperature Electron Microscope "Deeko 250".

This microscope has a specimen stage which can be set at any temperature between room temperature and 9K. Measurements were made with an accelerating voltage of 100 kV.

Specimens studied were:

- (a) Ovalene, evaporated on to a cold substrate, annealed for 30 minutes at 150°C . Thickness by formula 70\AA .
- (b) Coronene, evaporated on to a cold substrate and annealed for 30 minutes at 100°C . Thickness by formula 100\AA .
- (c) Metal-free phthalocyanine, evaporated on to a cold substrate and annealed for 30 minutes at 200°C . Thickness by formula = 140\AA ; thickness by quartz monitor = 140\AA , and
- (d) Metal-free phthalocyanine, prepared as in (a). Thickness by formula 100\AA , thickness by quartz monitor 60\AA .

Tables 5.E and 5.F and Figs. 5.5 and 5.6 show the results obtained for the measurement of the time taken for complete destruction of the first order diffraction spots for ovalene and coronene respectively, at a series of temperatures from

300K down to 9K. Standard deviations are not shown as insufficient data were collected to make these significant. However, the results lie on smooth curves with little apparent difference between the values for the coated and uncoated halves of the specimens; certainly there is no evidence for a protection effect of the carbon at high temperature which diminishes as the temperature is lowered.

Table 5G and Fig 5.7 (a and b) illustrate the corresponding results for the two samples of metal-free phthalocyanine; again, there is little evidence for protection against radiation damage by a carbon coating at any temperature, although the protection afforded by lowering the temperature is apparent. As discussed in Section 2.4, there is some controversy over whether a significant gain in specimen lifetime is obtained by cooling to below liquid nitrogen temperature; the gains obtained in the above experiments are shown in Table 5H.

Table 5.E. (see Fig. 5.5)Extinction Dose Results: (Deeko 250).Ovalene

<u>Temperature(K)</u>	<u>C/cm² coated</u>	<u>C/cm² uncoated</u>
295	0.333	0.347
200	0.504	0.503
150	0.536	0.496
100	0.873	0.854
50	1.212	1.415
10	4.004	4.243

Table 5.F. (see Fig. 5.6)Coronene

295	0.359	0.444
250	0.650	0.480
200	0.547	0.457
150	0.651	0.557
100	0.809	1.057
50	1.176	1.194
10	1.761	1.818

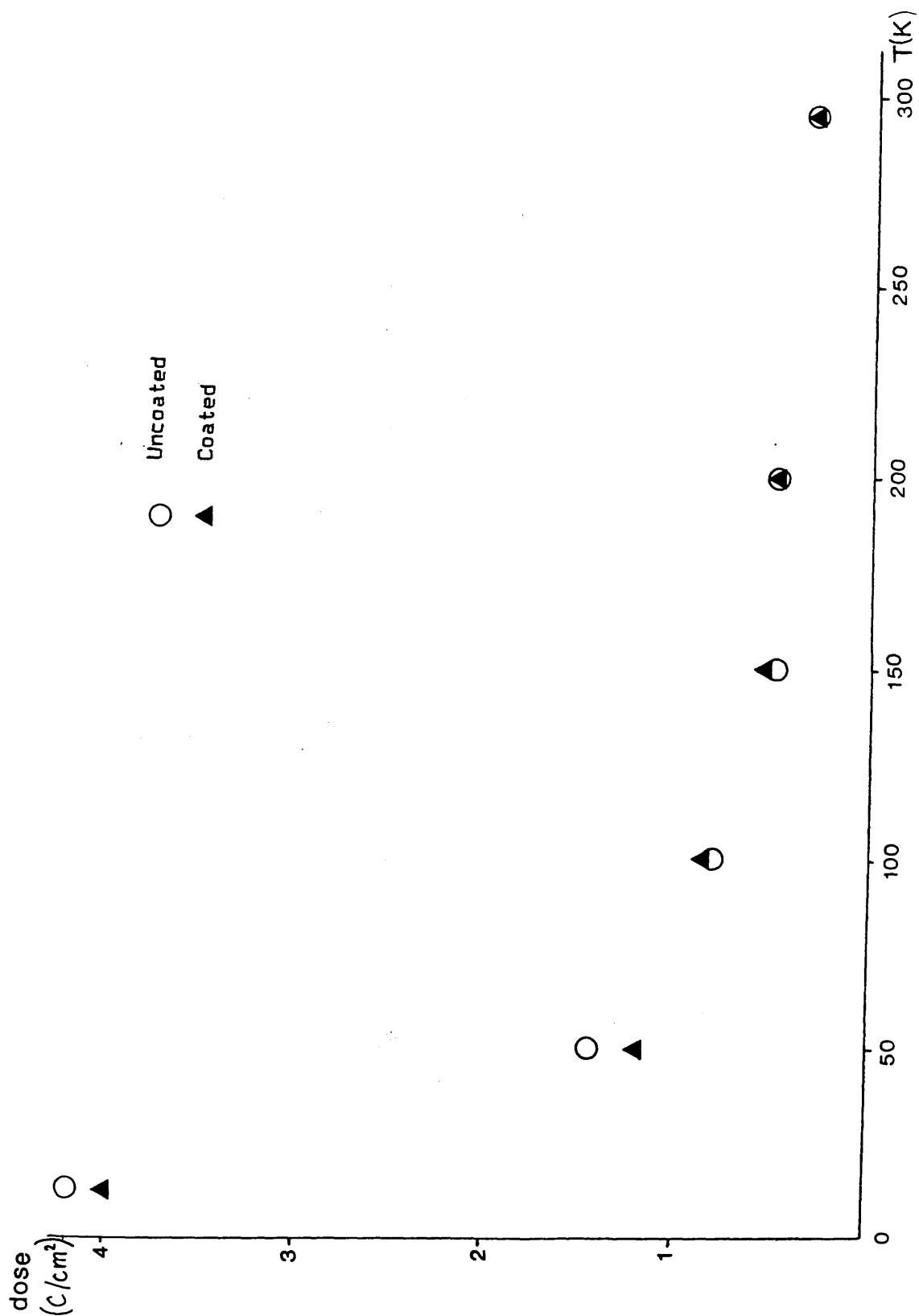


Fig. 5.5

Plot of the electron dose against temperature for destruction of the diffraction pattern for coated and uncoated areas of ovalene.

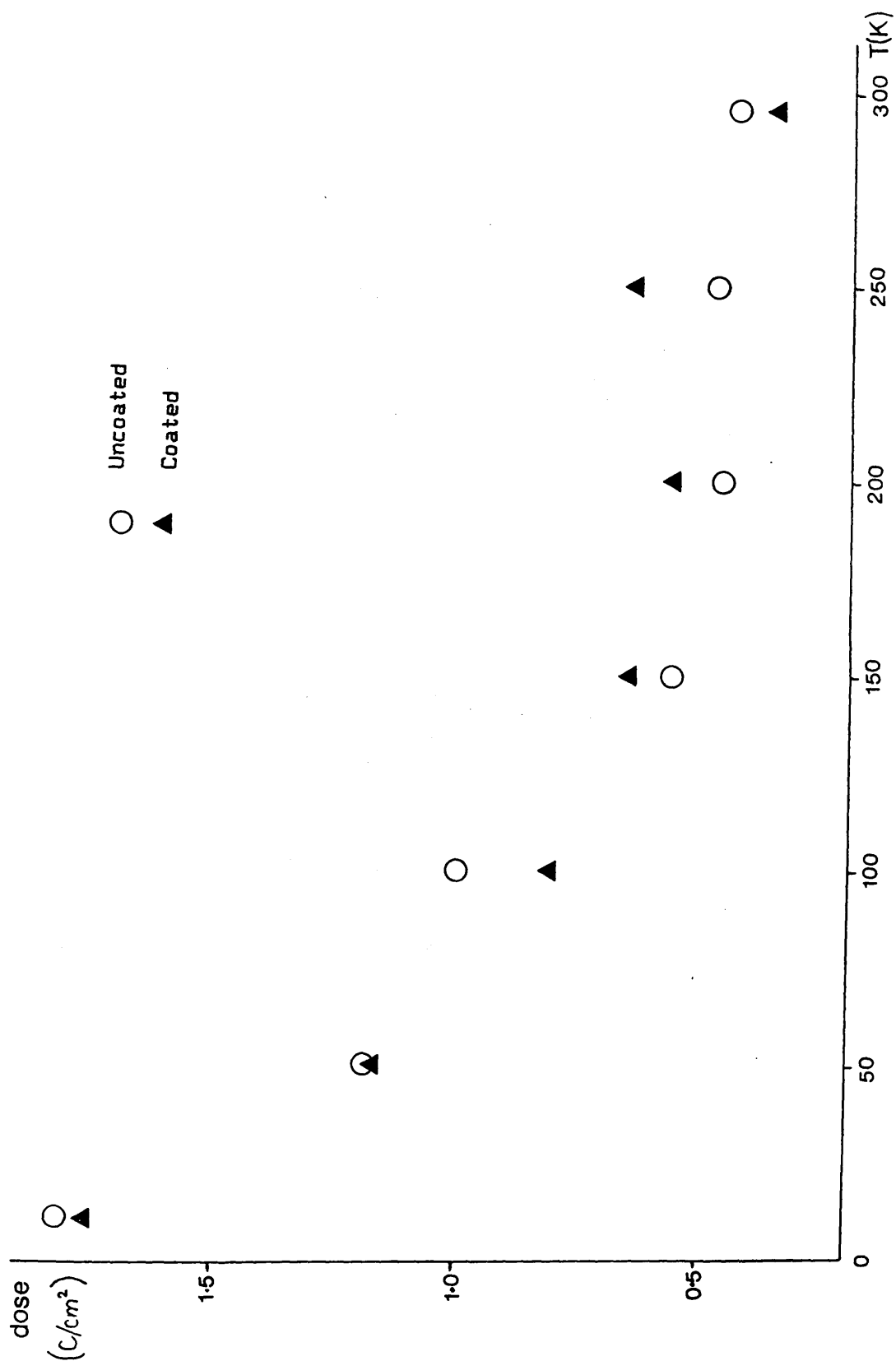


Fig. 5.6 Plot of the electron dose against temperature for destruction of the diffraction pattern for coated and uncoated areas of coronene.

Table 5.G (Deeko 250)Results for Metal-free Phthalocyanine.(i) 140Å by weight and by Δf .

<u>Temperature.</u>	<u>C/cm² coated</u>	<u>C/cm² uncoated</u>
295	0.319	0.320
250	0.357	0.369
200	0.484	0.464
150	0.439	0.526
100	0.648	0.676
50	0.860	0.846
10	0.919	0.999

(ii) 60Å by weight only.

295	0.148	0.187
250	0.233	0.204
200	0.289	0.287
150	0.430	0.429
100	0.400	0.503
50	0.770	0.810
10	0.966	1.117

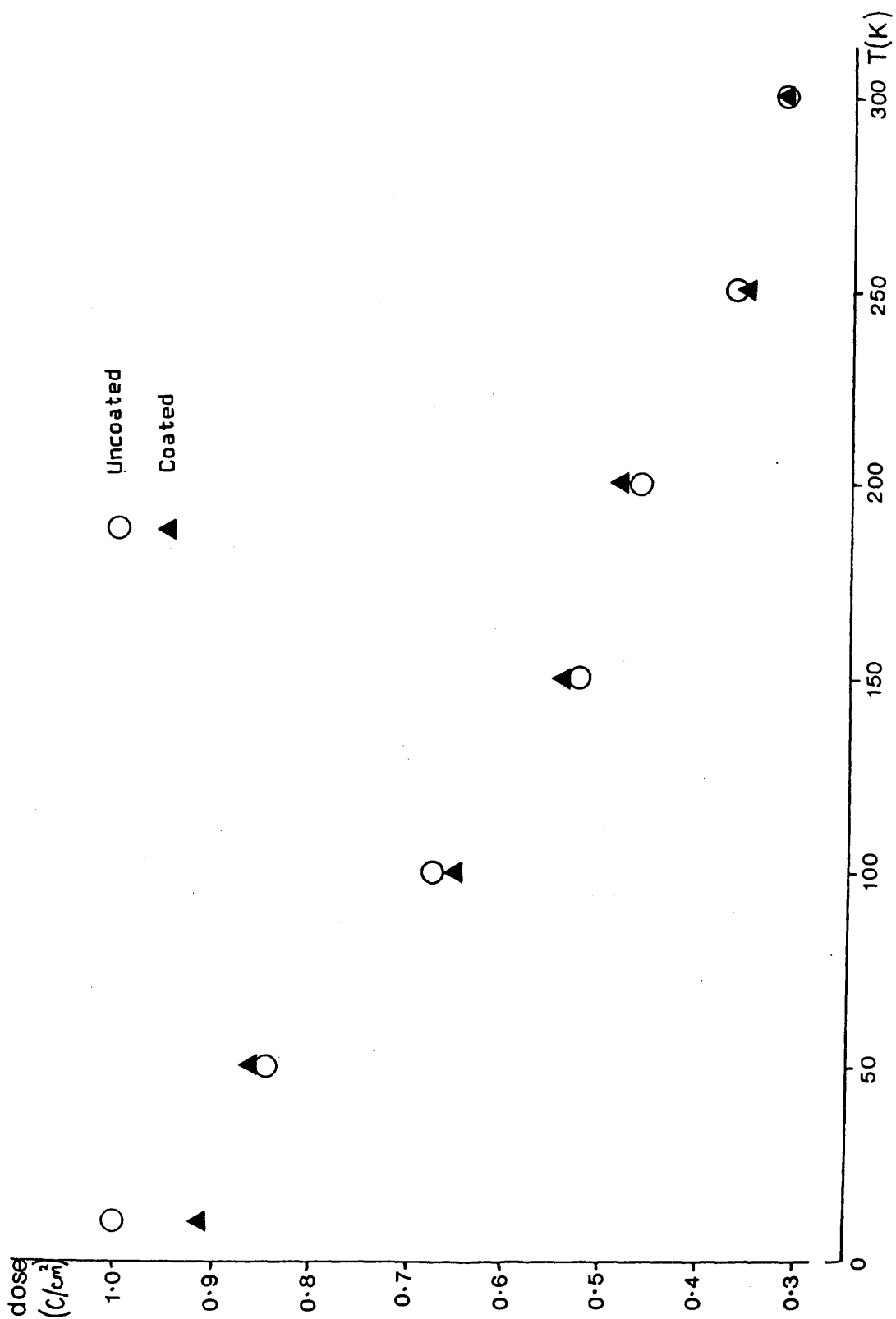


Fig. 5.7(a) Plot of the electron dose against temperature for destruction of the diffraction pattern for coated and uncoated areas of metal-free phthalocyanine (thickness by weight 140Å, by Δf 140Å).

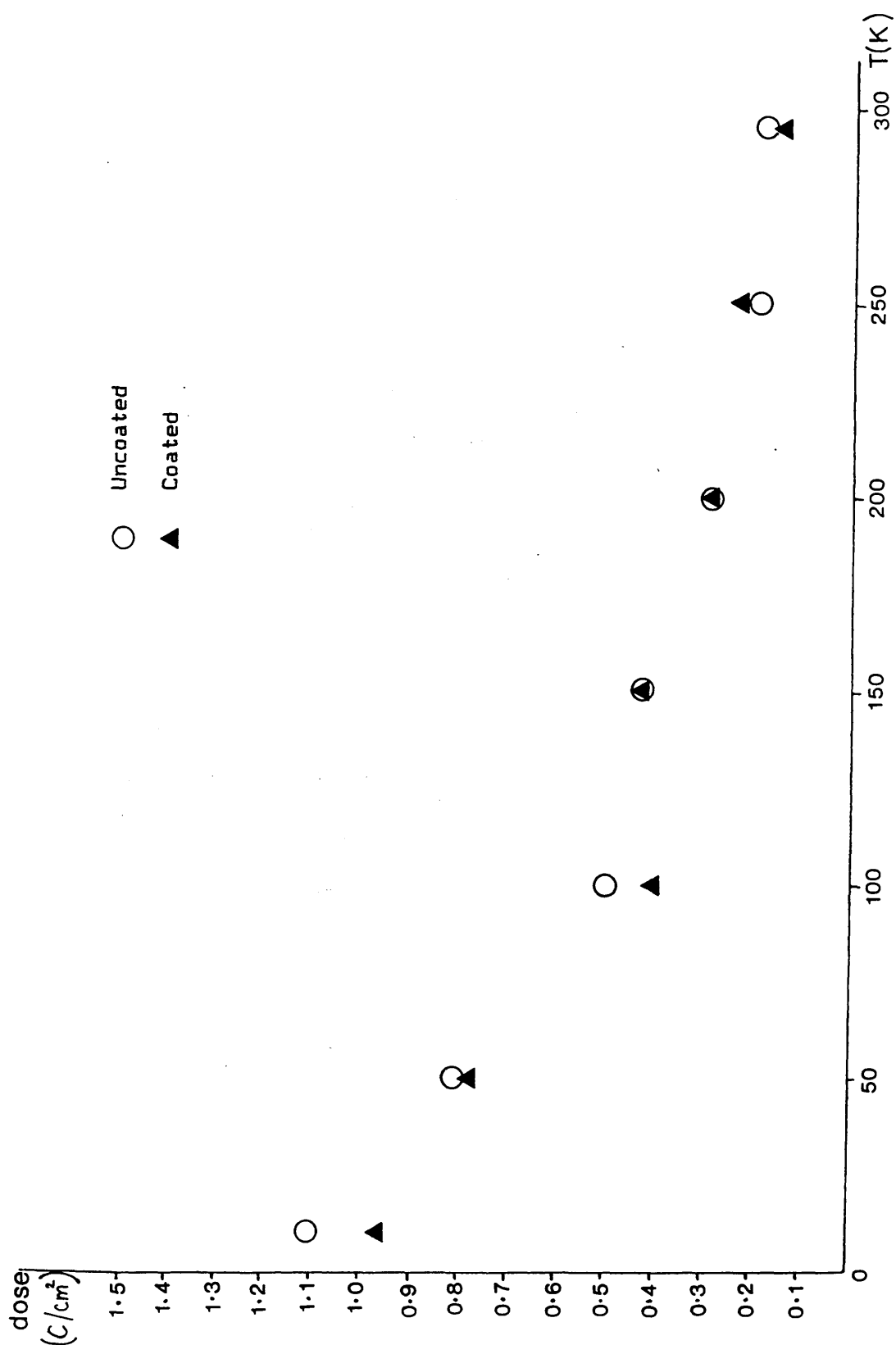


Fig. 5.7(b) Plot of the electron dose against temperature for destruction of the diffraction pattern for coated and uncoated areas of metal-free phthalocyanine (thickness by weight 100\AA , by Δf 60\AA).

Table 5.H.Gain in Lifetime on Lowering Temperature.

	<u>Overall</u>	<u>RT to 150K</u>	<u>150K to 10K</u>
OVALENE	12.0	1.5	8.0
CORONENE	4.5	1.5	3.0
PHthalOCYANINE (1)	3.0	1.7	1.8
PHthalOCYANINE (2)	6.2	2.6	2.4
PHthalOCYANINE *	5.4	2.3	2.4

* calculated from D_e measurements (Section 5.6)

5.6 Calculation of D_e for Metal-free Phthalocyanine.

The fading of phthalocyanine diffraction patterns was observed at seven different temperatures as before, but instead of estimating the dose required to destroy the crystallinity completely, the diffraction patterns were recorded as they faded and the intensities of the first-order diffraction spots were measured with the aid of a Joyce-Loebl flat-bed microdensitometer.

This is an instrument in which the photographic plate is mounted on a sliding glass stage between a light source and a photomultiplier detector. Part of the light beam is directed through the specimen, part through a grey glass "wedge" whose optical density varies linearly along its length. The signal generated by the difference in intensity between the reference beam and the beam passing through the specimen operates a servo-mechanism which slides the calibrated wedge until the two transmitted intensities match. A system of pulleys connects the sliding wedge to a chart table where the variation in intensity of the specimen negative is plotted.

This system is not ideal for use with diffraction patterns due to the sharpness of the variation in intensity at each spot; however if the negative is carefully aligned on the specimen table so that the diffraction spots are centred, and a very narrow slit-width is selected to sample a small area at a time,

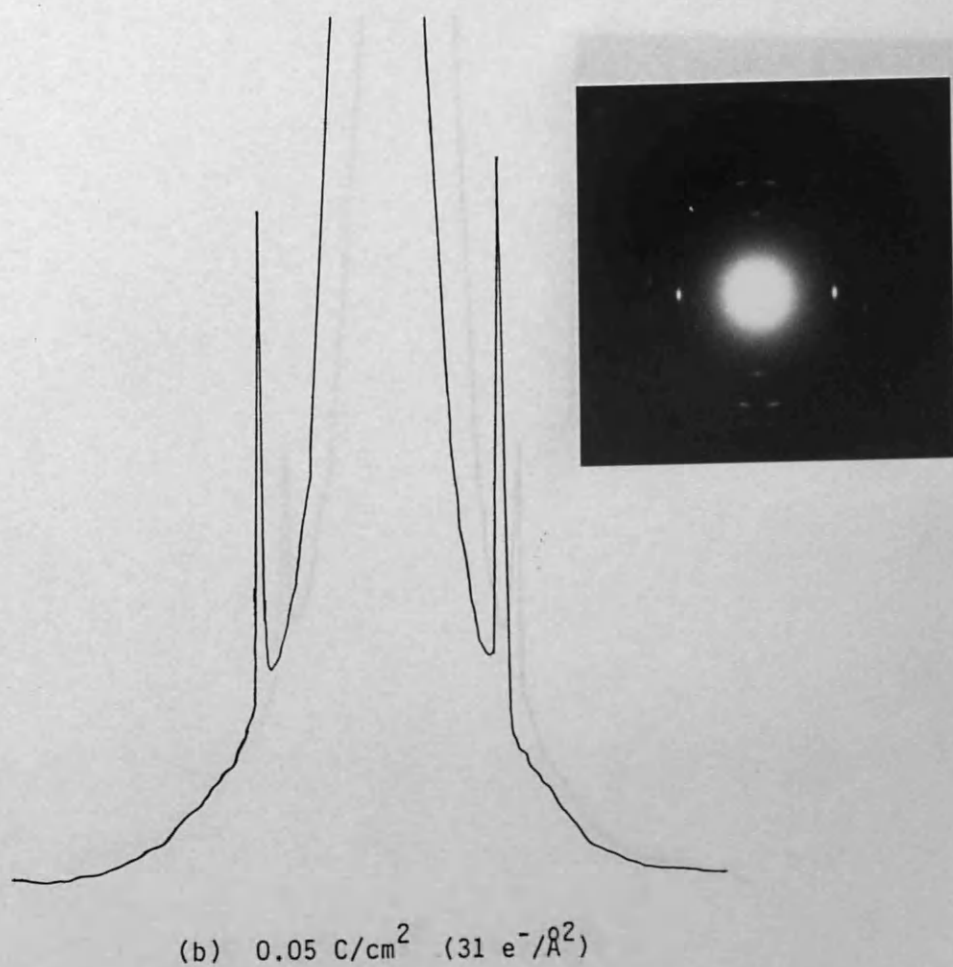
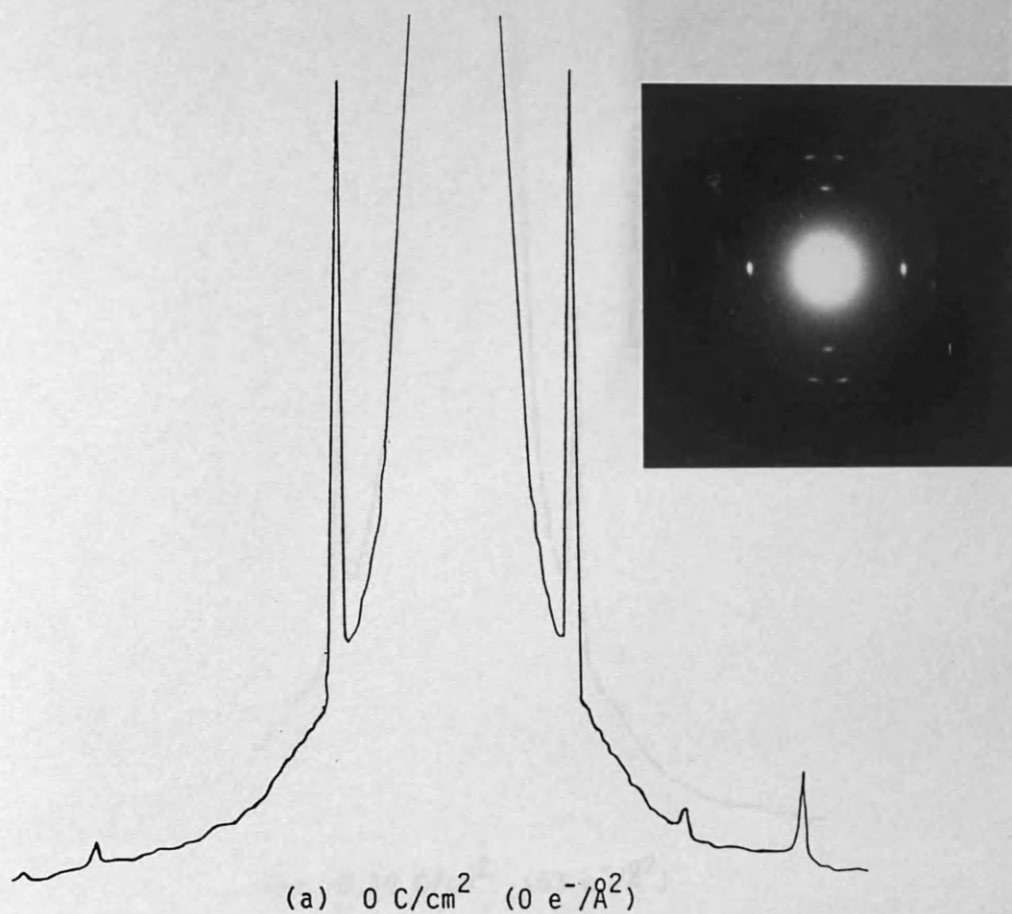
the area under each peak can be considered proportional to the intensity of the spot.

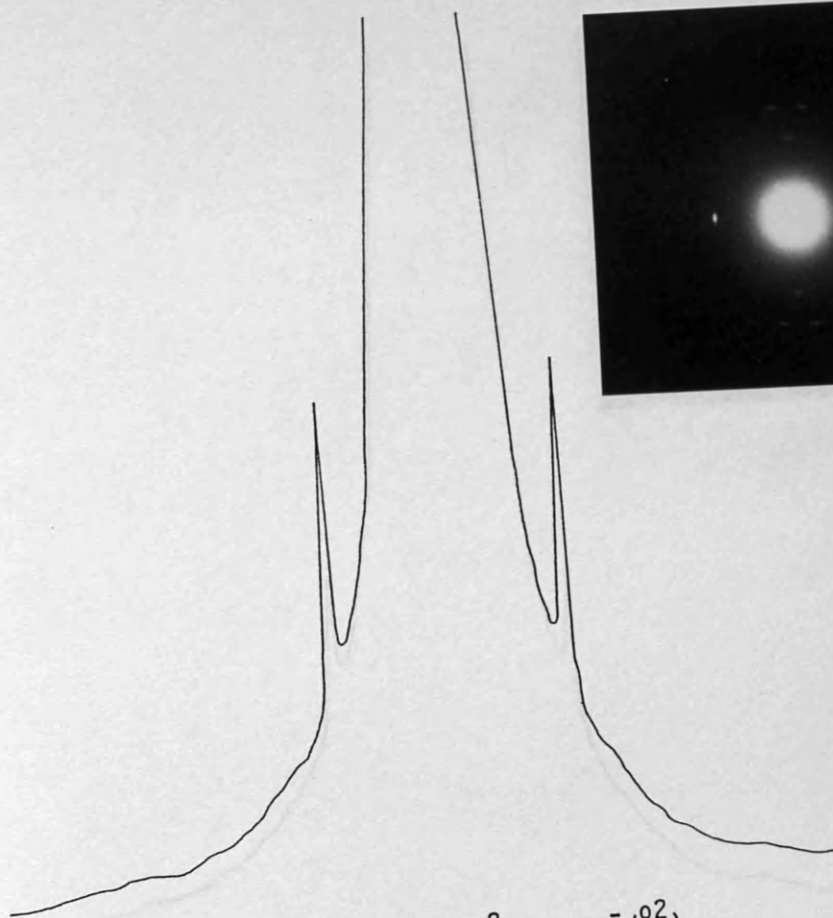
An example of a fading series of diffraction patterns of metal-free phthalocyanine, along with the densitometer traces for its (002) reflections, is shown in Fig 5.8.

Intensity measurements were made for every diffraction pattern in each fading series, and the peak areas were calculated and plotted against the dose for each temperature. Only those traces were used where Friedel symmetry conditions were met - that is, where the (hk0) and (\bar{h} k0) reflections were the same.

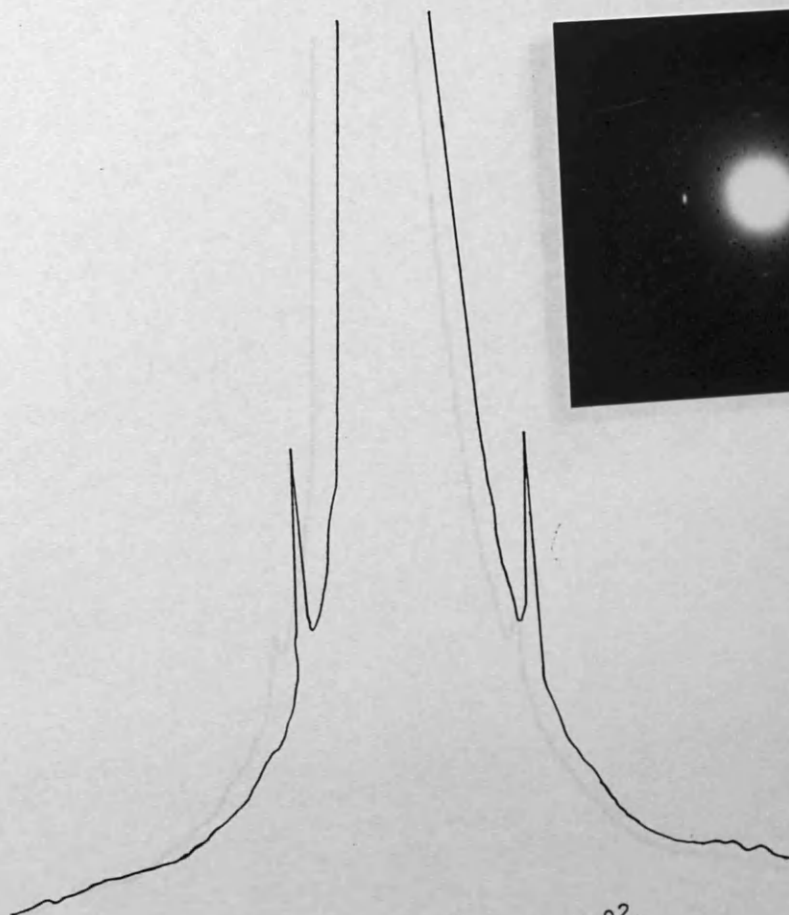
The fading curves are shown for coated and uncoated films in Figs. 5.9 and 5.10. The electron doses required to reduce the intensities of the spots to $1/e$ (that is, to 0.368) of their original values were obtained from the curves and plotted against temperature to give the graph shown in Fig. 5.11.

Fig. 5.8 Microdensitometer traces of (002) reflections of metal-free phthalocyanine with increasing electron dose, at 200K.

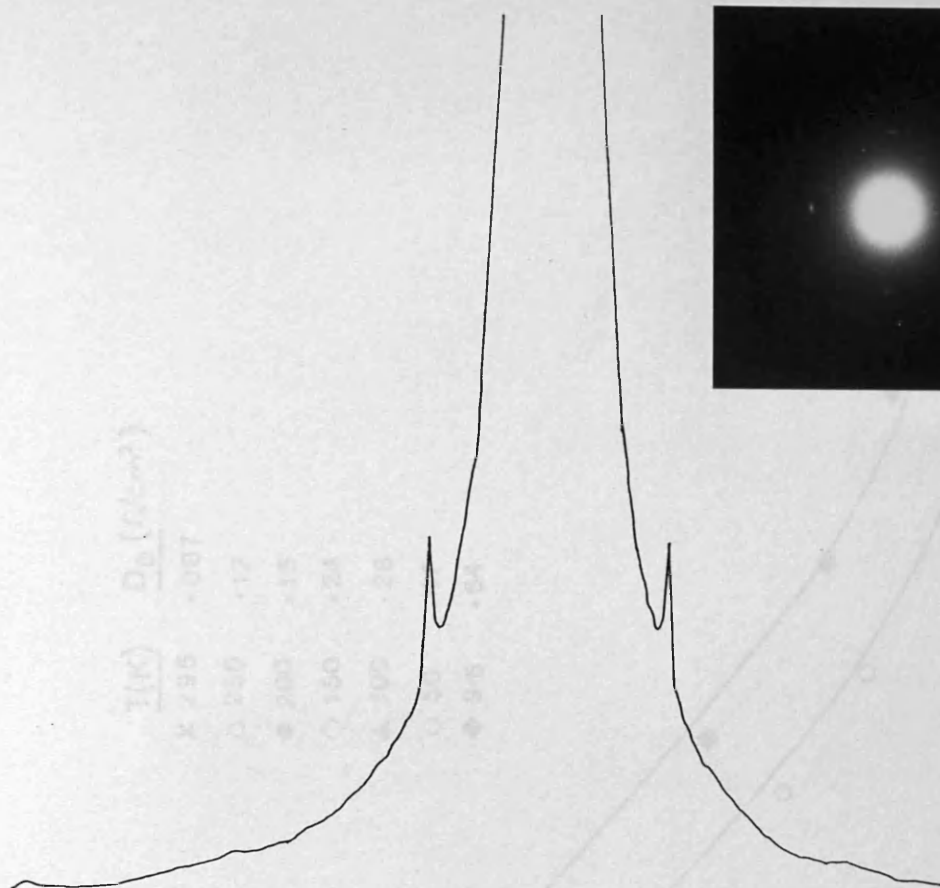




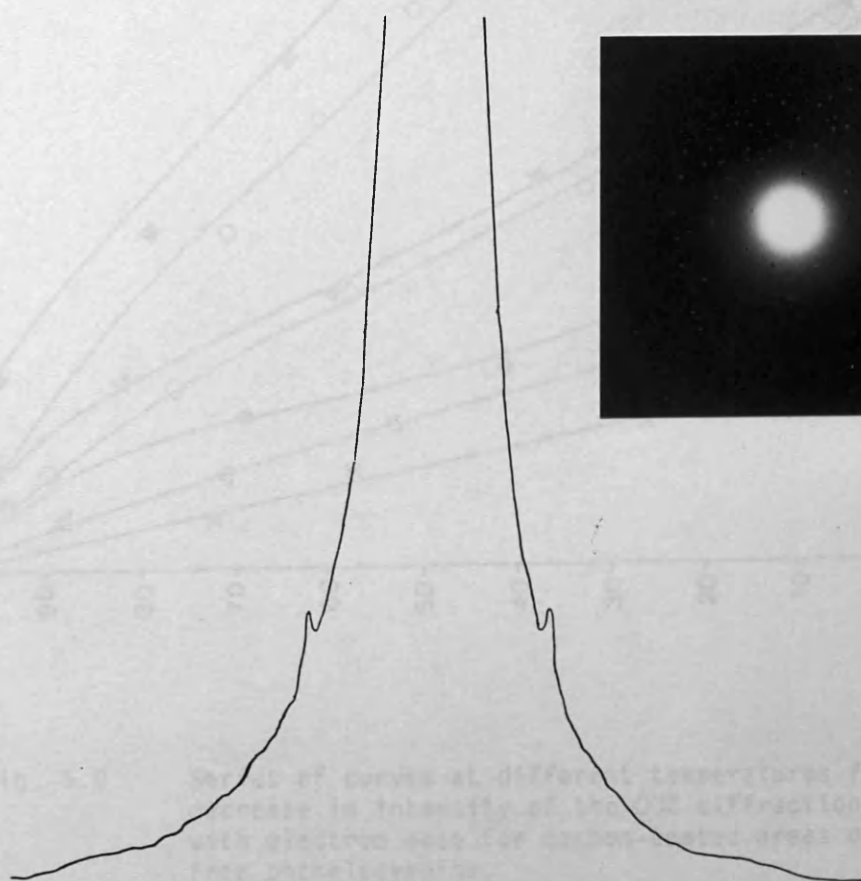
(c) 0.10 C/cm^2 ($63 \text{ e}^-/\text{\AA}^2$)



(d) 0.15 C/cm^2 ($94 \text{ e}^-/\text{\AA}^2$)



(e) 0.20 C/cm^2 ($126 \text{ e}^-/\text{\AA}^2$)



(f) 0.25 C/cm^2 ($157 \text{ e}^-/\text{\AA}^2$)

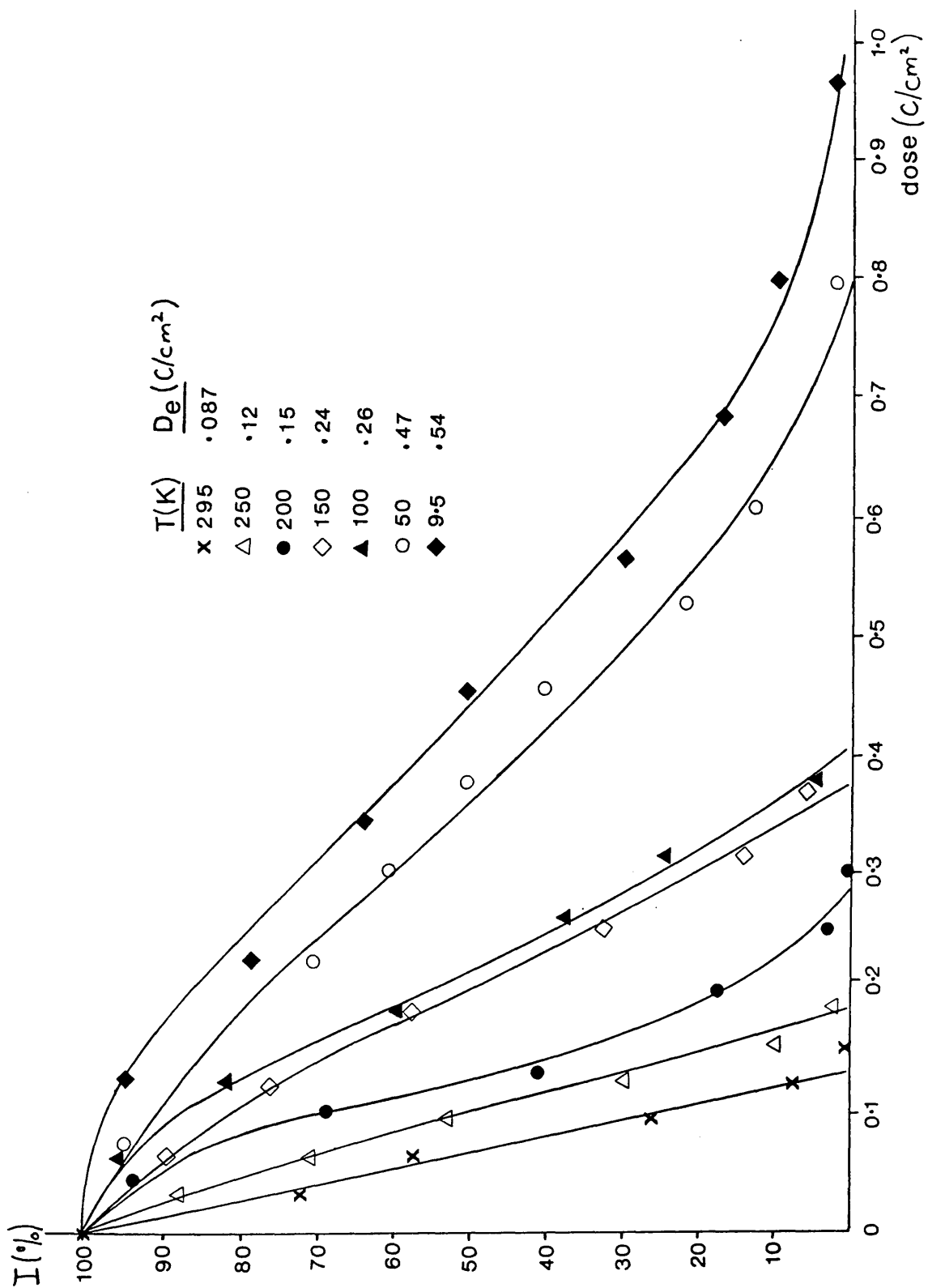


Fig. 5.9

Series of curves at different temperatures for the decrease in intensity of the 002 diffraction spots with electron dose for carbon-coated areas of metal-free phthalocyanine.

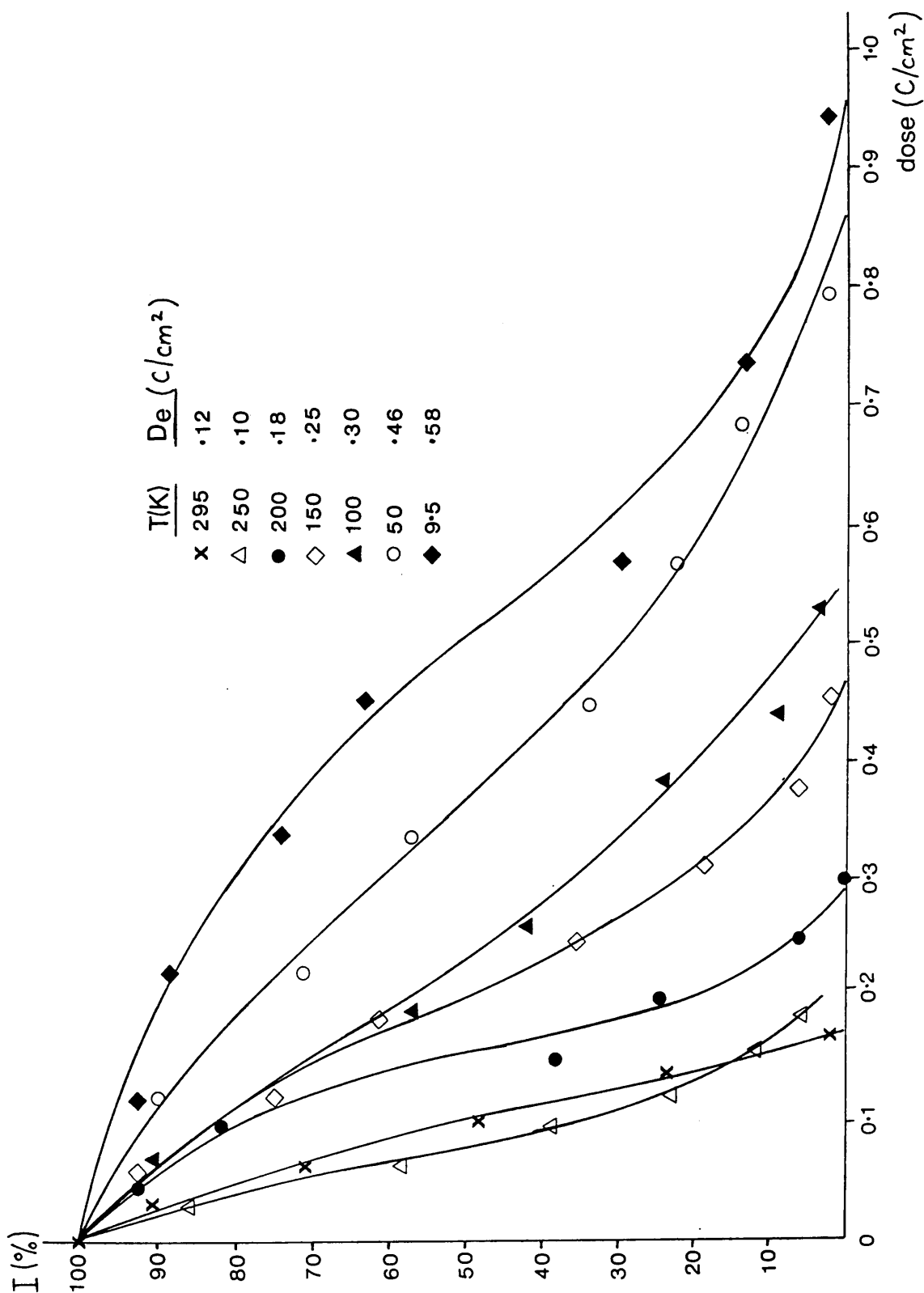


Fig. 5.10

Series of curves at different temperatures for the decrease in intensity of the 002 diffraction spots with electron dose for uncoated areas of metal-free phthalocyanine.

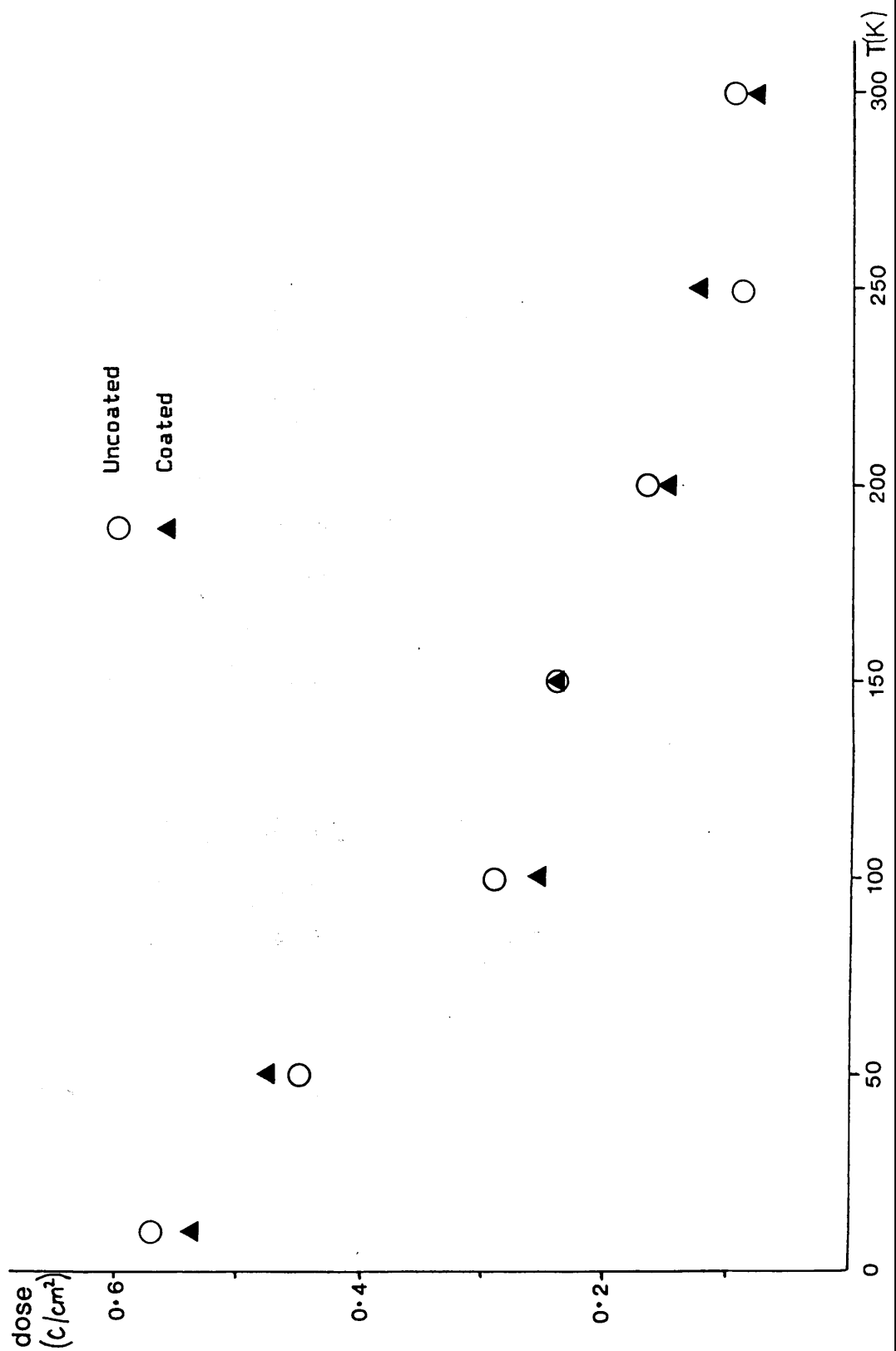


Fig. 5.11 Plot of D_e versus temperature (K) for coated and uncoated areas of metal-free phthalocyanine.

DISCUSSION:

It appears from the curves of Fig. 5.5 to 5.7 that an almost equal increase in specimen lifetime can be obtained by cooling to liquid helium temperature from 100K as by cooling from room temperature to 100K. An International Experimental Study Group (1986) quotes a range of 3 - 5 as being the protection factor obtained on cooling organic crystalline specimens to 150K, but reports a wide variation in results below this temperature. The results in this section (Table 5H) give a range of 1.5 to 2.6 for 150K, with equal or higher factors possible on cooling from 150K to 10K, especially for ovalene, although the reason for this very high protection factor is not known.

The point at which the protection factor for further cooling becomes less than that already obtained appears to have been reached by about 100K for ovalene, coronene and phthalocyanine.

Although the overall gain in lifetime varies widely from specimen to specimen in Table 5H, the proportion of the gain achieved by 150K appears constant for the three phthalocyanine specimens, and differs for the ovalene and coronene. If the temperature at which a certain gain in lifetime is achieved depends on the substance, a possible future experiment would be to relate these; it may be the size of the diffusing fragments which is affecting the temperature at which diffusion is inhibited.

5.7 The Dependence of Radiation Sensitivity on the Number of Layers in a Langmuir-Blodgett Film.

To confirm the dependence of radiation sensitivity upon specimen thickness, end-dose measurements were made as before on three samples of acetyl pyrene prepared by B. Eyres (I.C.I, plc) by the Langmuir Trough method (described by Roberts et al 1981). The layers were deposited separately from a water surface, the efficiency of deposition being monitored by measuring the change in area of the monolayer floating in the trough compared with the area of the substrate on which the layer was picked up.

The three specimens consisted of a monolayer, a four-layer film and a six-layer film. The four- and six-layer films tended to produce diffraction patterns corresponding to disordered layer structures; single crystal areas were sometimes to be found in the "monolayer" specimen but only areas believed to be true monolayers were considered in this experiment. The doses required for the complete destruction of the diffraction pattern in each case are shown in Fig. 5.12. There appears to be a linear dependence of critical dose upon the number of layers present (or specimen thickness), at least for this order of thickness.

This is in agreement with the results of Ohno (1984) who made similar measurements on layers of behenic acid $[\text{CH}_3(\text{CH}_2)_{20}\text{COOH}]$ and found a linear relationship for the thicknesses between 25 and 100\AA . Ohno, however, defined the critical dose in his experiment as D_e , the number of electrons required to reduce the intensity of the diffracted beam to $1/e$ of its original value.

In contrast to the result shown here, the plot given by Ohno consists of a straight line passing through the origin. Extrapolating the line through the points of Fig. 5.12 a value of $2.6 \text{ e}^-/\text{\AA}^2$ is obtained at zero thickness. This may be a consequence of the aromaticity of the acetyl pyrene molecule; a layer of the molecules can withstand a higher radiation dose than would be predicted by the thickness alone. Behenic acid on the other hand is a linear molecule built up of uniform sub-cells (disregarding the CH_3 and COOH end groups); the radiation sensitivity is more likely to be directly related to the number of sub-cells and hence to the length of the molecule.

Fryer and Holland (1983) and Holland, F.M. (PhD Thesis 1984) also found a linear dependence of end-dose on specimen thickness for thin evaporated films of copper phthalocyanine.

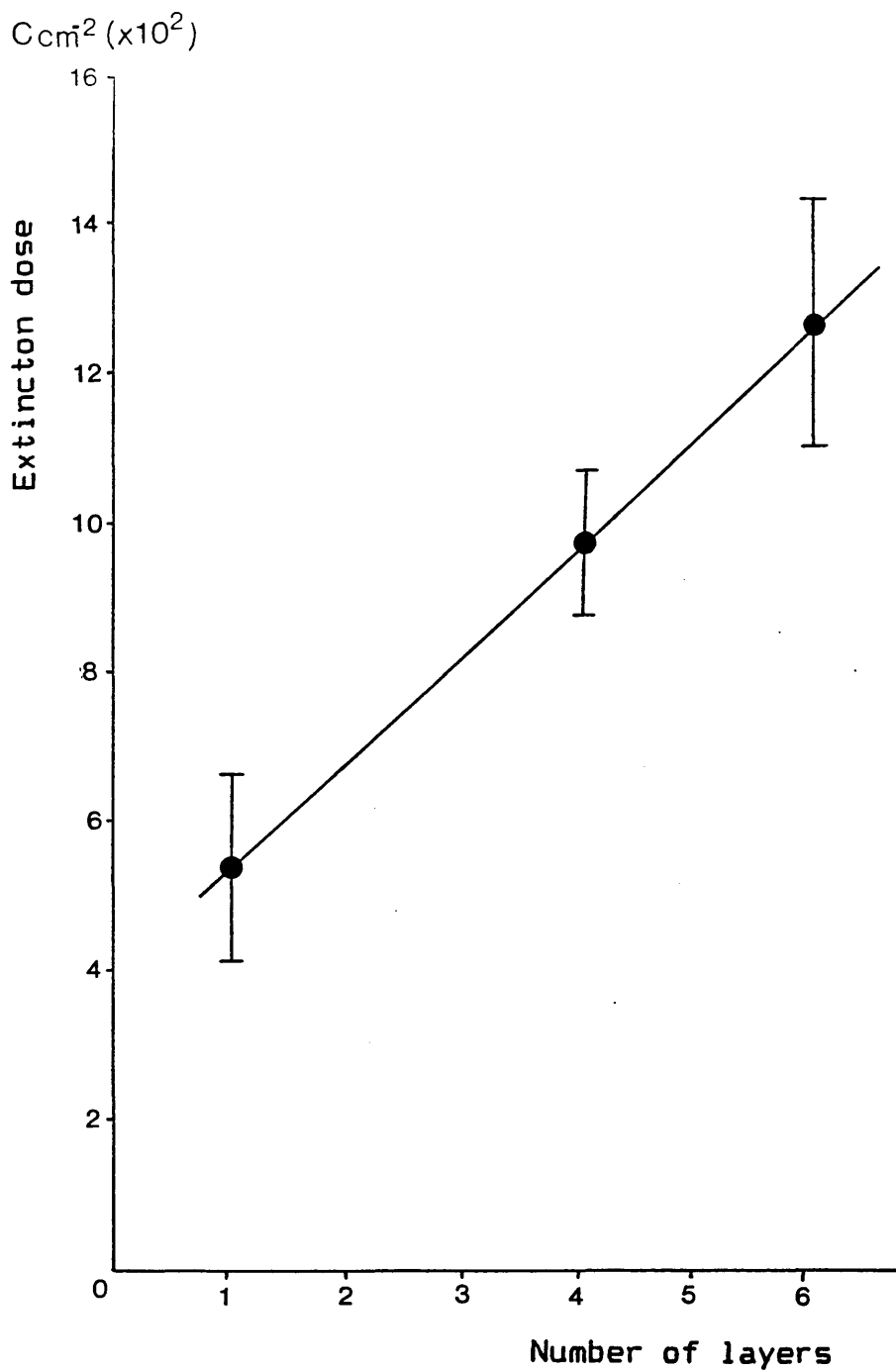


Fig. 5.12 Plot of extinction dose against number of layers for tetra-tertiary-butyl copper phthalocyanine, prepared by the Langmuir-Blodgett method.

CHAPTER 6: THE PARAFFINS - INTRODUCTION.

- 6.1 Growth of Paraffin Crystals.
- 6.2 Packing Behaviour of Paraffins.
- 6.3 Solid Solutions.
- 6.4 Vegard's Law.

CHAPTER 6: THE PARAFFINS - INTRODUCTION.

6.1 Growth of Paraffin Crystals.

"Paraffin" is the common term for an extensive homologous series of saturated, unbranched hydrocarbons with the empirical formula C_nH_{2n+2} . The series ranges from the gaseous molecules at room temperature where $C = 1-4$, through volatile liquids and waxy solids, to very long chains of C_{80} or more, which form white lozenge-shaped crystals. The simple molecular structure of the paraffins has made them a popular model for more complex but related materials, for example fatty acids and lipids [Dorset 1978, 1983 (a + b)] and the higher members of the series may in some respects be considered as polymers of low molecular weight.

The growth mechanism of paraffin crystals was studied by Dawson and Vand (1951), who shadow-cast n-hexatriacontane with palladium and examined the crystals by electron diffraction and electron microscopy. The crystals were grown from solution and lay with their {001} faces on the substrate. They were found to be orthorhombic, with a- and b-axes in close agreement with the X-ray values published by Müller (1932). Micrographs of single crystals indicate a spiral growth mechanism originating at a screw dislocation; complex spirals occur when more than one dislocation is present.

When two dislocations of opposite sense occur close to each other the spirals may cancel each other out and the crystal appears to consist of discrete steps. The steps of the spirals may be one molecule high, or more than one; in the latter case subsidiary dislocations are evident. Dawson and Vand's results supported the theory that crystals may grow only where there is a dislocation, although they did not support previous theories of long-range surface migration of molecules.

Anderson and Dawson (1953) postulated that the height of the growth steps depends on the size of molecular aggregates in solution. The preferred step height for $C_{39}H_{80}$, which is not associated with other molecules in solution, is monomolecular, whereas stearic acid, which forms bimolecular aggregates in solution, crystallises with a bimolecular growth-step.

Further studies were conducted by Keller (1961), again with $C_{36}H_{74}$, by light and electron microscopy. Heating stages were used in both types of microscope, and striations on the crystals were observed along the lozenge diagonals at elevated temperatures which remained when the crystals were cooled again. These were ascribed to shear planes arising from translation of stacks of molecules in the direction of the c-axis of the unit cell.

6.2 Packing Behaviour of Paraffins.

Solid paraffins exist in several polymorphous forms, all of which have the chain axes of the molecules arranged parallel to each other, and the way in which the chains pack depends both on the temperature and on the length of the chains (Kitaigorodskii 1973).

Studies of paraffins by diffraction methods have been carried out since the very early days of these methods, and the existence of polymorphs was observed in 1930(a) by Müller, who recorded two sets of X-ray reflections from a sample of ercosane ($C_{20}H_{42}$) as it cooled from the melt, first to a transparent solid and then to a white opaque one.

Müller demonstrated that the longest spacing of the unit cell showed a constant increase with n , the number of carbon atoms in the chain. The two shorter (a and b) axes remain almost constant for the orthorhombic form, although Müller observed (1930b) some variation occurring between the spacings for long and short chains, which he ascribed to the lateral interaction of the chains.

The ab face of the orthorhombic cell of paraffin is shown in Fig. 6.1. The dimensions of this plane have been measured by Teare (1959) as:

$$a = 7.42\text{\AA} ; b = 4.96\text{\AA}$$

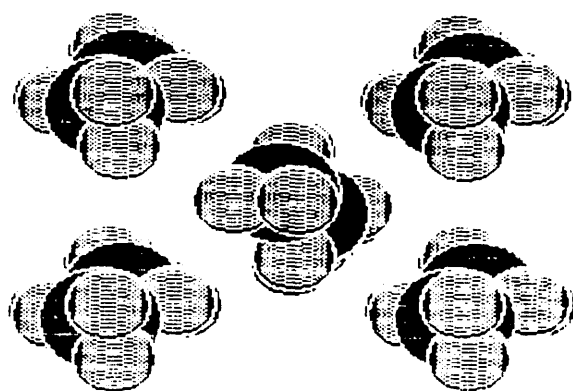
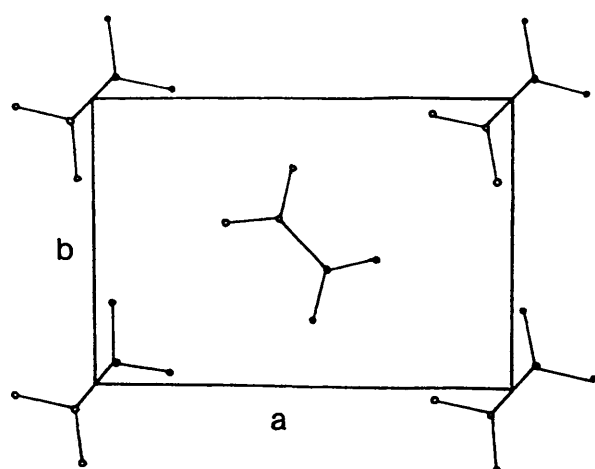


Fig. 6.1 The *ab* face of a paraffin unit cell
 $a = 7.42\text{\AA}$ $b = 4.96\text{\AA}$

These X-ray results are in good agreement with those of an early electron diffraction experiment of Rigamonti (1936) who measured the spacings of orthorhombic $C_{31}H_{64}$, and who also made more detailed measurements of H-C-H bond distances and angles than had previously been available.

In contrast to Müller's results, more recent studies show a variation in the a and b dimensions of less than 1% for differing chain lengths in their orthorhombic form, the form in which the chain axis lies exactly along the c-axis of the unit cell (Nyburg and Potworowski 1973).

The length of the c-axis depends on the number of carbon atoms in the molecule, and there is a slightly different relationship depending on whether the number, n, is odd or even.

$$\text{where } n \text{ is odd, } c = 2.546n + 3.75\text{\AA}$$

$$\text{where } n \text{ is even, } c = 2.540n + 3.693\text{\AA}$$

This is a consequence of a difference in symmetry between cells containing odd and even chains, which will be discussed below.

However, the length of the chain does determine the packing arrangement favoured by the molecules. With n (even) ≤ 26 , a triclinic packing occurs, as described by Müller and Lonsdale (1948) for the case of $C_{18}H_{38}$. An orthorhombic unit cell was observed near the melting point for the material (27°C), or if

impurities of C_{16} or C_{20} paraffins were present, but at room temperature the pure substance formed a triclinic arrangement with:

$$a = 4.28\text{\AA} \quad ; \quad b = 4.82\text{\AA} \quad ; \quad c = 23.07\text{\AA}$$

$$\alpha = 91^{\circ}6' \quad ; \quad \beta = 92^{\circ}4' \quad ; \quad \gamma = 107^{\circ}8'$$

Only one molecule was observed per unit cell, implying that, unlike the orthorhombic arrangement, the planes on which the carbon atoms lie are all parallel.

Fig. 6.2 shows the "inter-layer distance" for a range of paraffins from C_{16} to C_{36} (after Kitaigorodskii 1973). This is the distance between the planes passing through the chain-ends of the molecules. The series A represents the odd-numbered carbon chains which pack in an orthorhombic unit cell; hence the distance is a linear function of the number of carbon atoms in the molecule, and corresponds to the length of the carbon backbone.

The lower even-carbon chains (series B) pack obliquely in triclinic cells; hence the distance between the layers is slightly shorter than that for the orthorhombic form of the same material.

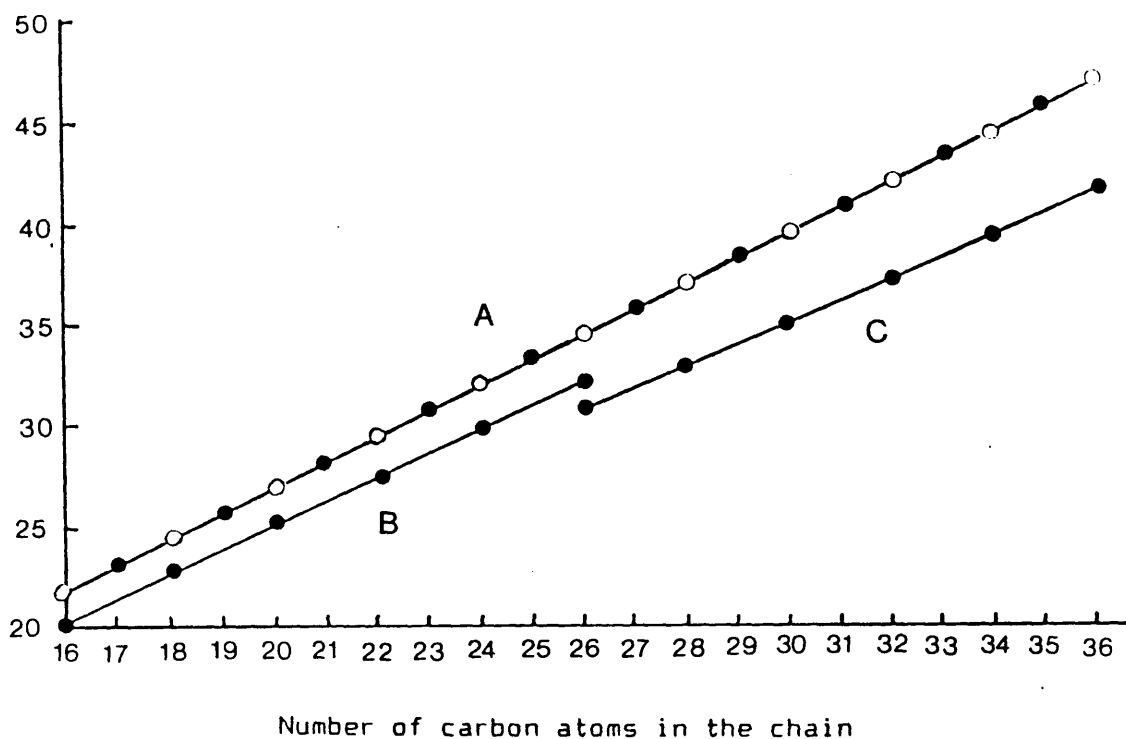


Fig. 6.2 The "inter-layer distance" for pure paraffins (after Kitaigorodskii)

The chains may not lie at any tilt angle, but must assume a value in which the zig-zags of adjacent molecules are displaced by an integral multiple of c_0 . If the chains are displaced in such a way that a CH_3 end-group is in contact with methylene groups of adjacent chains, then the packing density is lowered.

In the monoclinic form of the higher even paraffins ($C \geq 28$, series C of Fig. 6.2), the angle β is 119° , the molecules lie at an even more oblique angle than those of the triclinic paraffins, and the perpendicular separation of the chain-ends falls even further short of the actual length of the molecule.

The dimensions of the monoclinic form of $\text{C}_{36}\text{H}_{74}$ are:

$$a = 5.57\text{\AA} \quad ; \quad b = 7.42\text{\AA} \quad ; \quad c = 48.35\text{\AA}$$

$$\beta = 119^\circ \quad (\text{Kitaigorodskii 1973}).$$

Detailed X-ray structural studies on representative members of each type of paraffin have been carried out by Nyburg and Lüth (1972) ($\text{C}_{18}\text{H}_{38}$ n-even, triclinic); Shearer and Vand (1956) ($\text{C}_{36}\text{H}_{74}$ n-even, monoclinic); Teare (1959) ($\text{C}_{36}\text{H}_{74}$ n-even, orthorhombic); and Smith (1959) ($\text{C}_{23}\text{H}_{48}$ n-odd, orthorhombic).

The chain packing of each of the three types of subcell is shown in Fig. 6.3. In the monoclinic and triclinic modifications the planes containing the C-C bonds of the chains are all parallel; this is not the case with the orthorhombic structure.

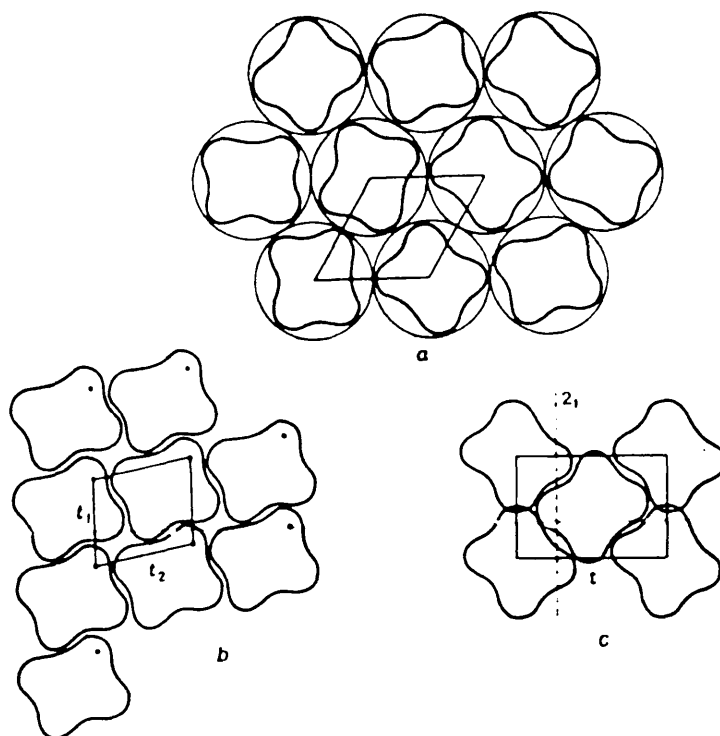


Fig. 6.3 Three possible types of close packing of chain molecules:

- (a) hexagonal,
- (b) oblique,
- (c) rectangular.

(after Kitaigorodskii)

Kitaigorodskii (1973) assumes the tetragonal subcell to be slightly more energetically favourable than the orthorhombic, being slightly denser; this energy difference becomes less important as the molecules increase in length, concerning as it does only the packing of the end-groups. For this reason at $n > 26$, the orthorhombic configuration becomes stable.

Near their melting points, some paraffins undergo a phase transition in which the symmetry of the unit cell changes from orthogonal to hexagonal. This is a consequence of rotational disorder about the axes of the chains leading to a circular average cross-section instead of an orientated one. The chains themselves pack as cylinders and the angle ψ in Fig. 6.4 becomes 60° (Müller 1932).

Three possible models for the disorder experienced by paraffin molecules at the pre-melt phase transition are discussed by Dorset et al (1984a). These are (a) the rigid rotor in which the whole alkyl chain rotates about its axis, (b) a helical configuration as observed in polytetrafluoroethylene, and (c) a kinked chain, with defects either distributed at random or grouped together. It was found that diffraction studies of paraffin molecules in the $hk0$ orientation (that is, the projection looking down the chains) could not distinguish between the three types of disorder as the resultant intensities could be accounted for by any of the three models.

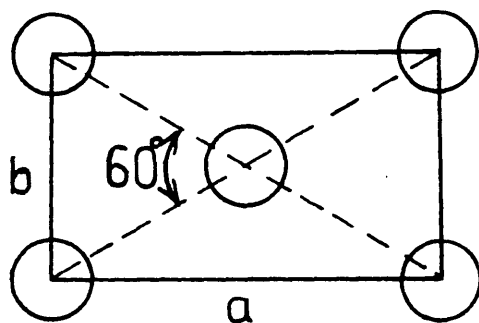
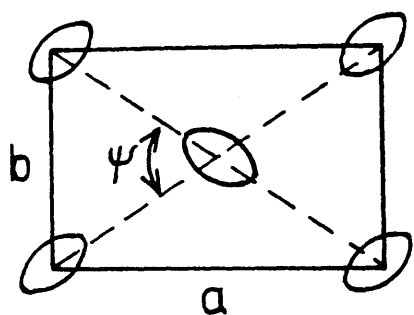


Fig. 6.4 The orthogonal-hexagonal phase transition in a paraffin near its melting point (after Müller).

However, by crystallising n-hexatriacontane ($C_{36}H_{74}$) in the 0kl orientation (a description and references are given in Chapter 4) a distinction could be made and a mechanism postulated. The changes in observed intensity ratios do not support either of the first two conformations, but a model was constructed for the third, kinked structure, from which it was found that the average density of defects at voids at the chain-ends have a modulating effect on the low-angle 001 reflections which agrees with experimental observation.

A hysteresis effect was also observed in which the chains did not immediately return to their defect-free conformation on cooling the crystal; on re-warming, the phase transition occurred at a temperature about 3° lower than when first warmed. The kinked structure was illustrated as shown in Fig. 6.5. Crystals of polyethylene were also observed to undergo an orthorhombic-hexagonal phase transition on heating (Ingram 1970).

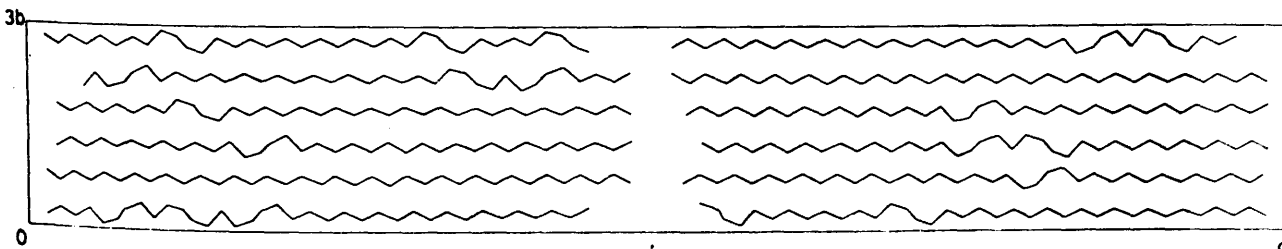


Fig. 6.5 Model of n-hexatriacontane constructed by Dorset to evaluate the average contribution of undistorted and kinked chain segments to total diffraction patterns.

A similar, but irreversible, "quasi-thermal" effect was found for paraffins irradiated in the electron microscope (Dorset et al 1984b Dorset and Zemlin 1985). Thermal effects are attributed to "gauche-trans-gauche⁻¹" kinks occurring in the chains which produce voids in the chain-ends and cause the fading of the 001 reflections. Irradiation on the other hand may cause the formation of trans-vinylene bonds which would have a similar attenuating effect on the diffraction pattern; g-t-g⁻¹ kinks may also be present (Dorset, Holland & Fryer 1984).

The phase behaviour of a large range of n-paraffins, from C₅ to C₃₆ has been studied by Schaerer et al (1956), who found that (a) the phase behaviour of short-chain n-alkanes is monotropic, and changes into an enantiotropic behaviour for compounds with longer chains, and (b) odd and even series differ in that the change of phase behaviour occurs at very different chain lengths. These authors constructed the diagram shown in Fig. 6.6., which shows the stability range of each phase at a series of temperatures, for both odd and even hydrocarbons. For the odd alkanes, the phase change $S_{\beta} \longrightarrow S_{\alpha}$, where S_{β} is the solid phase which is stable at low temperature (tetragonal, monoclinic, or orthorhombic) and S_{α} is the solid hexagonal phase, only occurs below the melting point ($S_{\alpha} \longrightarrow L$) for chains of nine carbon atoms or more, and the range of stability of the hexagonal phase increases as the chain length increases.

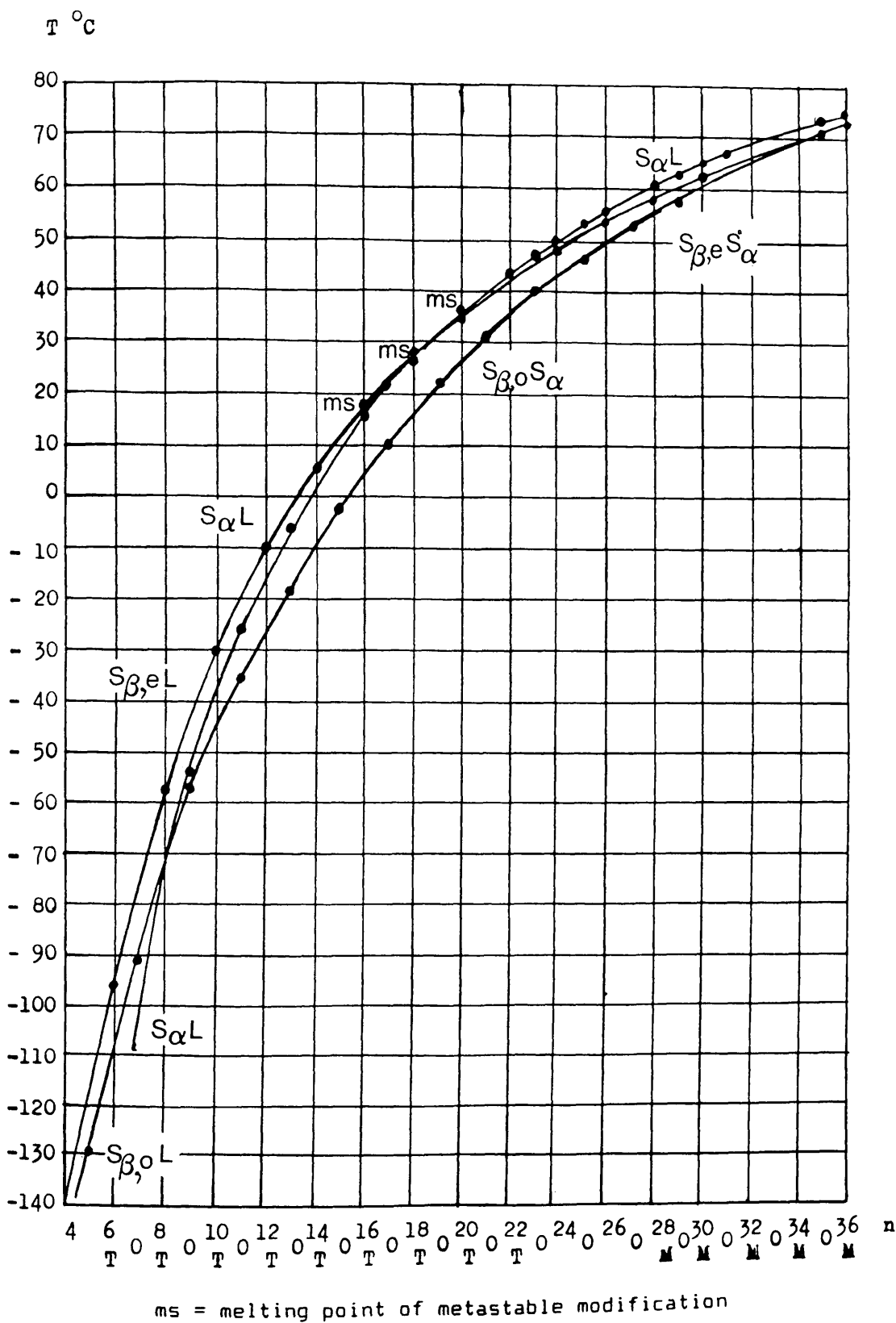


Fig. 6.6 The phase behaviour of n-alkanes.
(after Schaerer et al)

For even-numbered hydrocarbons the shortest chain at which a hexagonal phase is stable is C_{22} , although C_{16} , C_{18} and C_{20} may form a metastable hexagonal phase.

In order to represent the repeating unit within the molecular chains themselves, Vand (1951) introduced the concept of a sub-cell which for normal hydrocarbons has dimensions:

$$a = 7.45\text{\AA} \quad ; \quad b = 4.97\text{\AA} \quad ; \quad c = 2.54\text{\AA}$$

(Nyburg and Potworowski 1973)

where the value of c represents a single "zig-zag" of the methylene chain. Vand demonstrated that the structure factor for the whole cell may be split into contributions from the subcells and from atoms outside the subcells, and that by solving the structure of the comparatively simple subcell unit, the phases of the main unit cell may be deduced.

A diagram of the (010) and (100) projections of an orthorhombic paraffin, with the subcell denoted, is shown in Fig. 6.7 (after Teare 1959).

The essential difference between an odd- and an even-numbered paraffin was illustrated by Müller (1929) in the following diagrams (Figs. 6.8 and 6.9). It is assumed that all the molecules pack in such a way that the linkage between the chain-ends form a centre of symmetry, although this is strictly true only for molecules which pack with the chains

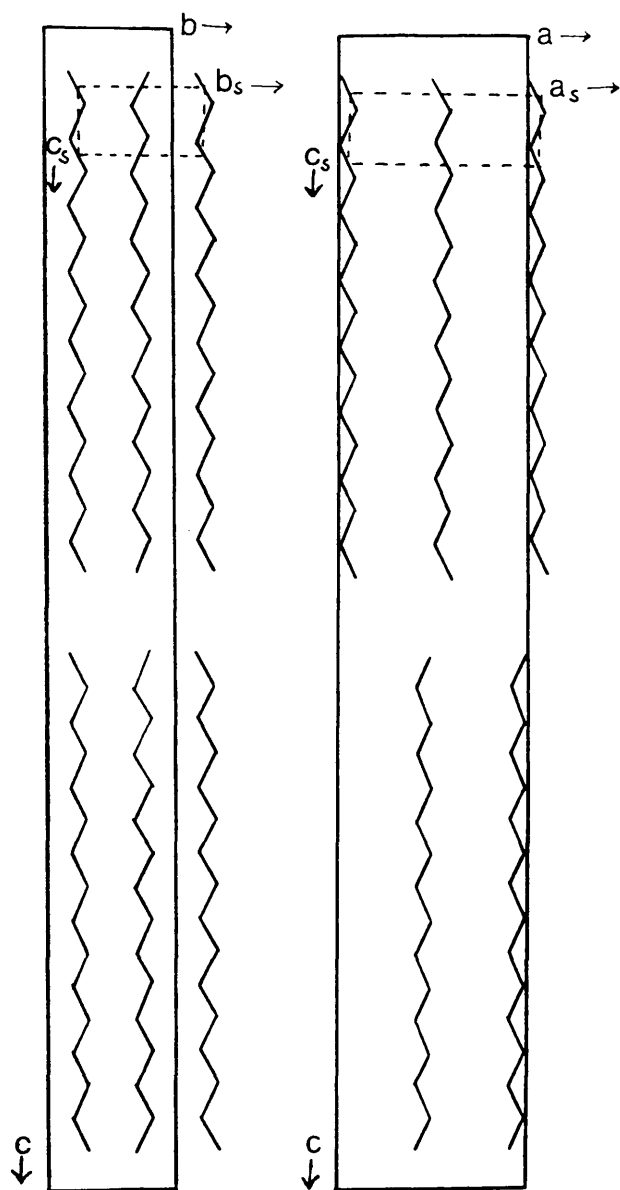


Fig. 6.7 The (100) and (010) projections of orthorhombic paraffins (after Teare (1959)). The "subcell" of the zig-zag is shown by dotted lines.

Fig. 6.8

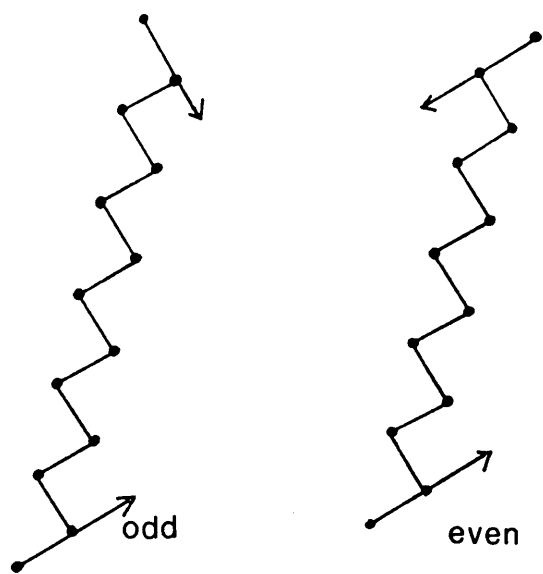
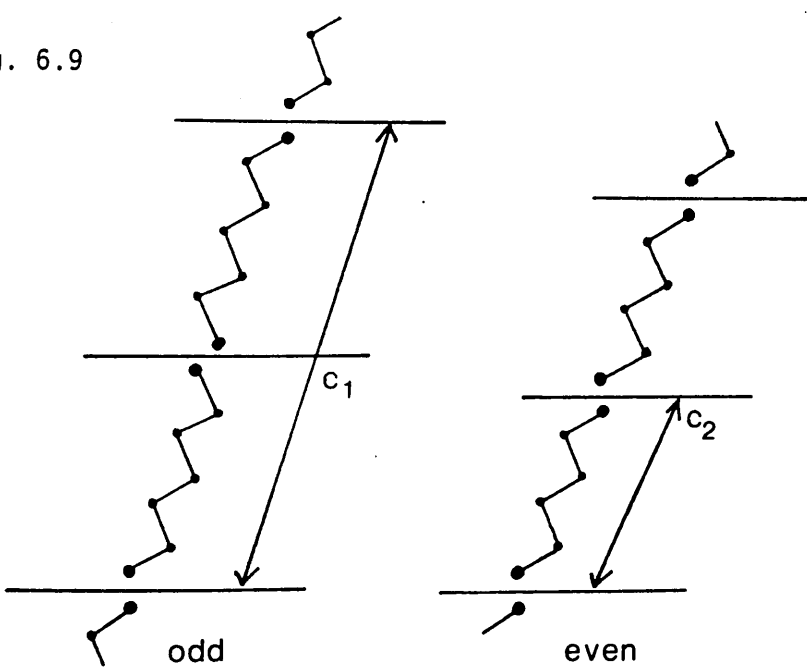


Fig. 6.9



Figs. 6.8 and 6.9 Illustration of the difference in symmetry between an odd and an even numbered paraffin chain.

perpendicular to the plane of the end-groups. It is apparent that for the even-numbered chains, every molecule is related to its neighbour along the c-axis by a simple translation, whereas for the odd-numbered chains the translational relationship holds only for every second molecule. A consequence of this is that the c-axis periodicity corresponds to one molecule's length for even-numbered paraffins but requires two molecules for odd-numbered ones.

Piesczek et al (1974) identified four temperature dependent polymorphs for crystals of $C_{33}H_{68}$. The one occurring at the lowest temperature ($T < 54.5^{\circ}C$) is orthorhombic in shape and consists of unit cells of four molecules each. A molecule in one layer is related to an adjacent molecule in the next layer by a centre of symmetry.

In the higher-energy polymorph occurring at $54.5^{\circ}C$ the packing within each layer remains identical but the stacking of the layers is changed. Two adjacent layers are now related by a twinning plane and the unit cell becomes monoclinic.

At $65.5^{\circ}C$, surface striations are observed on the crystal and a further phase transition takes place. The plane containing the chain-ends is no longer perpendicular to the chain axes, although the subcell remains orthorhombic. The angle formed between this plane and the chains is 18.5° , caused by a

longitudinal shift of each chain by one subcell repeat of 2.54\AA

The fourth modification, where $T > 68^\circ$ is described with less certainty. It may be triclinic or orthorhombic but is not hexagonal although the lattice spacings approach hexagonal symmetry. The four phases were labelled A, B, C and D respectively.

The defect structure and phase behaviour of $n\text{-C}_{33}\text{H}_{68}$ was further studied by X-ray powder diffractometry by Strobl et al (1974), who divided defect types into three categories:

1. Chain rotations, which produce defects in the sub-lattice,
2. Longitudinal shifts of the chains; the sub-lattice remains perfect, and
3. Disruption of the chain zig-zag.

This study was complemented by that of Ewen et al, by infra-red and nuclear magnetic resonance spectrometry (1974). Their results, taken together, show the low-temperature polymorph A to be well ordered with no interfacial or intrachain defects. On warming, the polymorph B is formed by the occurrence of 180° rotational jumps; the lamellar structure remains perfect but the void layer between the lamellae thickens slightly. On changing to C, the layers become oblique as a result of regular staggering of neighbouring planes. Thermal longitudinal

motion enlarges the void layer beyond the normal H-H distance of 2.34\AA , and rotational jumps are more energetically favourable in this configuration than in the rectangular one. The defect structure arising from 180° rotational jumps followed by longitudinal shifts over the distance of one CH_2 repeat in modification 'C' is illustrated in Fig. 6.10. All three classes of defect appear in the "rotator phase" D, in which intrachain defects cause the overall layer spacing to increase, and intramolecular defects diffuse along the chains. The first two forms of motion also become more continuous in character.

6.3 Solid Solutions.

Once the packing behaviour for paraffins over a wide range of chain lengths was established, the next question to interest many authors was that of the packing of solid solutions: how does the presence of a small amount of a homologue of the same or different symmetry affect the ability of the paraffin chains to close-pack, and how much of a difference in chain length is tolerable before the formation of a true solid solution becomes unfavourable?

Kitaigorodskii (1973) stated that organic solid solutions were all of the substitutional type, that is, a solute molecule takes the place of a solvent molecule in the lattice; it was believed that due to the small size of the voids in an organic

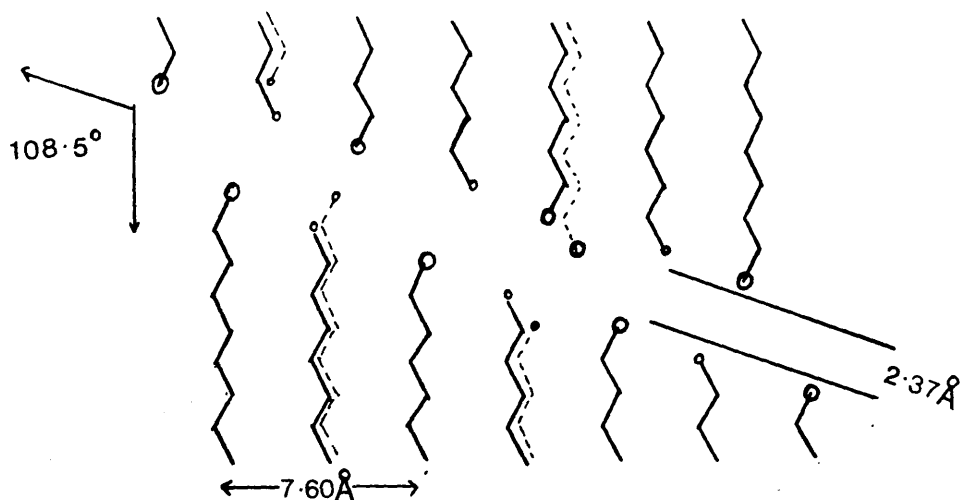


Fig. 6.10 Defect structure in the lamellar interface arising from "flip-flop" screw motions. (after Strobl et al)

crystal compared to the volume occupied by the molecules, interstitial solutions were likely to be very rare if they existed at all. In a later book, the same author (1984) discusses inclusion complexes and clathrates; however, many of these substances do not combine in continuously variable proportions, and so cannot be classified as true solid solutions. For the study of paraffins only true substitutional solid solutions need be considered.

In a review of the subject, Mnyukh (1960) gives two basic conditions for solid solution formation in paraffins: firstly, there should not be a large difference in the chain-lengths of the components, and secondly, only those paraffins which exhibit the same symmetry of subcell packing may form continuous solid solutions. This second condition precludes solid solution formation between even- and odd-chain molecules.

As a third, more general, rule for restricted solubility, Mnyukh also states that "under otherwise similar conditions, n-paraffins with shorter chains will dissolve in n-paraffins with longer chains, while preserving the structure (modification) of the solvent, to a greater extent than in the reverse case".

In 1933, Slagle and Ott examined mixtures of fatty acids by X-ray diffraction methods and found evidence for at least partial solid solution formation for molecules with up to 8 carbon atoms' difference in chain length. In some cases, for example the C_{10}/C_{12} mixture, a two-line pattern was observed, corresponding to a metastable modification; the lines merged after the crystals had been left standing for two weeks.

Solid solutions were also observed of mixtures consisting of several components, all-even, all-odd, and an equimolar mixture of all the fatty acids from C_{10} to C_{18} inclusive.

Where the molecules are of different lengths, it is the structure of the planes on which the chain-ends lie which is of most importance, as it is here that the difference in chain length must be accommodated. It is the behaviour of the chain-ends and chain-folds which characterises the different packing theories for linear polymers, and paraffin solid solutions are often studied as models for polymer systems (Dorset 1985, Asbach et al 1979, Keller 1960).

Asbach et al (1979) constructed two possible models for the arrangement of the differing chain lengths in solid solutions. In one, the chains are arranged in such a way that one end of each short molecule may pack level with the ends of the longer chains, leaving a void at the other, or both ends of the short

chain may fall short of the longer chain-ends. Translations of the short molecule parallel to the longer ones are permissible. In the second model, which the authors consider to be more likely when the shorter component is predominant, the longer chains may take on a "gauche" conformation at their ends, causing kinks which partially occupy the voids and allow a dense packing between the crystal lamellae.

Solid solutions of $C_{24}H_{50}$ / $C_{28}H_{58}$ were observed to fractionate at room temperature, but comparison between reflection intensities from the lamellae and from the subcells for $C_{28}H_{58}/C_{32}H_{66}$ led to the conclusion that the two components are randomly distributed in the lamellae and that voids at the chain-ends are compensated by translations of the shorter chains. Only even-even mixtures were considered.

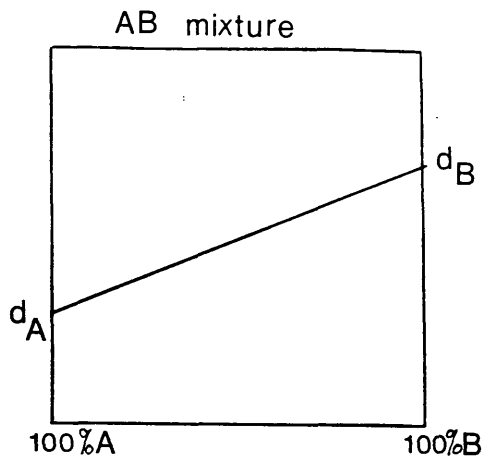
X-ray powder methods cannot identify defects in the interior of the chains, where the molecules depart from the postulated all-trans conformation. Dorset (1985) used electron diffraction techniques to investigate the crystal structures of even-even and odd-even paraffin mixtures in the $Ok1$ orientation. The paraffins studied were $C_{32}H_{66}$, $C_{33}H_{68}$ and $C_{36}H_{74}$, all of which were found to crystallise into the orthorhombic polymorph. Long spacings of solid solutions of C_{32}/C_{36} and C_{33}/C_{36} of various compositions were measured, and plotted against the mole-percentage of $C_{36}H_{74}$ present. Most of the values lay

above the straight line joining the values for the two components. This was the case both for the odd-even and the even-even systems. The presence of kink defects was identified but it was not possible to compare the defect concentration of solid solutions with single-paraffin crystals. It was also shown that longitudinal translations of the shorter chains occur only within the length of the longer chains.

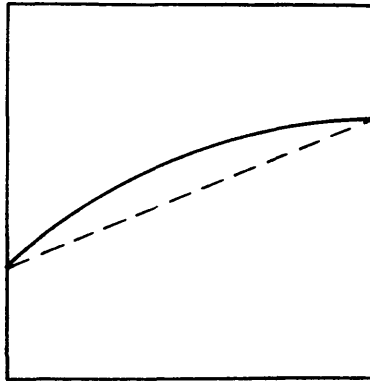
Dorset concluded that although symmetry considerations preclude solid solution formation between odd and even paraffins in their lowest energy forms, mixing is permissible if a higher-energy polymorph of the odd-chain paraffin is adopted, in this case the 'B' form described by Piesczek et al for $C_{33}H_{68}$.

6.4 Vegard's Law.

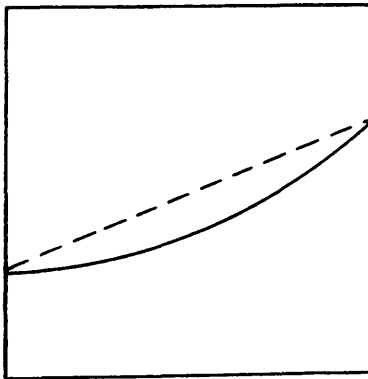
The variation in lattice spacing with composition of series of solid solutions was first examined by L. Vegard (Vegard & Dale 1928), who made his measurements on mixtures of metals such as copper and cobalt, and copper and gold, and on mixed nitrates such as $Pb(NO_3)_2$ / $Ba(NO_3)_2$. His results show a tendency of the lattice spacings to expand in a linear fashion between the values for the two pure components, and such behaviour has come to be known as Vegard's law. Some systems may deviate from this pattern, and the forms that these variations may take are illustrated in Fig. 6.11. Vegard & Dale noted a slight positive deviation in the Cu/Au system but offered no explanation for it.



(a) Expansion of a cell dimension with change in composition according to Vegard's law



(b) Positive deviation from Vegard's law



(c) Negative deviation from Vegard's law.

Fig. 6.11

Attractive or repulsive forces between the components of the solutions, and inhomogeneity of the solid formed on cooling the melt may be the causes of deviations from linear expansion of solutions of metal oxides (West 1984).

The behaviour of paraffin solid solutions with regard to Vegard's law has been investigated by Retief et al (1985), by X-ray powder diffractometry and by Dorset (1985, 1987) by electron diffraction. Retief et al measured a steady increase in the c-axis of a C_{23}/C_{25} system as the proportion of the longer molecule rose, flattening off at about 80%; it appears that a small proportion of a shorter chain has little effect in a predominantly long-chain crystal whereas the presence of a longer molecule causes the c-axis to expand. An increase in both a and b was also recorded, the effect being more rapid when a long molecule was added to a predominantly short-chain paraffin, and this was attributed to protrusions or kinks in the molecules near the chain-ends.

Dorset found that for the systems C_{32}/C_{36} , for each ratio of components, the value of the C/2 spacing lay above the level represented by Vegard's law and that a step function could be superimposed on the values. This was attributed to changes in the packing of the molecules as the composition of the solution changes; at some compositions more than one crystal structure was found to be assumed by the crystal aggregate.

CHAPTER 7 - THE PARAFFINS: RESULTS and DISCUSSION.

- 7.1 Low Magnification Images of Paraffins in the $hk0$ Orientation.
- 7.2 High Resolution Electron Microscopy. of Paraffins in the $hk0$ Orientation.
- 7.3 Image Processing of Paraffins ($hk0$ Orientation).
- 7.4 Fourier Reconstructions of Paraffins in the $0kl$ Orientation.
- 7.5 High Resolution Imaging of Paraffins in the $0kl$ Orientation.
- 7.6 Changes in Lattice Spacings of Solid Solutions of Paraffins.

CHAPTER 7: THE PARAFFINS: RESULTS and DISCUSSION.

7.1 Low Magnification Images of Paraffins in the $hk0$ Orientation.

Plates 4 to 6 show micrographs taken at a magnification of less than 10,000X of $C_{44}H_{90}$, $C_{60}H_{122}$ and $C_{82}H_{166}$ paraffins crystallised from solution. In general these are flat monolamellar lozenges with angles of 67° and 113° , although some show variations in contrast across sections and some show evidence of bend contours or growth steps. Only C_{82} occasionally exhibits the striations in the $\langle 130 \rangle$ direction as reported by Dorset (1985) and as shown in Plate 6. The reason for the appearance of these striations has not been explained in the literature, although Dorset has compared them to the $\langle \bar{1}30 \rangle$ lines found on collapsed polythene lozenges (Bassett et al 1963). It was hoped that image processing techniques applied to low-dose lattice images of the $hk0$ projection of C_{82} crystals in Section 7.3 of this thesis might supply an explanation for the phenomenon, but the results in this chapter shed no further light on the matter.

As demonstrated in Plate 7, the bend contours on the crystal change, loss of contrast occurs and eventually surface detail fades on exposure to the electron beam. In order to find out whether, in the images exhibiting $\langle 130 \rangle$ striations, detail had already been destroyed by the time room-temperature

images had been taken, micrographs of $C_{82}H_{166}$ were recorded in the JEOL 100B at 181K and then at room temperature after cooling. The same details were visible on the face of the crystal at each temperature, and no change was observed in the electron diffraction pattern (Plate 8).

7.2 - High Resolution Electron Microscopy of Paraffins in the hk0 Orientation.

At room temperature, the electron dose required to obliterate the diffraction pattern of a paraffin crystal in the hk0 orientation was of the order of 0.02 C/cm^2 ($12e^-/\text{\AA}^2$). According to the Rose equation, this number of electrons will resolve a 28\AA point separation at best. Lattice resolution will be higher for a given electron dose; however, in reading this figure, a 100% electron utilisation has been assumed and a contrast value of 5%. The dimensions of the unit cell in the hk0 projection of an n-paraffin crystal are $7.45\text{\AA} \times 4.97\text{\AA}$, well below the theoretical resolution limit.

Two possible ways of improving the attainable resolution are:

1. Decrease the acceptable signal to noise ratio by employing image processing techniques ($S/N = 1$ gives a minimum resolvable spacing of 5.8\AA), and
2. Lower the specimen temperature to increase the number of incident electrons which can be tolerated by the structure.

A number of paraffin crystals were prepared from hexane solution and examined in the helium cooled specimen chamber of a cryo electron microscope at about 15⁰K. The minimum dose technique was employed as described in Section (3.2). The paraffins were C₃₆H₇₄, C₄₄H₉₀, C₆₀H₁₂₂ and C₈₂H₁₆₆. These were irradiated at a dose rate of 1e⁻/Å² per second, and for each exposure the total incident dose was 12e⁻/Å². Dorset and Zemlin (1985) have demonstrated that at this value the relative intensities of the beams contributing to the image are still constant enough to give a valid structure within the resolution limit at the 020 reflections.

The signal to noise ratio was such that no contrast was visible to the eye; however, the resolved periodicity was detected by optical diffractometry and the patterns obtained are shown in Plates 9 and 10. The highest frequency resolved is 2.48Å⁻¹ as shown by the appearance of the (020) reflections; although this level of resolution was rare for paraffins and was not detected by subsequent microdensitometry of the plate, in principle it should be possible to form reconstructed images with 2.48Å detail from the noisy image.

Optical diffractometry also provided a method of detecting local changes in orientation or bends in the crystal. Series of optical diffraction patterns taken a known distance apart across low dose micrographs of monolamellar paraffin crystals

showed that for pure paraffins and for solid solutions, the orientation showed no measurable change in the xy plane over a distance of one micron. However, bends in the z direction can be detected by changes in the intensity of the diffraction spots.

Plate 11 shows a series of eight optical diffractograms of a micrograph of a solid solution of C_{33}/C_{36} , mole ratio 2 : 3. The magnification of the negative was 60,000x and the diameter of the illumination spot 12 mm, which corresponds to a diameter of $2,000\text{\AA}$ and a sample of 8.4×10^4 unit cells. The patterns represent eight adjacent areas with centres $1,600\text{\AA}$ apart, so the areas overlap. The 200 spots are most intense at Plates c and f but these planes appear to bend out of the diffracting angle in Plates a, b and h.

This observation is comparable to that of Downing and Glaeser (1986) who found variations in optical diffraction intensity for paraffins when a series of $2,000\text{\AA}$ diameter areas was illuminated. They reported that when a much smaller beam-diameter was used during microscopy, the six diffraction spots stayed constant over several areas of crystal image, and interpret this as supporting Henderson and Glaeser's theory (1985) that beam-induced movement is an important factor in the loss of contrast of beam-sensitive specimens in the electron microscope.

These bends in the crystal are not apparent in the filtered images described in the next section, but the areas sampled for image processing were much smaller than the comparatively coarse sampling of these optical diffractograms.

7.3 - Image Processing of Paraffins (hk0 Orientation).

This was carried out as discussed in Section 3.4, and the micrographs chosen were those showing the highest resolution detail from the optical diffraction results. In Berlin, the window-size used had a radius of 3 picture elements ("pixels"); this was considered large enough to include the whole diffraction spot without including too much background noise. Some of the resulting Fourier reconstructions are shown in Plates 12 to 15. These are of the pure paraffins $nC_{36}H_{74}$, $nC_{60}H_{122}$ and $nC_{82}H_{166}$, and the original images were taken at low contrast and low temperature on the superconducting helium-cooled microscope, at a magnification of 60,000. Two solid solutions, crystallised in the same manner, were also included for comparison; $C_{32}H_{66}/C_{36}H_{74}$ (60% C_{36}) and $C_{33}H_{68}/C_{36}H_{74}$ (60% C_{36}).

It appeared from these reconstructions that a certain domain structure, giving a contrast change every few lattices and forming lozenge-shaped areas, existed in the crystal. A feature resembling a defect is highlighted in Plate 12.

Zemlin et al (1985) reconstructed an image of $C_{44}H_{90}$ by cross-correlation averaging and by Fourier filtering and found an edge dislocation in the reconstructed image.

Fourier filtered reconstructions of atomic resolution images of TaS_2 and MgO have been published by Tomita et al (1985). The reconstructed images show a remarkably similar structure to those of the paraffins and the authors attribute the variation in contrast to the modulation of the semiconductor structure by charge-density waves. The purely organic paraffins however, are not semiconductors and so another explanation had to be found for the contrast-changes. Now, in a recent paper, Pradère et al (1988) have demonstrated that noise being filtered through a large window in the reconstruction procedure may give rise to a "defect" structure which is not related to the original crystal structure.

A new reconstruction was performed on the same micrographs as described above by means of an Optronics densitometer with a 25μ raster by Dr. Douglas Dorset at the Medical Foundation of Buffalo. The resultant images (Plates 16 and 17) show clearly that as the window-size of the masking function is reduced from five to one picture element, the contrast changes become less marked and a perfect lattice emerges. When the mask size is one picture element, much detail is lost due to the averaging over the whole image. However, changes in contrast, if they

existed in the original micrograph, should still appear in the reconstruction as the phase information is preserved in this type of reconstruction. If there had been bends in the crystal, the intensity of the six peaks of the transform, which is the first stage of reconstruction, would differ and the bend contours would appear on the filtered image. These however do not appear, and the structures seen on the coarser reconstructions can be attributed to an artefact of the image processing technique.

7.4 - Fourier Reconstructions of Paraffins in the 0k1 Orientation.

The same image processing procedure as was used for the solution grown paraffins was applied to the epitaxially formed ones. In this case the lattice structure was visible on the original micrographs, which are described further in Section 7.5; the defect density is more apparent from the reconstructed images. Areas of micrographs which showed high order diffraction spots were chosen for densitometry, and windows were formed at the peaks of the Fourier transform as before.

Images were reconstructed of the pure paraffins $C_{32}H_{66}$, $C_{33}H_{68}$ and $C_{36}H_{74}$, and of the solid solutions C_{32}/C_{36} and C_{33}/C_{36} in the mole ratios 1 : 9, 1 : 3, 1 : 1, 3 : 1 and 9 : 1. Defects in the crystal structure are seen to be more numerous in this

orientation than in the $hk0$; the effects of voids or kinks at the chain-ends are more apparent when the c -axis is on view than on looking down the chains of a monolamellar crystal.

A much larger number of areas would have to be digitised and the number of defects counted before a quantitative, statistical account could be given of the defect density for each solid solution at each mole ratio, but a qualitative inspection of the reconstructed images indicates that pure paraffins have very few defects, perhaps one pair in 30 lattices. The 1 : 1 mixture of C_{32} and C_{36} also appears to be almost free of defects. Other ratios of components vary widely; slight variations in crystallisation conditions probably have a large effect on the degree of perfection of the crystal, and the exact rate of cooling of the crystals during the epitaxial growth process is difficult to control. It might be expected that defects would be concentrated where a small proportion of a long paraffin was present in a mixture with a predominantly shorter one, but this does not necessarily appear to be the case. The number of defects in an area of $2.5 \times 10^6 \text{ \AA}^2$ (30 lattices across) ranges from 0 to 20 in four samples of C_{33}/C_{36} with a mole ratio 9 : 1. A $7.44 \times 10^6 \text{ \AA}^2$ area of a 3 : 1 mixture of C_{33}/C_{36} contains no defect at all.

Three examples of reconstructed $0k1$ images are shown in Plate 18:

- (a) is of pure $C_{36}H_{74}$,
- (b) is a C_{32}/C_{36} (3 : 1) solid solution, and
- (c) is a C_{32}/C_{36} (1 : 1) solid solution.

The other reconstructions in the two series have a similar appearance, and no particular pattern emerged from the variation in composition of the solid solutions.

Two pairs of dislocations are marked with arrows. The nature of these dislocations cannot be determined from two-dimensional projections, but it can be seen that where one dislocation occurs, another occurs in the opposite sense to reduce the strain on the lattice. From inspection of the dislocations in 20 reconstructed images, it is observed that the pairs of defects occur at a mean distance apart of 4.3 lattices, with 10 lattices being the widest observed gap.

One problem is the appearance of contrast variation in the reconstructed images. In the previous section it was shown that contrast changes may be an artefact of the Fourier reconstruction, arising from the window-size used in filtering. If this is the case in these $0k1$ images, then the defects occurring in them may also be an artefact, as these are always situated in areas of poor contrast, as demonstrated in Plate 18 but observed throughout the series.

7.5 - High Resolution Imaging of Paraffins in the 0k1 Orientation.

These specimens were prepared as discussed in Section 4.4, and micrographs were taken at room temperature on the JEOL 100B and 100C, and cooled by liquid nitrogen in the "Deeko 250" (operated at 100kV). Micrographs of the pure paraffins are shown in Plates 19 to 23, at an initial magnification of 17,000X. In general, these crystals are long and lath-shaped. They do not crystallise in a monolayer like the hk0 orientated crystals, because of the stronger van der Waals forces along the length of the chain, so thick areas can be seen by their darker contrast.

Lattices corresponding to the $c/2$ axis of the unit cell can be seen clearly; their spacings, which are determined by the chain length of the paraffin molecules, vary with the specimen, and were confirmed by measuring their light optical diffraction patterns. It was quite feasible to record images at room temperature because the required magnification is comparatively low. Plate 21 however, was taken on the "Deeko 250" microscope at 190K and shows a single crystal of $nC_{36}H_{74}$. The optical transform indicates a resolution of 22\AA (the lattice resolution of this microscope is approximately 20\AA). The electron diffraction pattern of a $C_{36}H_{74}$ crystal is also shown (Plate 20b). It is typical of paraffin crystals in this orientation. The row of 001 spots represents the interlamellar

spacing while the wider-angle reflections arise from the "subcell".

Attempts to image at high magnification the second, perpendicular, lattice of 5\AA corresponding to the b-axis of the unit cell were not successful. One reason for this is that the intensity of the illumination required would be too high. A second is that the phase contrast transfer function, calculated for several defocus values, does not favour the resolution of two such widely differing spacings simultaneously.

7.5 (i) - The Pure Paraffins.

Plate 19 shows an areas of a crystal of $\text{nC}_{32}\text{H}_{66}$. The molecules have crystallised in straight rows, without evidence of the undulations which are apparent in phospho-lipid crystals (Fryer & Dorset 1987). The majority of the chain ends must be packed in one plane, without significant lateral translations along the chain axis. There are visible changes in the direction of the lattices, however, with what appear to be amorphous regions in between. An example of one of these amorphous regions is marked on the Plate; it forms a wedge-shaped division between the crystalline regions, the lattices of which undergo an 18° change in direction. Measurements of other areas of C_{32} show that these changes in direction are not always at a constant angle, so epitaxial crystallisation of the

paraffin along one particular face of another paraffin crystal seems unlikely. The change in orientation of the paraffin may be following a change in orientation of the benzoic acid on which it was crystallised.

There may also be a screw-type dislocation occurring in the crystal, although this cannot be confirmed with only a two-dimensional projection as evidence. The tapered, apparently amorphous regions may consist of planes of molecules which are tilted slightly out of the Bragg angle, thus preventing them from scattering in phase.

Plates 20 and 21 show areas of $nC_{36}H_{74}$. Like $C_{32}H_{66}$, this paraffin crystallises as a monoclinic unit cell. These areas also show long bands of lattices without the changes in orientation visible on the previous Plate. Several smaller changes are visible however; an example is highlighted in white on Plate 21(b).

Examples of odd-numbered chains with orthorhombic unit cells, $C_{33}H_{68}$ and $C_{37}H_{76}$, are shown in Plates 22 and 23 respectively. As with the C_{36} , the crystal lattices run in a straight line without change in orientation, but not always continuously. This makes it unlikely that a difference in crystal symmetry or chain-end packing is the cause of the changes in orientation in some crystals, but not in others.

A twin boundary can be seen in the micrograph of $C_{37}H_{76}$, and is marked by arrows.

7.5 (ii) - Solid Solutions.

As described in Section 6.3, mixtures of two paraffins with different chain-lengths crystallise to form solid solutions. The specimens are prepared for microscopy in exactly the same way as the pure paraffins. Both even-even and even-odd pairs of paraffins were examined, in varying proportions. A discussion of the lattice dimensions of the crystals follows in Section 7.6.

(a) $C_{37}H_{76}/C_{38}H_{78}$

The difference in chain-length between the two components of this pair is only 1.27\AA . A source of possible incompatibility, however, lies in the symmetry of their unit cells, and the difference in chain-end packing. Plate 24 shows a lattice image of a 1 : 1 solution of this pair. The lattices run straight without changes in orientation, but with the defects found in all of the paraffin samples studied. It is difficult to count defects accurately from such a micrograph, but the concentration appears to be no higher than in the pure paraffin samples. Measurement on an optical bench of diffraction patterns of areas sampled over the negative shows a constant d-spacing, indicating that the true solid solution seems to have formed.

(b) C₃₂H₆₆/C₃₆H₇₄ (even-even).

Images of this pair are shown in the following plates:

Plate 25 : Ratio of components - 3 : 2

Plate 26 and 27: Ratio of components - 1 : 1

Plate 28 : Ratio of components - 2 : 3

Plate 29 : Ratio of components - 1 : 4

Each of the components of this pair has the same symmetry (monoclinic) so it would be expected that they would form a continuous solid solution.

The same type of lattice is visible as in previous plates - straight parallel lines, with spacings intermediate to the two pure components, with localised defects in the lattice and amorphous regions interrupting the lattice. Only a small crystalline area was found of the 2 : 3 ratio.

Only in the solid solution where the ratios are 1 : 1 was there evidence of a change of orientation in the lattice, as well as twinning of crystals; the crystal in plate 27 makes an angle here of 15° and there is no amorphous boundary region, the lattice making a continuous bend.

(c) $C_{33}H_{68}/C_{36}H_{74}$.

Images of these are shown as follows:

Plates 30 and 31 : Ratio of components - 1 : 9

Plates 32 and 33 : Ratio of components - 1 : 4

Plate 34 : Ratio of components - 1 : 3

Plate 3 : Ratio of components - 1 : 1

Plates 36 and 37 : Ratio of components - 3 : 1

Plate 38 : Ratio of components - 9 : 1

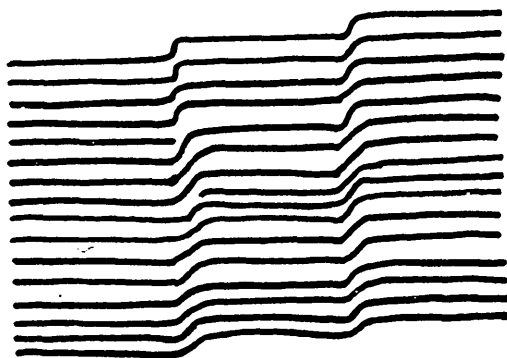
The components of this series of solid solutions have different unit cell symmetries; according to Mnyukh they should crystallise separately. However, electron diffraction studies (Dorset 1985) and the optical analysis of the above Plates show that they do form solid solutions at various ratios.

In Plates 30 and 31, the longer component is well in excess, and the shorter component is expected to leave voids at the chain ends. The lattices, however, appear as in previous plates without any features to distinguish them from the pure paraffins. Plate 30, which is a smaller enlargement, shows clearly the lath-shaped form of crystals grown by the epitaxial method. Plates 32 and 33, of C_{33} and C_{36} in the ratio 1 : 4 show step-like growth at the edge of a crystal.

The pair of components with $C_{33} : C_{36}$ in the ratio 1 : 3 (Plate 34) again has straight lattices which show slight changes in orientation, and which are best visible with the page held horizontally to the eye.

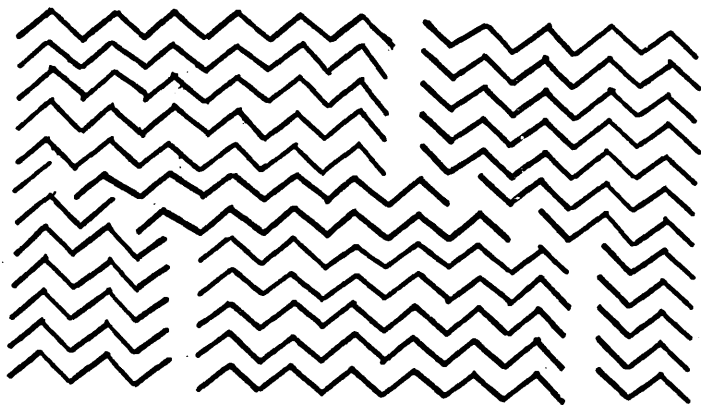
Plate 35 shows a region of the equimolar solution of this paraffin pair, showing a twin boundary which finishes in a split in the crystal.

The 3 : 1 blend of components (Plates 36 and 37) behaves slightly differently. The lattices run in an almost constant orientation, except that in one region (Plate 37) there is a series of sideways displacements of the rows which appear as sketched below.



Sometimes there appears to be no break in the lattice, and in some cases a defect is visible resembling an edge dislocation.

Each lattice line represents the end plane of an array of paraffin chains packed side by side; the discontinuities may be the result of lateral translations of chains:



With short straight lines representing the molecular chains, a possible representation of the crystal is sketched below:

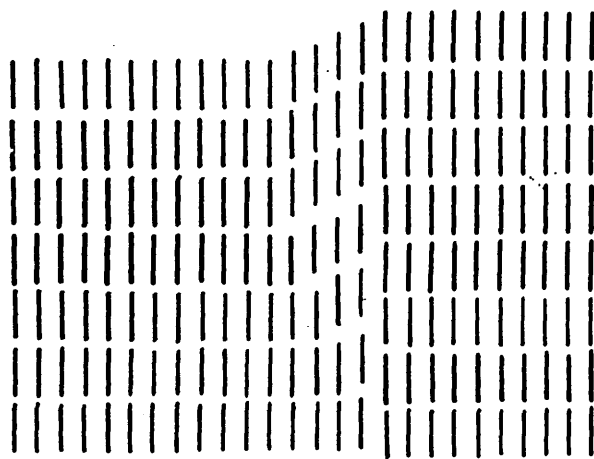


Plate 38 is the same pair of paraffins in a 9 : 1 ratio. The features of the micrographs are just as before, in spite of the

fact that the shorter chain is now in excess and the longer chain must accommodate itself into the lattice.

There is no evidence from these lattice images of any separation of the components of a solid solution on crystallisation. It appears from optical bench analysis of the negatives, in which the spacing is intermediate to the two pure paraffin chains and does not vary over the area of the negative, that the two different paraffin chains occupy sites at random in the crystal, and do not have a tendency to pack "like-with-like".

7.6 -Changes in Lattice Spacings of Solid Solutions of
Paraffins.

The following solid solutions were prepared as described in
 Section 4.4:

$C_{32}H_{66} / C_{36}H_{74}$		$C_{33}H_{68} / C_{36}H_{74}$	
(even)	(even/ortho)	(odd)	(even/ortho)
1.00	: 0.00	1.00	: 0.00
0.91	: 0.09	0.91	: 0.09
0.77	: 0.23	0.76	: 0.24
0.60	: 0.40	0.60	: 0.40
0.53	: 0.47	0.52	: 0.48
0.40	: 0.60	0.40	: 0.60
0.27	: 0.73	0.27	: 0.73
0.20	: 0.80	0.20	: 0.80
0.09	: 0.91	0.10	: 0.90
0.00	: 1.00	0.00	: 1.00

$C_{36}H_{74} / C_{38}H_{78}$		$C_{37}H_{76} / C_{38}H_{78}$	
(even)	(even)	(odd)	(even)
1.00	: 0.00	1.00	: 0.00
0.80	: 0.20	0.80	: 0.20
0.60	: 0.40	0.60	: 0.40
0.50	: 0.50	0.50	: 0.50
0.40	: 0.60	0.40	: 0.60
0.20	: 0.80	0.20	: 0.80
0.00	: 1.00	0.00	: 1.00

The four pairs of solid solutions were prepared in the 0kl orientation, and lattice images recorded in order to determine the variation in their lattice spacings according to the ratio of their components. Two were of even-even pairs (C_{32}/C_{36} and C_{36}/C_{38}), and two of odd-even pairs (C_{33}/C_{36} and C_{37}/C_{38}). An attempt was made to crystallise a 1 : 1 solution of $C_{44}H_{90}$ and $C_{19}H_{40}$, to find out whether long paraffin chains could incorporate molecules less than half their length; however, the combination did not crystallise at all, and this appears to support Mnyukh's theory that only molecules which are similar in length may form continuous solid solutions.

Lattice images of the crystallised solid solutions were mounted in the optical bench, and the optical diffraction patterns were measured from several areas of each micrograph and from several micrographs where possible. The resultant graphs of spacing versus composition are shown in Figs. 7.1 to 7.4. Vegard's law is represented by a straight broken line connecting the spacings for the pure paraffins. Error bars represent the standard deviations in the measurements.

The C_{37}/C_{38} pair of paraffins has a difference in length of only 2.54\AA between the component molecules, but it is also a pair in which the symmetry difference might be a barrier to continuous solid solution formation: $C_{38}H_{78}$ has an orthorhombic unit cell and $C_{37}H_{76}$ a monoclinic one. The

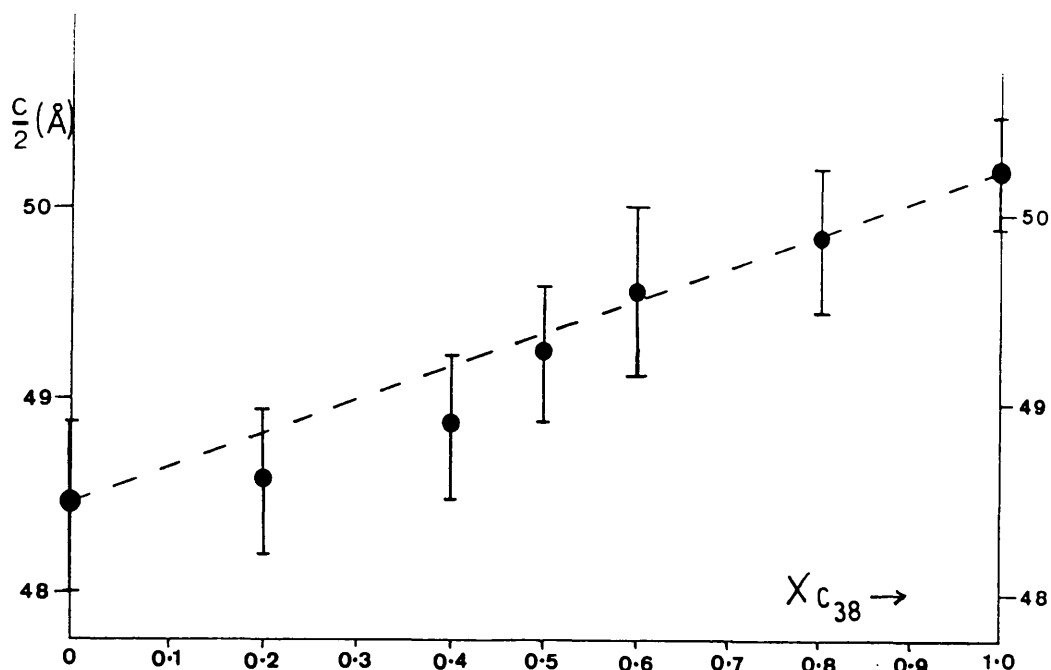


Fig. 7.1 Plot of lamellar spacing against proportion of $C_{38}H_{78}$ in a C_{37}/C_{38} solid solution (Vegard's law behaviour shown by dotted line).

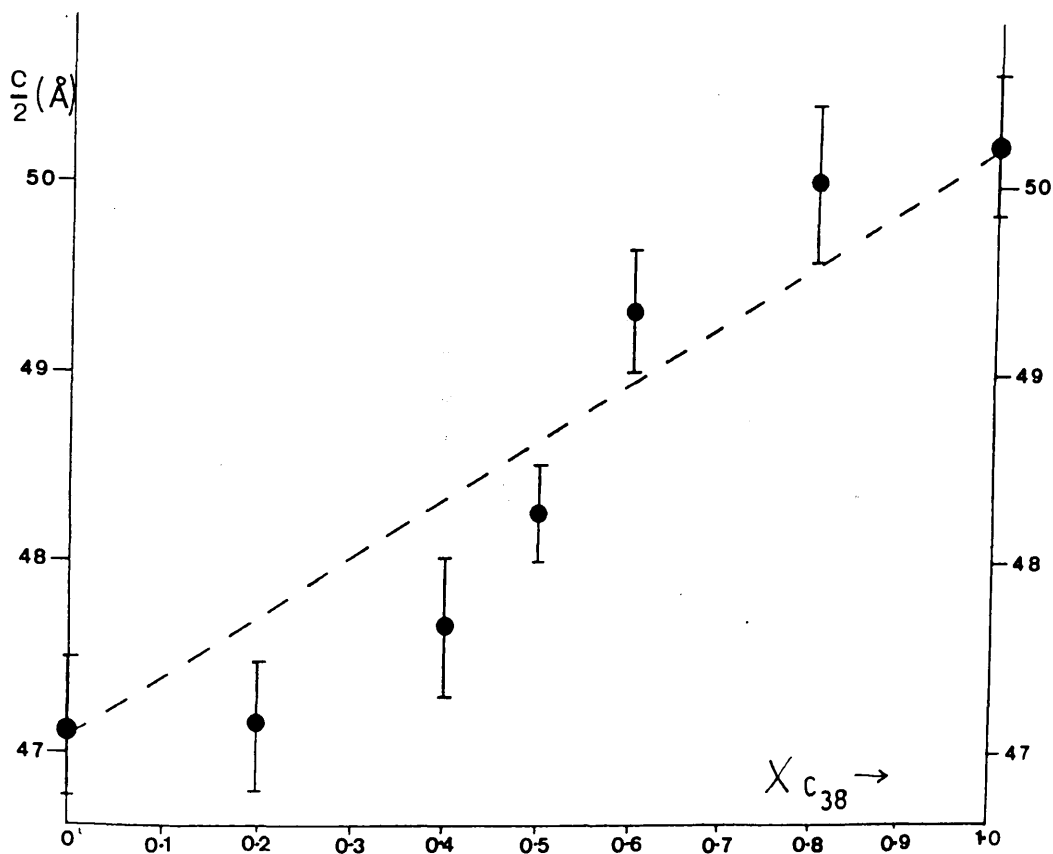


Fig. 7.2 Plot of lamellar spacing against proportion of $C_{38}H_{78}$ in a C_{36}/C_{38} solid solution.

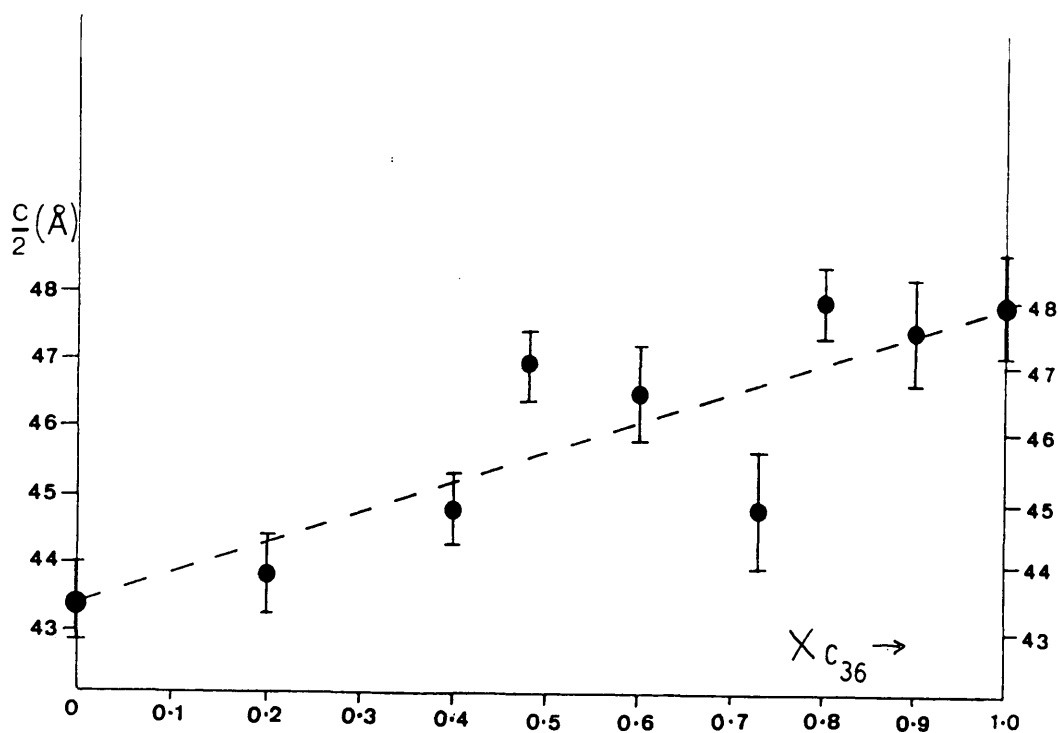


Fig. 7.3 Plot of lamellar spacing against proportion of $C_{36}H_{74}$ in a C_{33}/C_{36} solid solution.

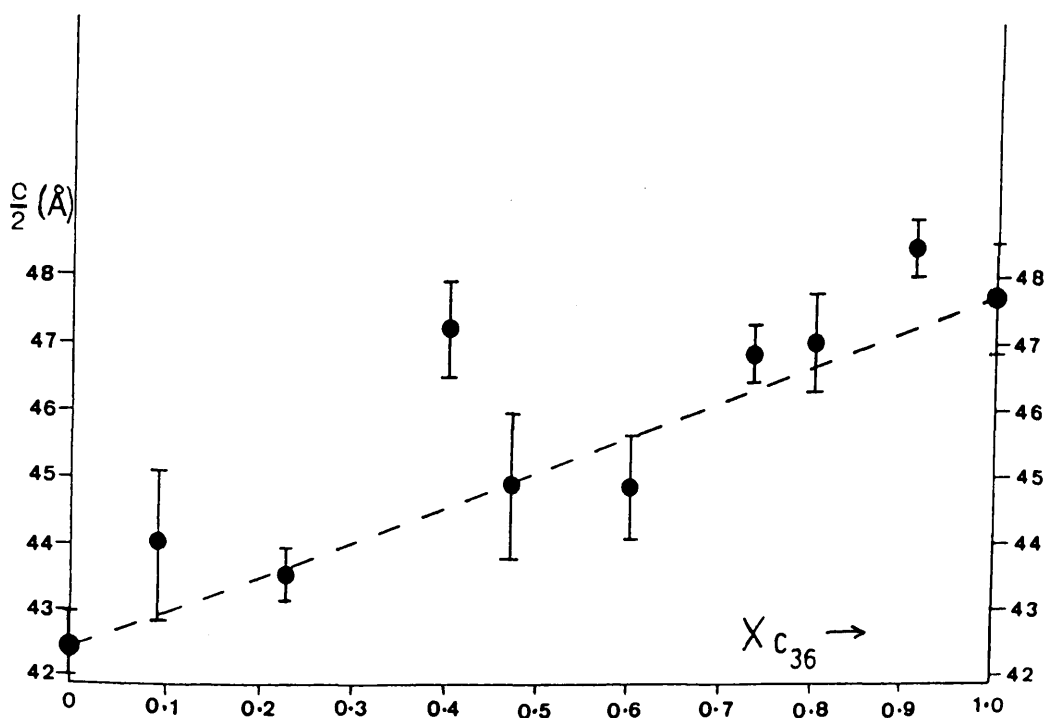


Fig. 7.4 Plot of lamellar spacing against proportion of $C_{36}H_{74}$ in a C_{32}/C_{36} solid solution.

measurement of very small differences in lamellar spacing between the members of the series is also a cause of a comparatively large error in the observed spacings of the optical diffraction patterns.

At low concentrations of the higher component this pair exhibits a negative deviation from Vegard's law; at higher concentrations the theoretical values are more closely approached.

A similar pattern emerges for the C_{36}/C_{38} pair, the components of which are also fairly close in length, although this time they both have the same (orthorhombic) unit cell symmetry. At low concentrations a negative deviation is observed, which becomes a positive deviation at high concentrations of the longer paraffin. The positive deviation can be accounted for by the chain-ends of the long component protruding and leaving voids in the plane of the chain-ends; the slight negative deviation may be the result of kinks in the long chains allowing the layers to pack closely together.

The trend for the C_{33}/C_{36} and the C_{32}/C_{36} pairs is less clear, but there may be a tendency in these two solutions to follow the same pattern as the first two; there appears to be a slight negative deviation from Vegard's law where the shorter chain predominates and a slight positive deviation where the

longer chain predominates. The trend would thus appear to be as shown in Fig. 7.5 -

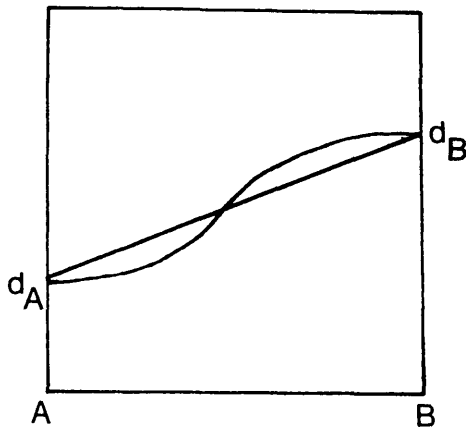


Fig. 7.5 The deviation from Vegard's law behaviour displayed by the paraffin solid solutions described in this chapter.

This behaviour differs from that observed in electron diffraction studies by Dorset (1985), where the lattice spacing showed a positive deviation from Vegard's law at all concentrations. In a recent paper, however, Dorset (1987) describes a step function governing the increase in lamellar spacing with the proportion of the larger component. He concludes that it is not possible to interpret the spacings of a solid solution in terms of Vegard's law and that the binary paraffin solid at any concentration of longer chain length component adopts the structure of the next longest pure paraffin, with some concentrations able to adopt more than one structure.

There are insufficient data in Figs. 7.1-7.4 to detect a step function in the increase in lamellar spacing, but the points on the plots do not appear to correspond to the spacings of the intermediate pure paraffins, as they increase gradually. This is also true for the solution with only one carbon atom's difference in the components, C_{37}/C_{38} , although this may be the result of the averaging effect of the optical diffraction technique.

High-resolution imaging of paraffin solid solutions complements diffraction studies in that it allows the lattice image to be viewed directly with its defects, but it does not replace the accurate crystallographic data available from diffraction techniques which are required to draw conclusions about the chain-end packing.

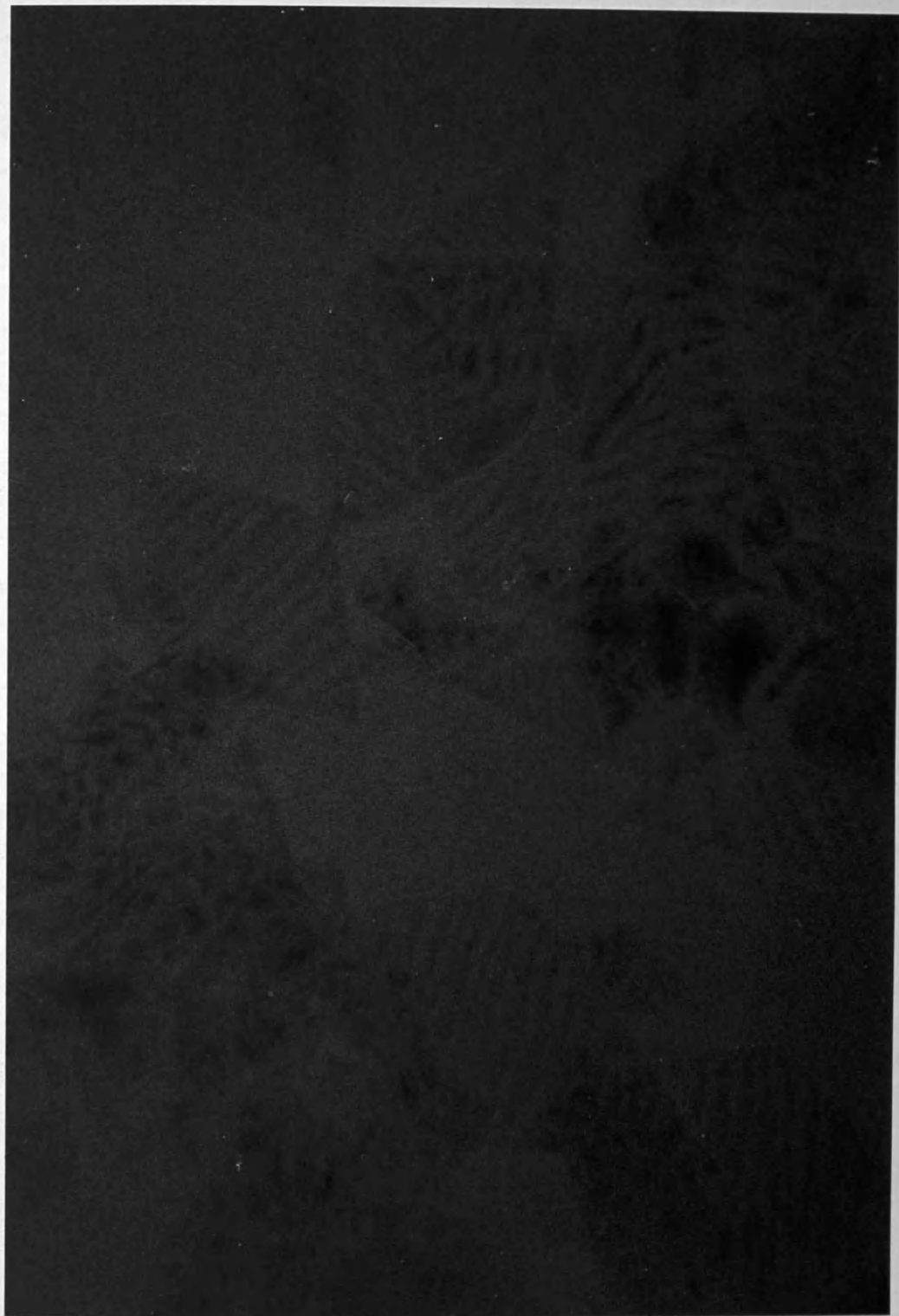


Plate 4 : Image of solution-grown crystals of $C_{44}H_{90}$, showing bend contours.

(The magnification of this Plate is unknown as it was taken from the defocused central beam of a diffraction pattern, but the crystals are probably $1\ \mu$ in length).

Plate 5 : Solution-grown, lozenge shaped monolamellar
crystals of $nC_{60}H_{122}$
x 49,800.



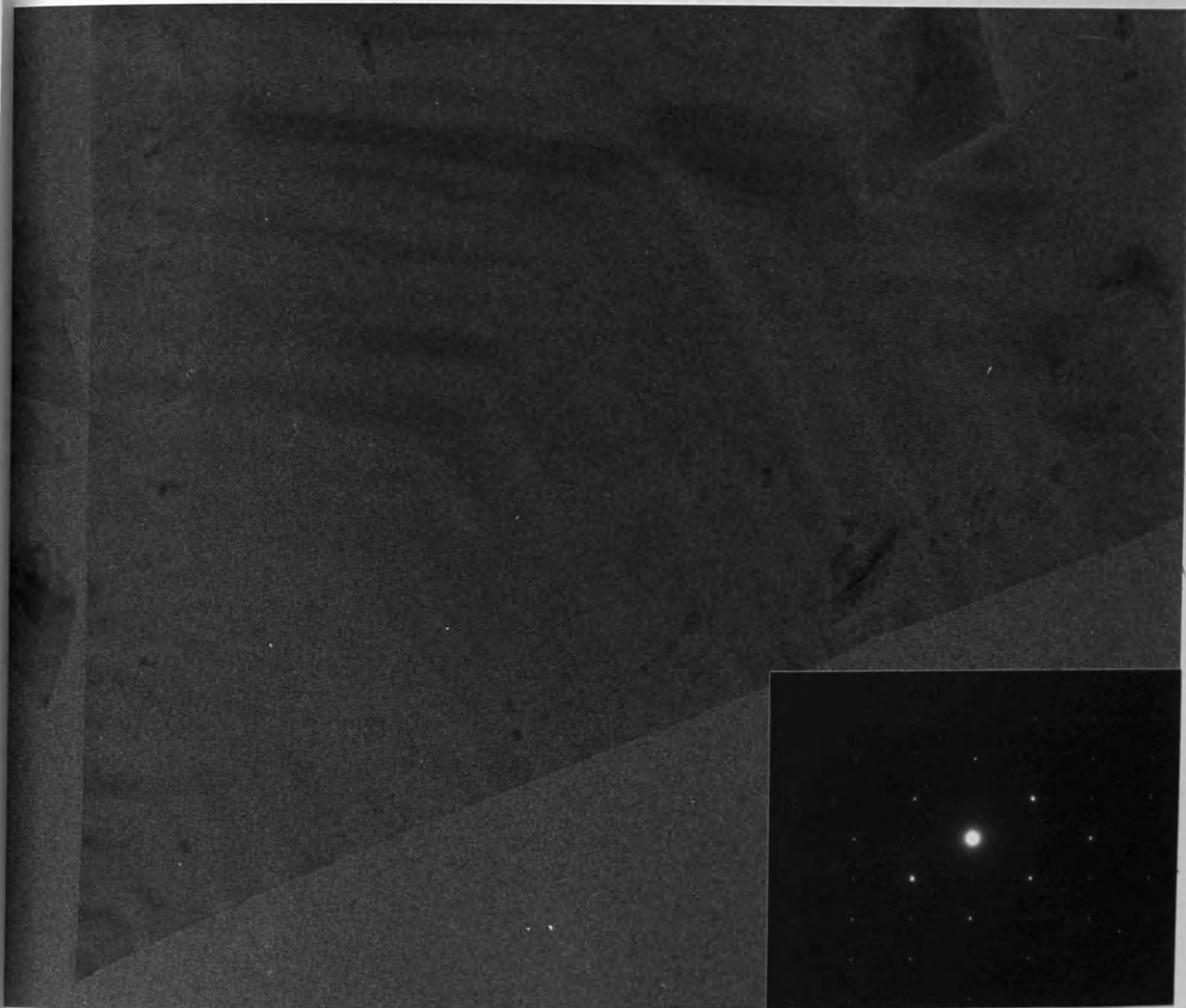


Plate 6 : $C_{82}H_{166}$ crystal with $\langle 130 \rangle$ striations, grown from solution.

x 20,000

Plate 7 : Paraffin crystal, $C_{82}H_{166}$ showing change in surface features with electron dose

	x 30,000	
	$e^-/\text{\AA}^2$	C/cm^2
(a)	1.2	1.92×10^{-3}
(b)	1.8	2.88×10^{-3}
(c)	2.4	3.84×10^{-3}
(d)	3.0	4.80×10^{-3}

a



b



c



d





Plate 8 : Solution-grown lozenge-shaped crystal of
 $\text{nC}_{82}\text{H}_{166}$ taken at 181K
x 20,000

Plate 9 : Area of a low-dose micrograph of a paraffin in the $hk0$ orientation, with no detail visible ($2\text{cm} \equiv 10\text{nm}$), and the optical diffraction patterns from four such micrographs:

- (a) $\text{C}_{36}\text{H}_{74}$
- (b) $\text{C}_{44}\text{H}_{90}$
- (c) $\text{C}_{60}\text{H}_{122}$
- (d) $\text{C}_{82}\text{H}_{166}$



a



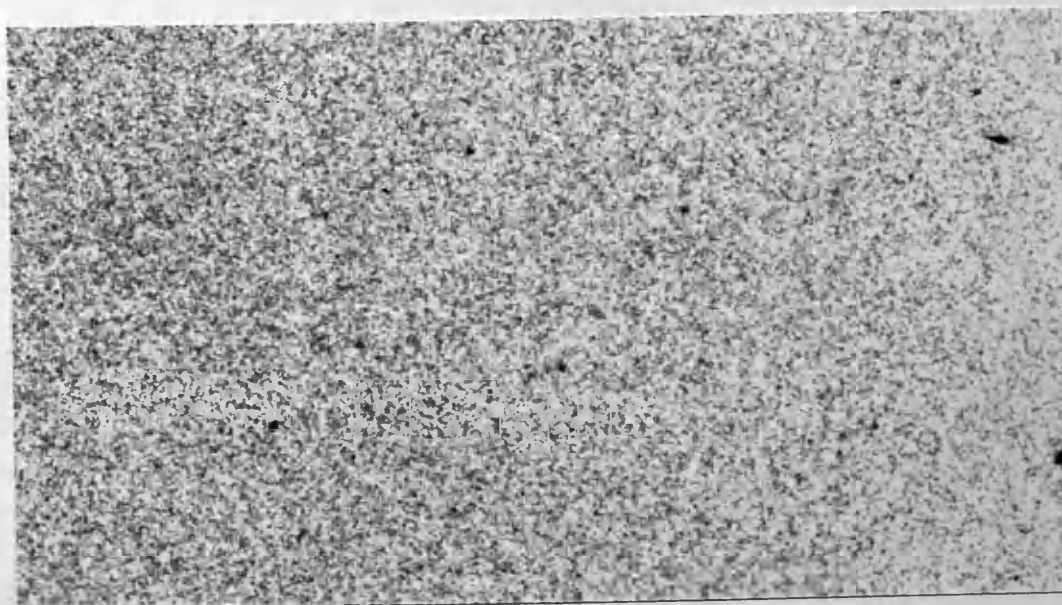
b



c



d



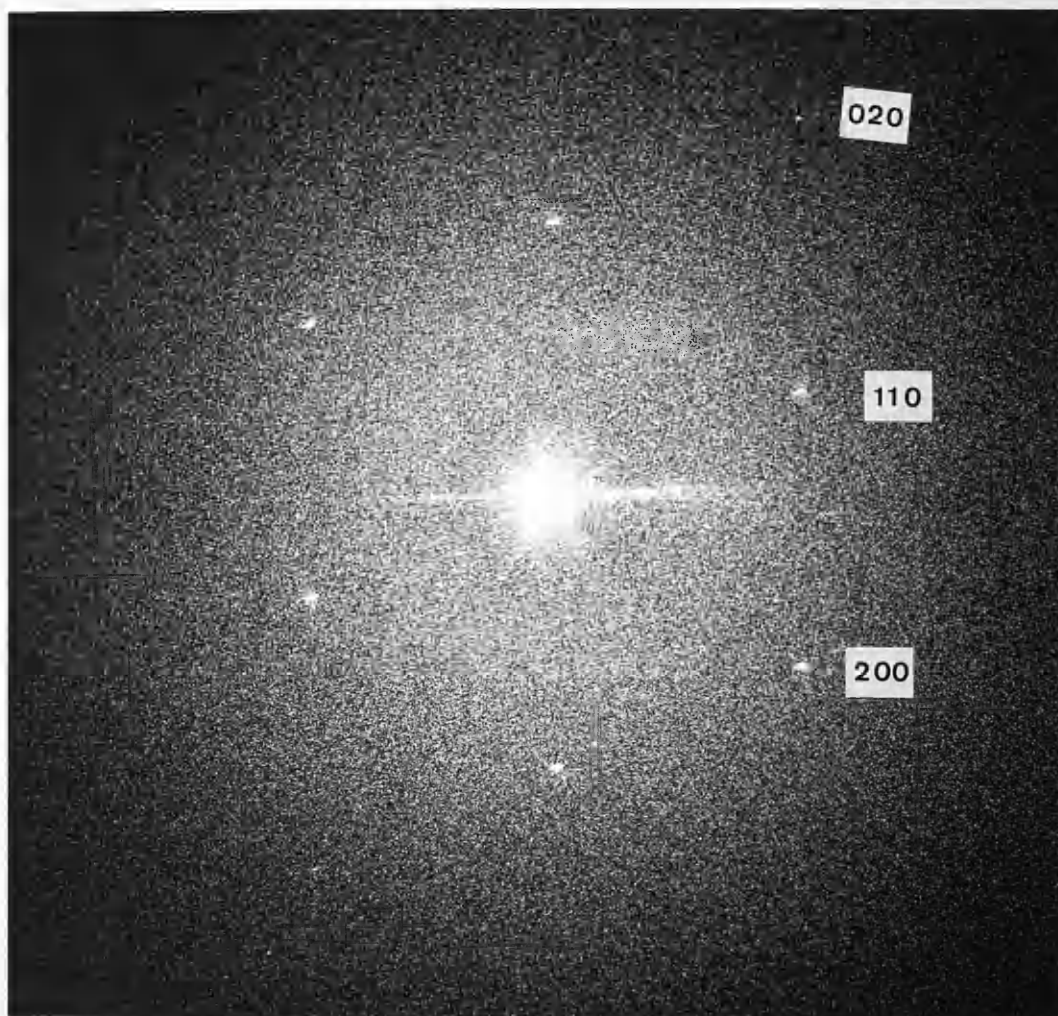
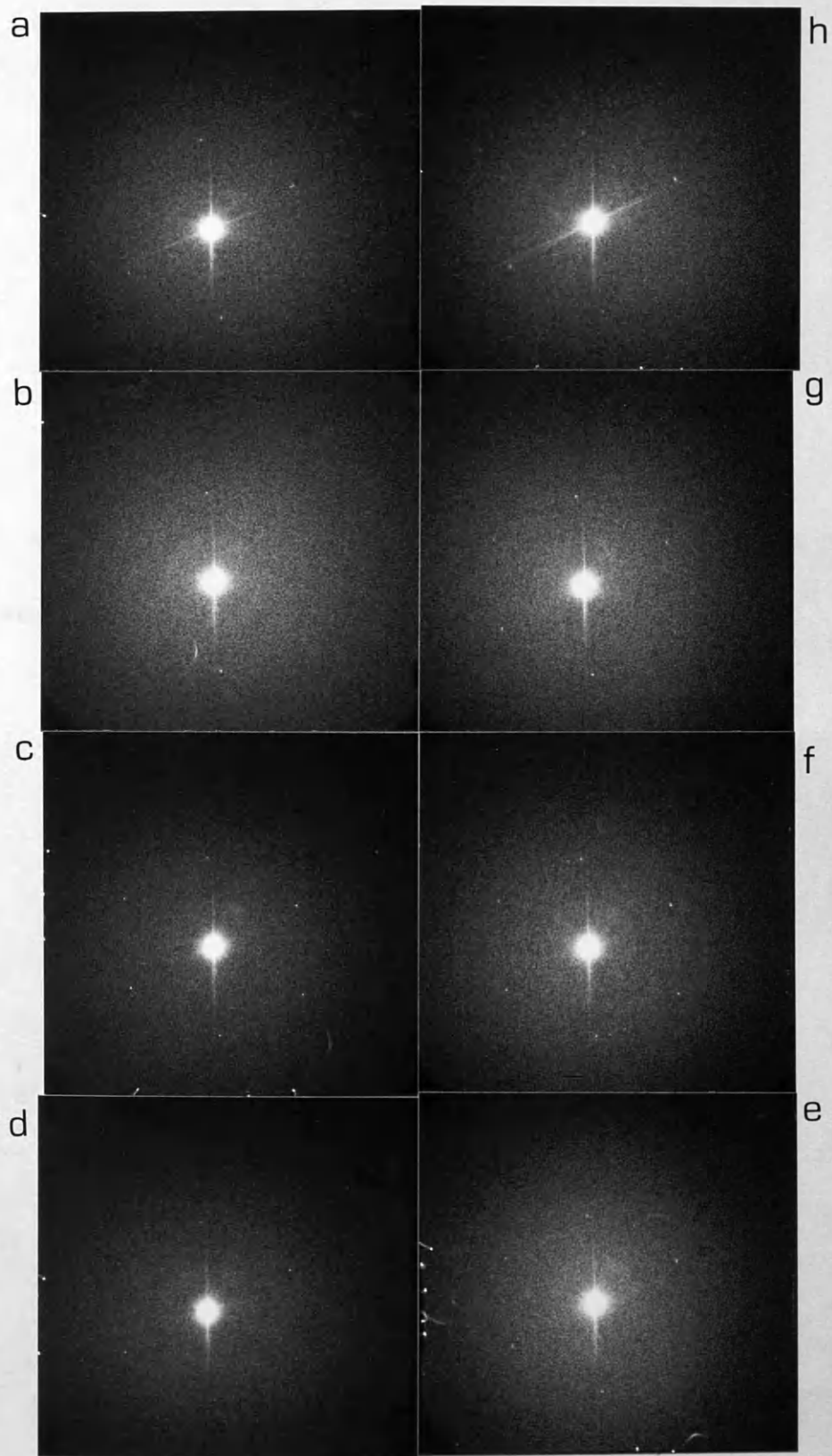
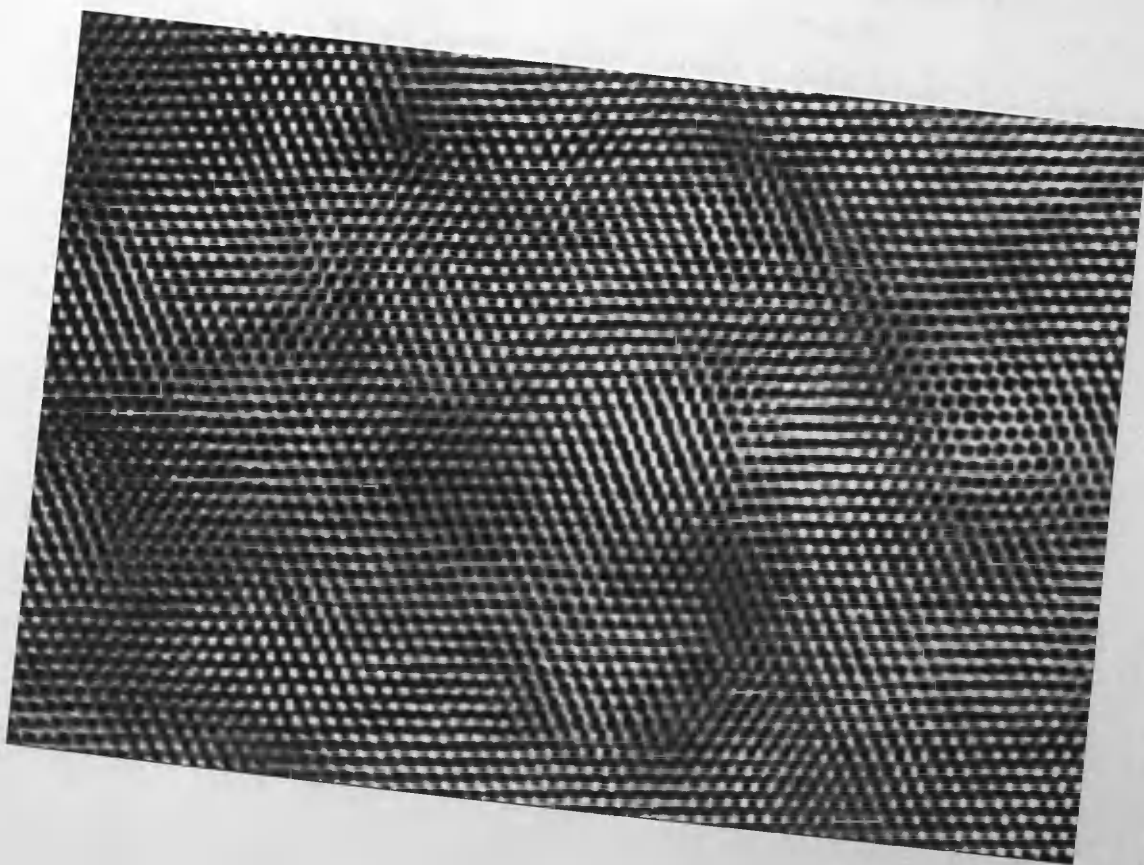
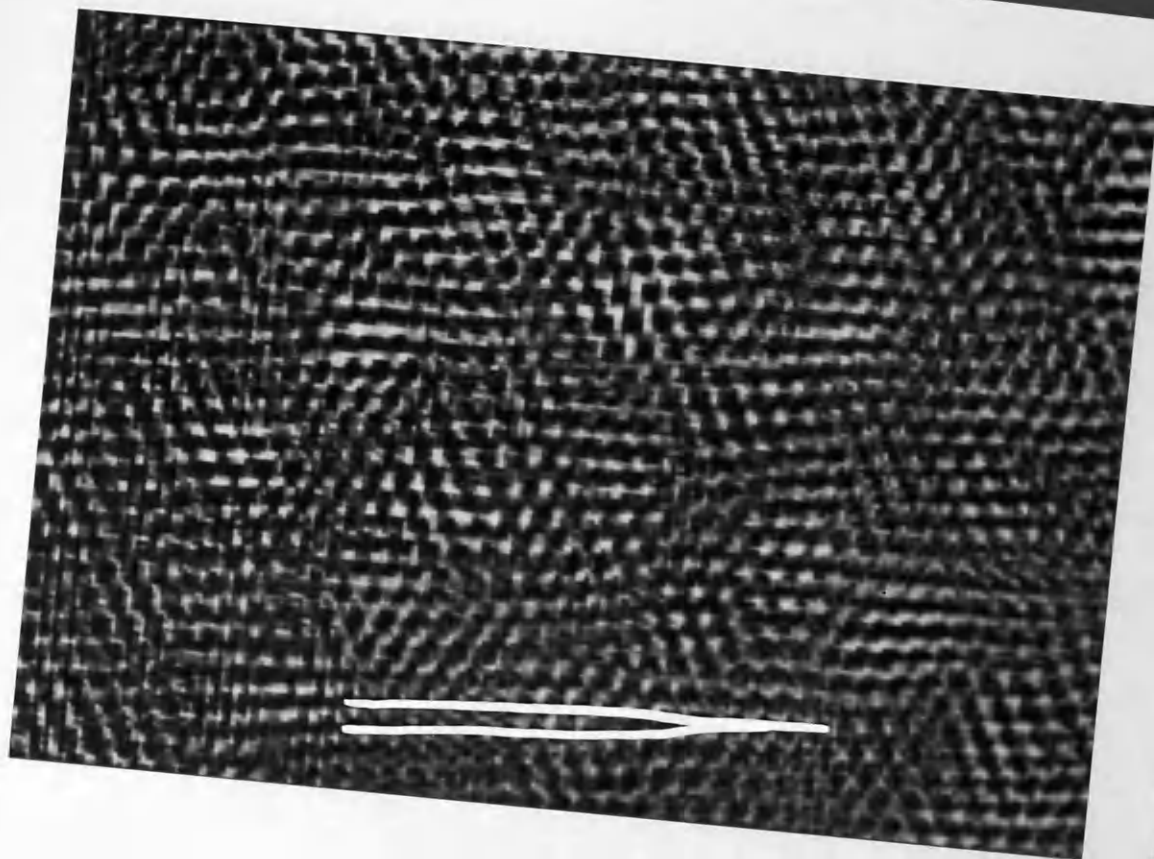


Plate 10 : Optical diffraction pattern of C_{32}/C_{36} solid solution, mole ratio 2 : 3 showing 020 reflections (hk0 orientation).





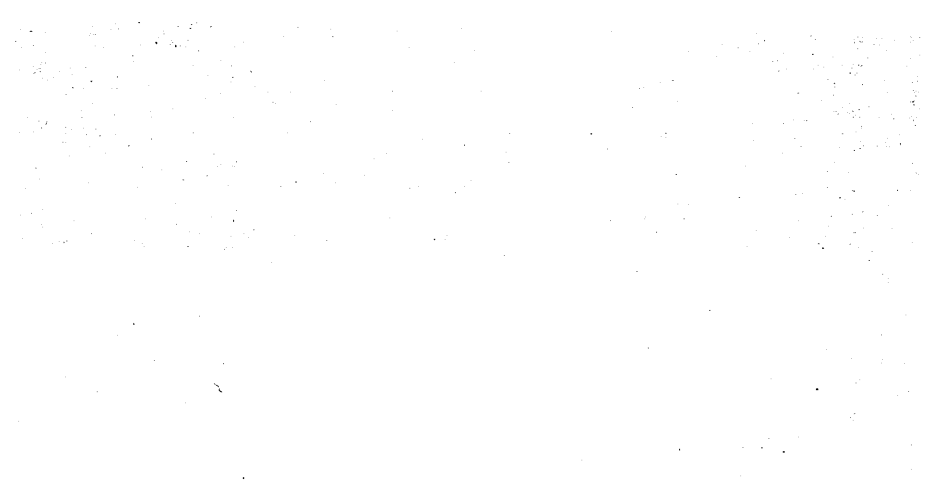
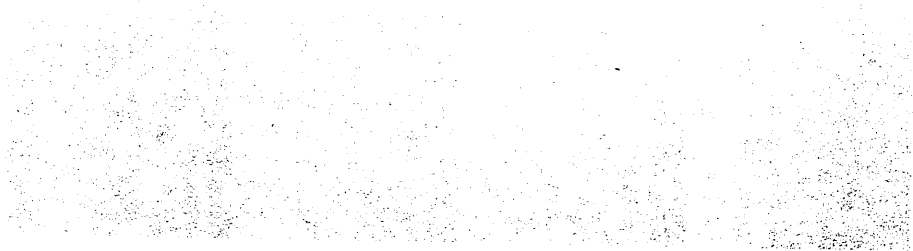


Plate 13 : (a) Part of a 300 x 300 pixel area of a Fourier
reconstruction of $C_{60}H_{122}$ in the 0k1
orientation (window radius 3 pixels)

(b) As above, but sampled area 720 x 720 pixels.



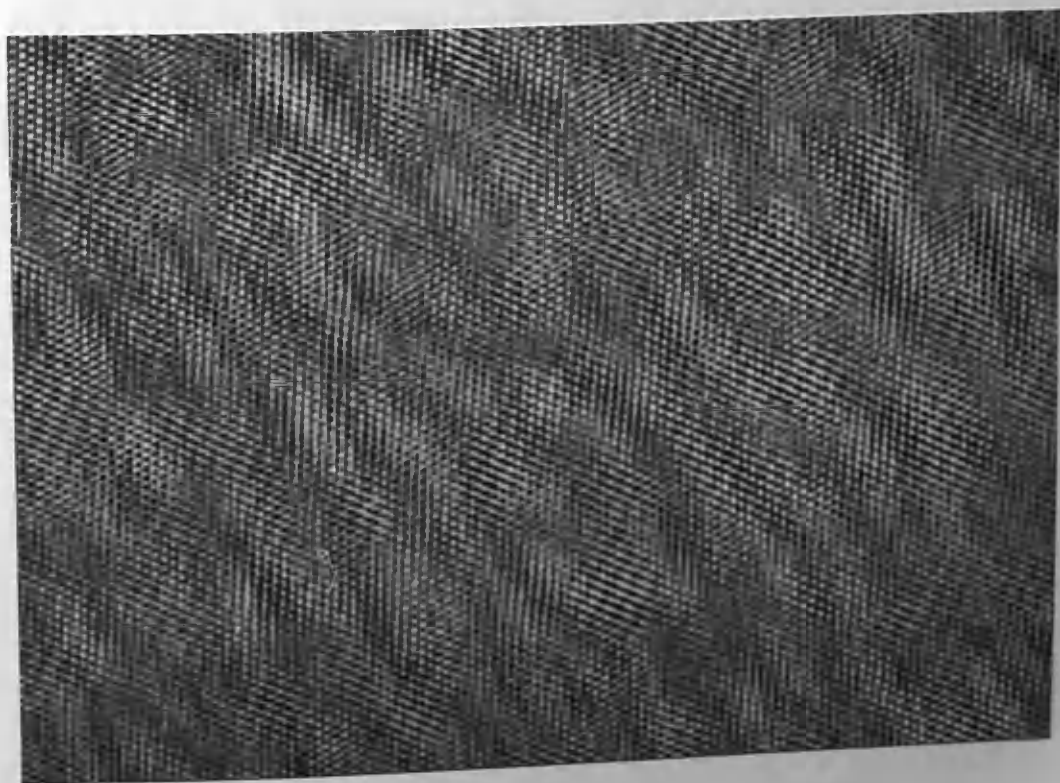
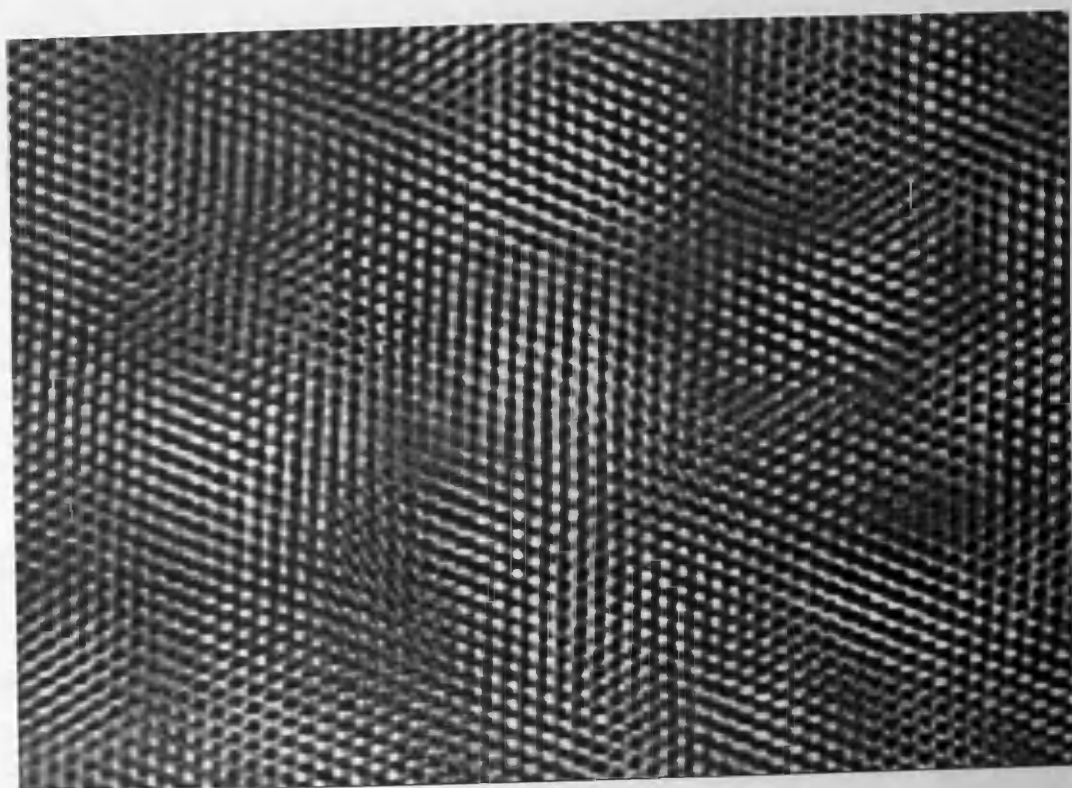


Plate 14 : (a) Part of a 300 x 300 pixel area of a Fourier reconstruction of $C_{82}H_{166}$ in the 0k1 orientation (window radius 3 pixels)

(b) As above, but sampled area 600 x 600 pixels.

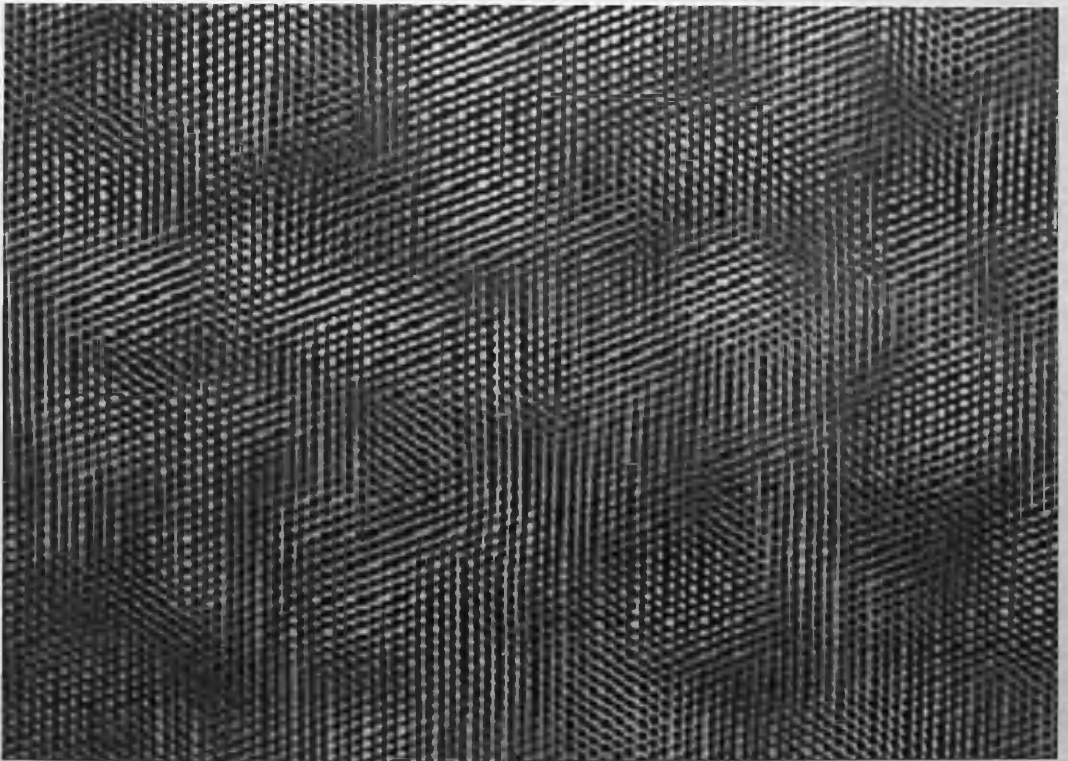
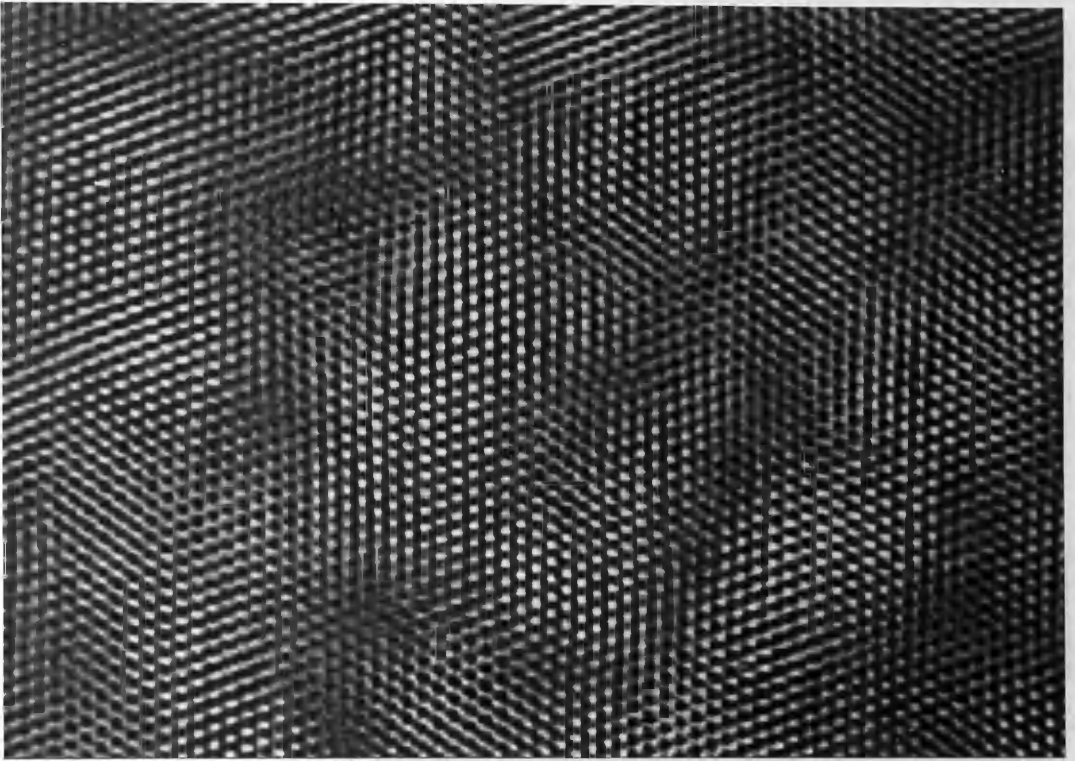
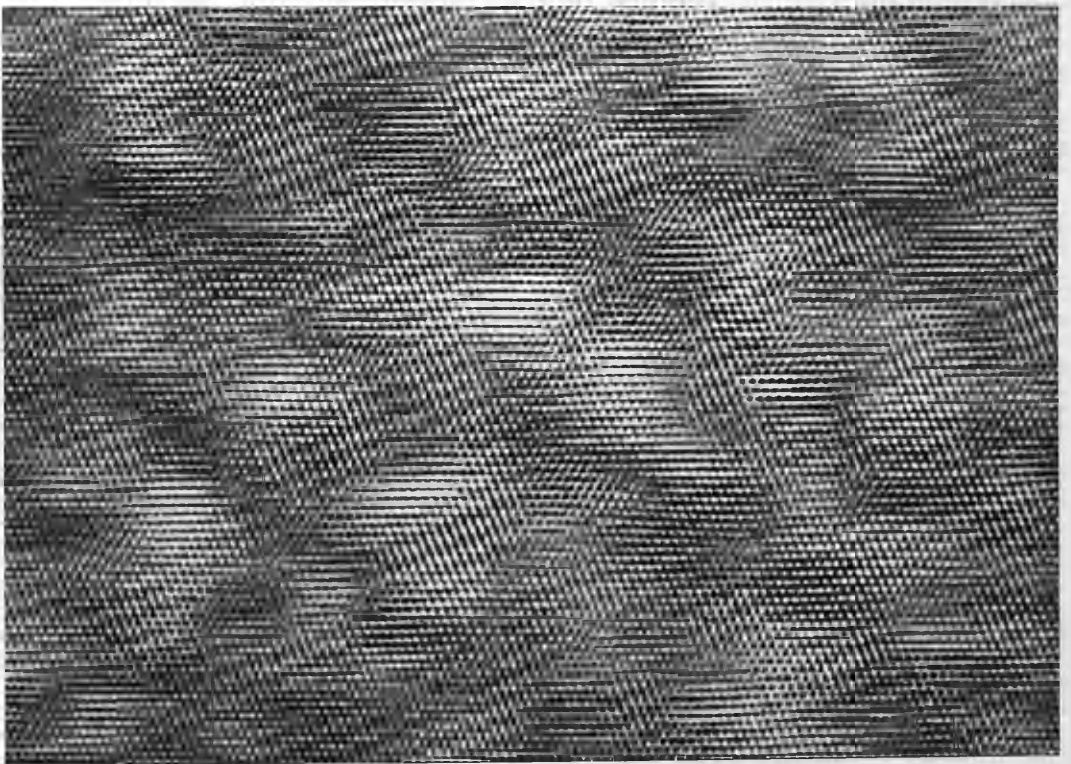
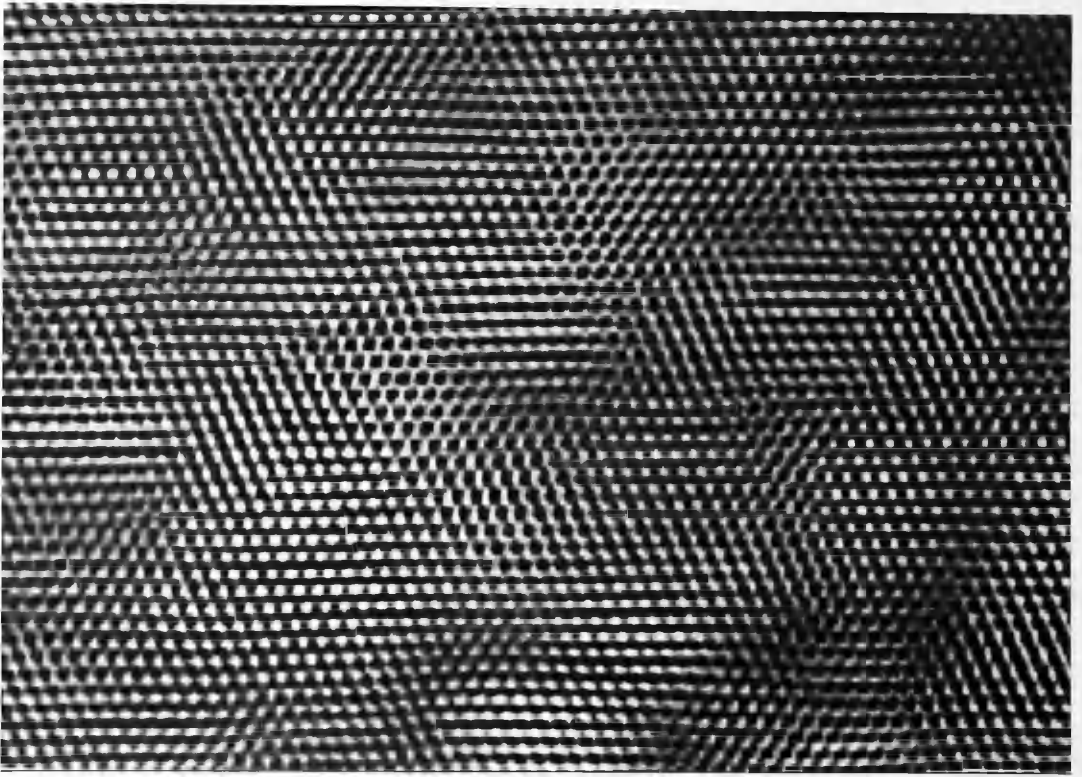


Plate 15 : (a) Part of a 300 x 300 pixel area of a Fourier reconstruction of a solid solution of C_{32}/C_{36} , mole ratio 2 : 3 (window radius 3 pixels)

(b) As above, but sampled area 720 x 720 pixels.

Plate 16 : (a) 700 x 700 pixel Fourier reconstruction of $C_{36}H_{74}$, filtered with a window function of 5 pixels diameter (0k1 orientation),
(b) the same area of crystal filtered with a 1 pixel window function.



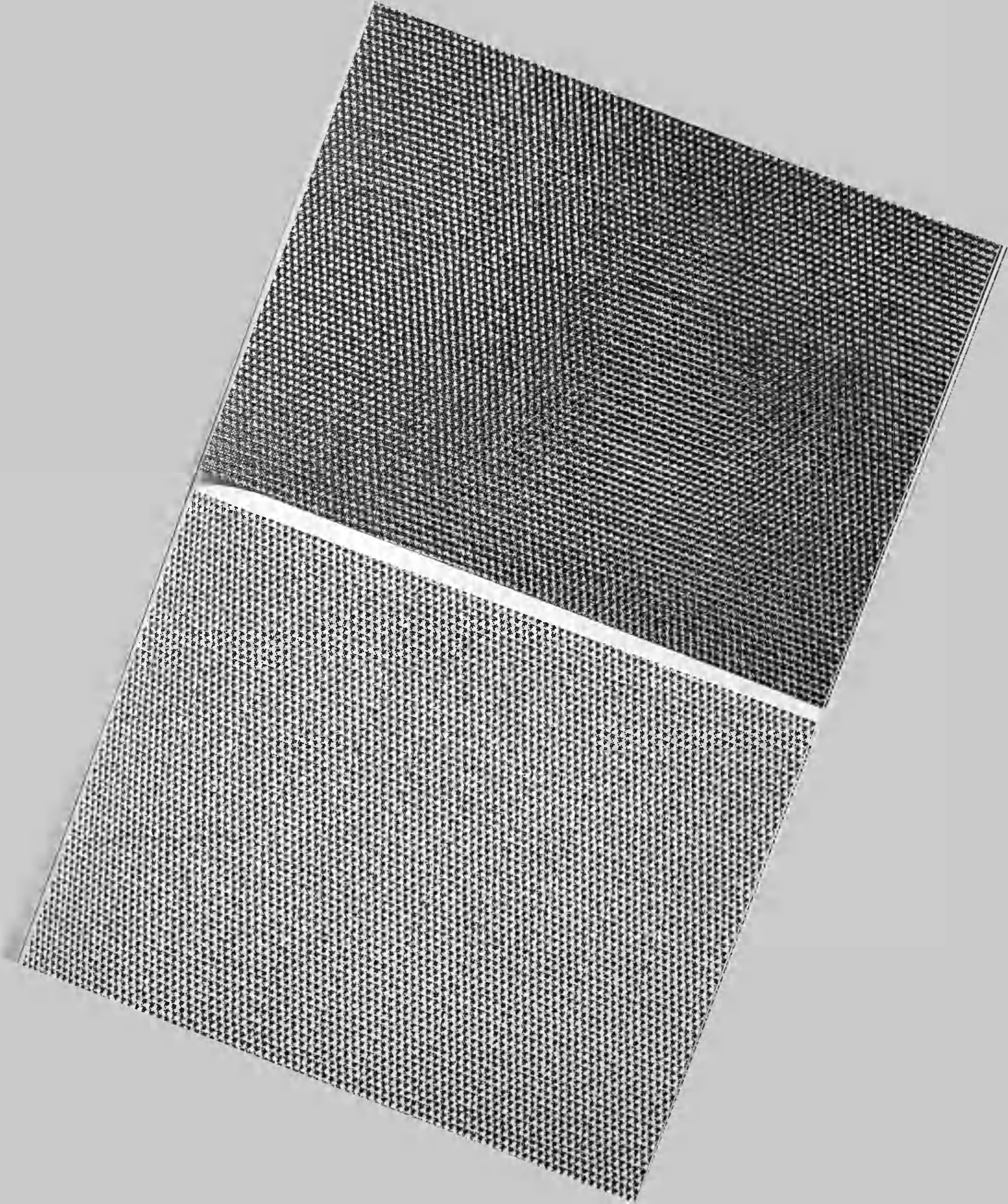


Plate 17 : (a) 700 x 700 pixel Fourier reconstruction of $C_{82}H_{166}$, filtered with a window function of 5 pixels diameter (0kl orientation),
(b) The same area of crystal filtered with a 1 pixel window function.

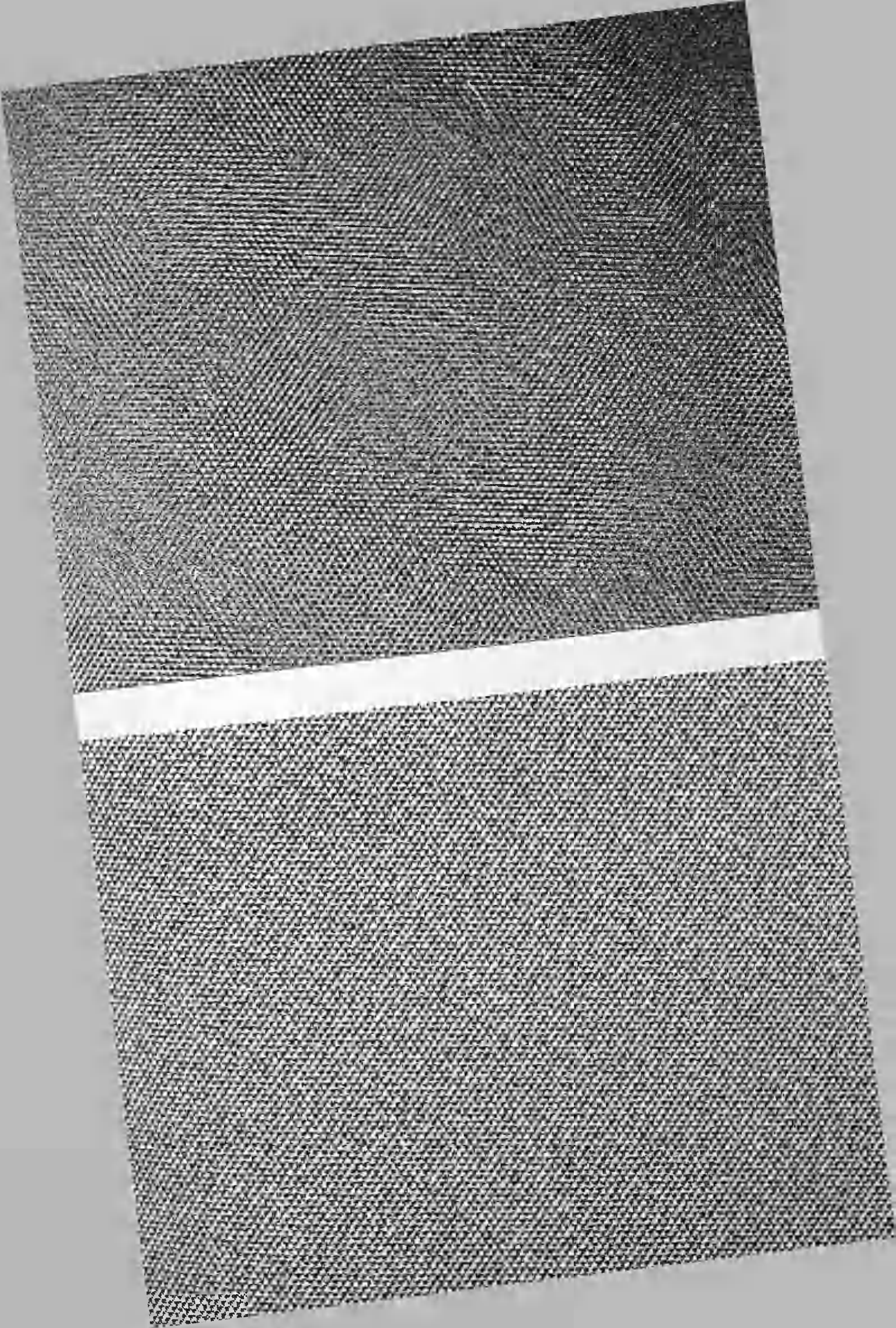


Plate 18 : Three Fourier reconstructions of paraffins in the $hk0$ orientation:

- (a) $C_{36}H_{74}$
- (b) C_{32}/C_{36} solid solution, mole ratio 3 : 1
- (c) C_{32}/C_{36} solid solution, mole ratio 1 : 1

Horizontal lines on the images are due to the raster; examples of "defects" are marked with arrows.

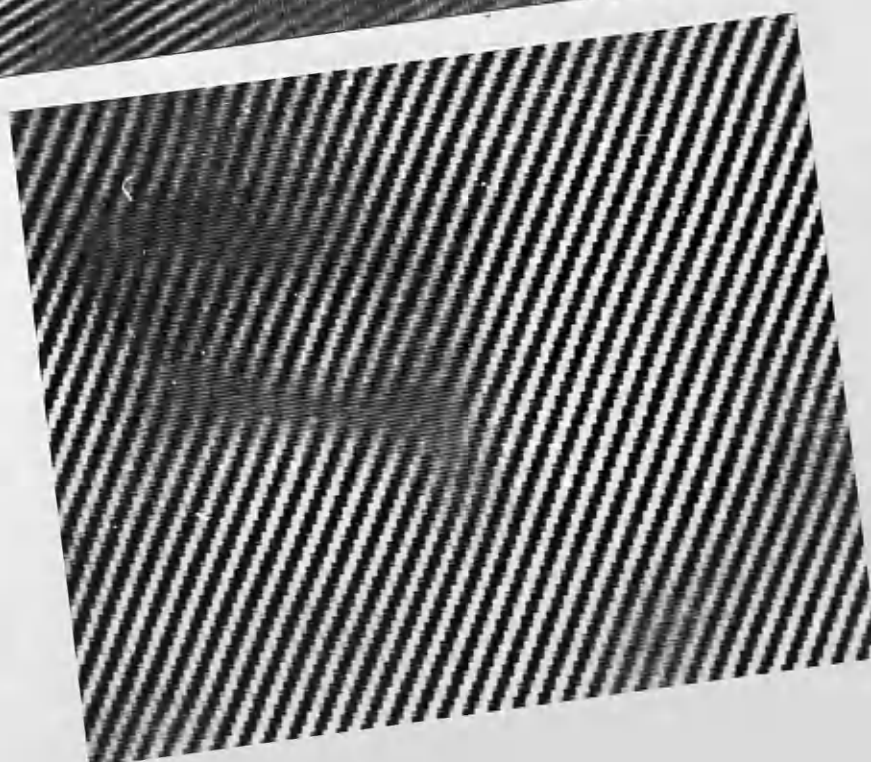
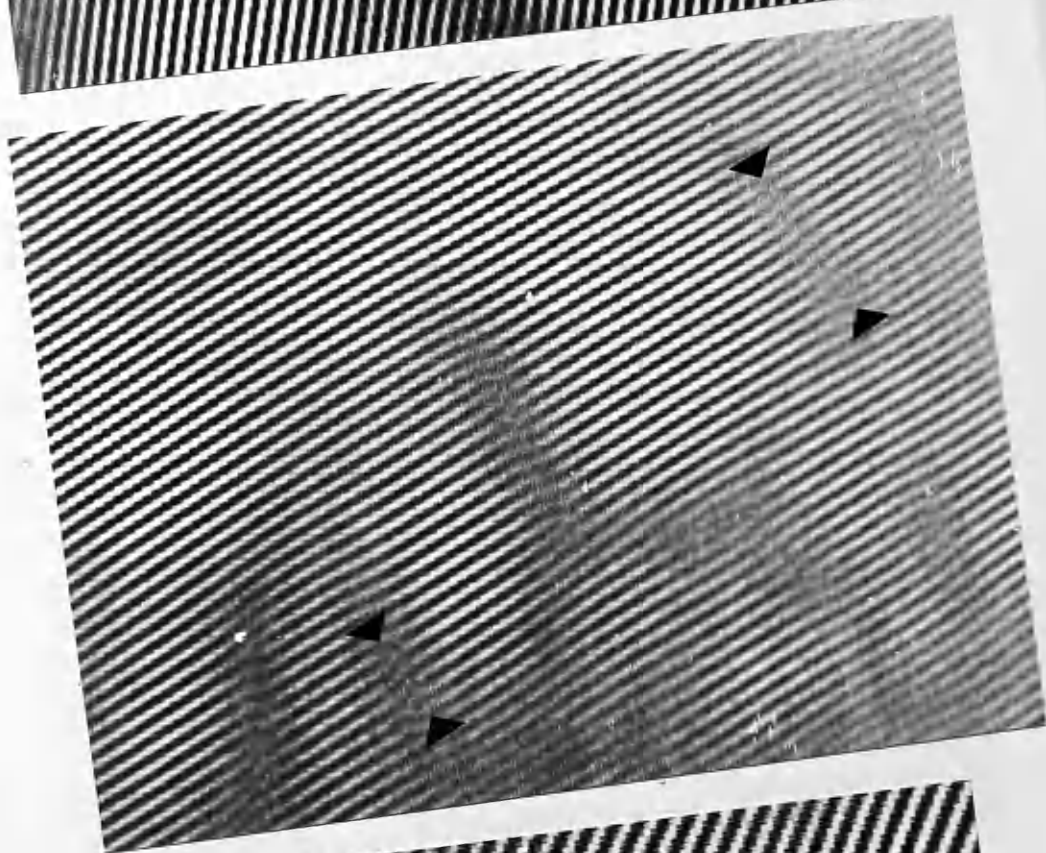
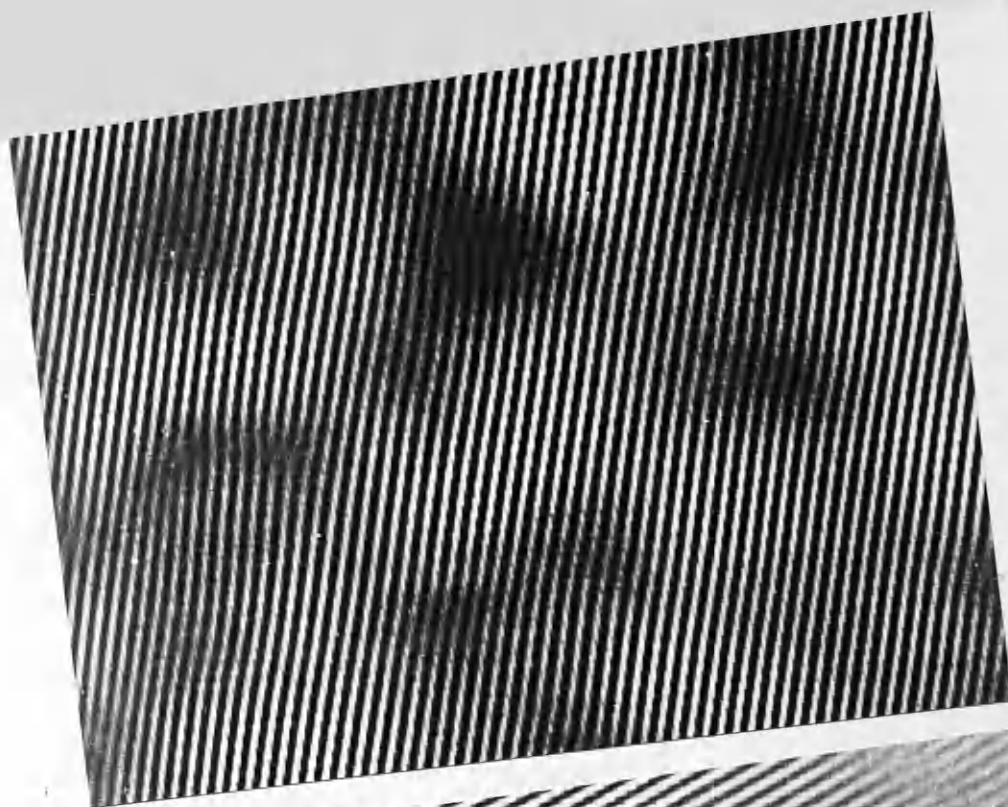


Plate 19 : Epitaxially-grown crystal of a pure paraffin,
 $n\text{C}_{32}\text{H}_{66}$

x 263,500

Lattice spacing 42.5\AA

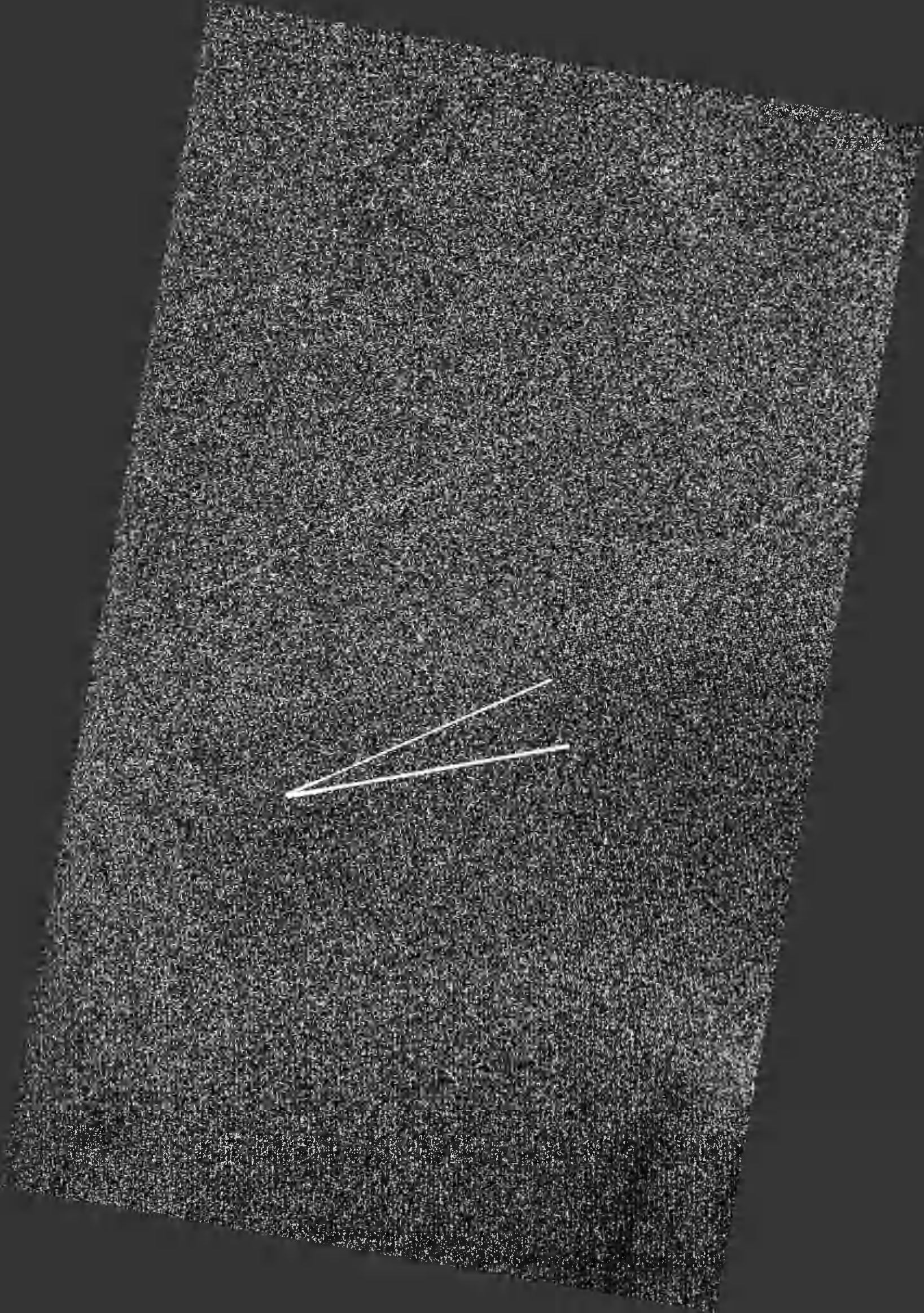
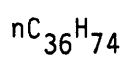


Plate 20 (a): Epitaxially-grown crystal of a pure paraffin,



x 263,500

Lattice spacing 47.5\AA

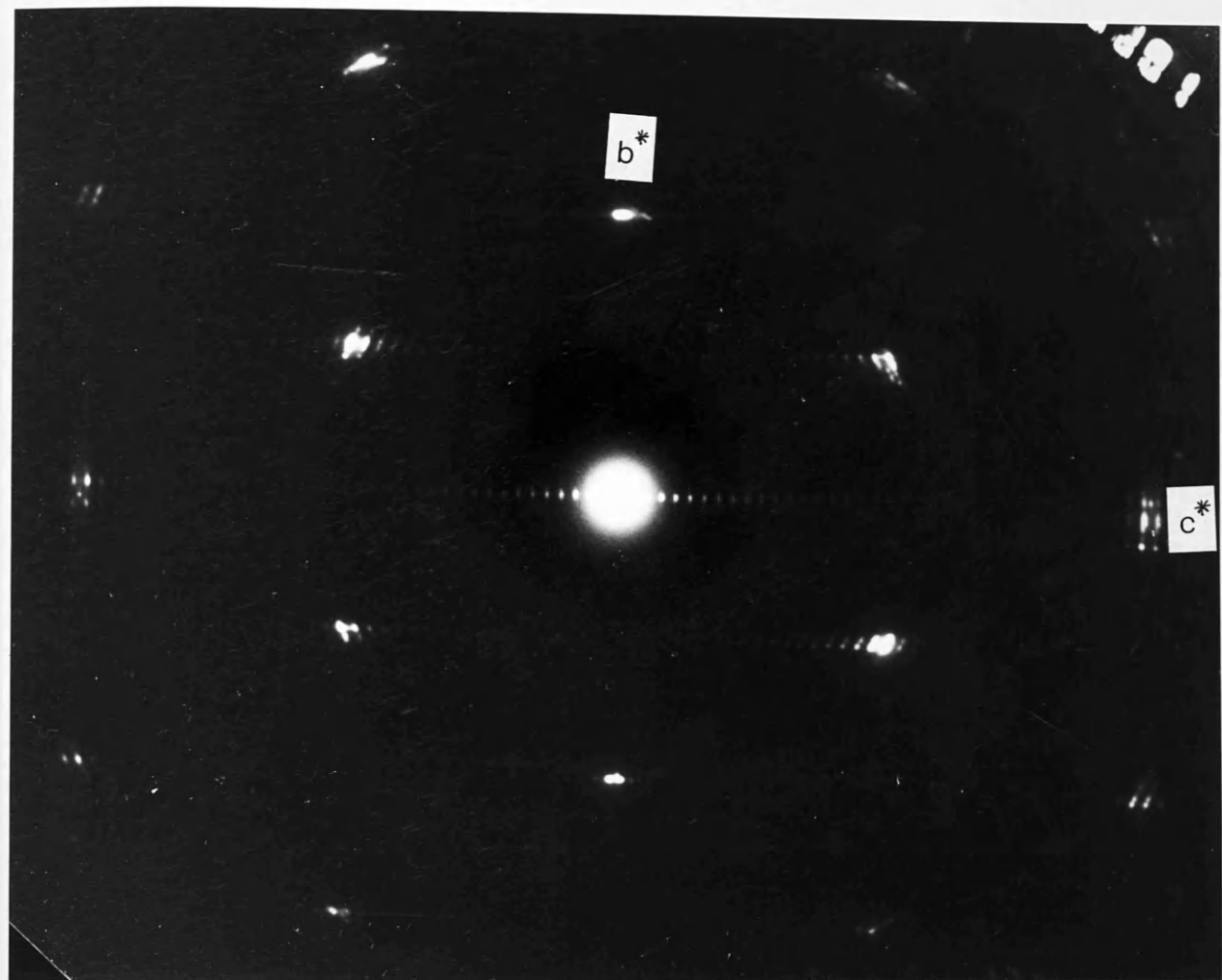
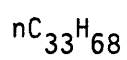


Plate 20 (b) : Electron diffraction pattern of $\text{nC}_{36}\text{H}_{72}$
(0kl orientation).

Plate 21 : Two areas of epitaxially grown crystal of $\text{nC}_{36}\text{H}_{74}$,
taken at 190K, with optical transform.



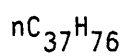
Plate 22 : Epitaxially-grown crystal of a pure paraffin,



x 263,500

Lattice spacing 43.8\AA

Plate 23 : Epitaxially grown crystal of a pure paraffin,



x 310,000

Lattice spacing 48.9\AA

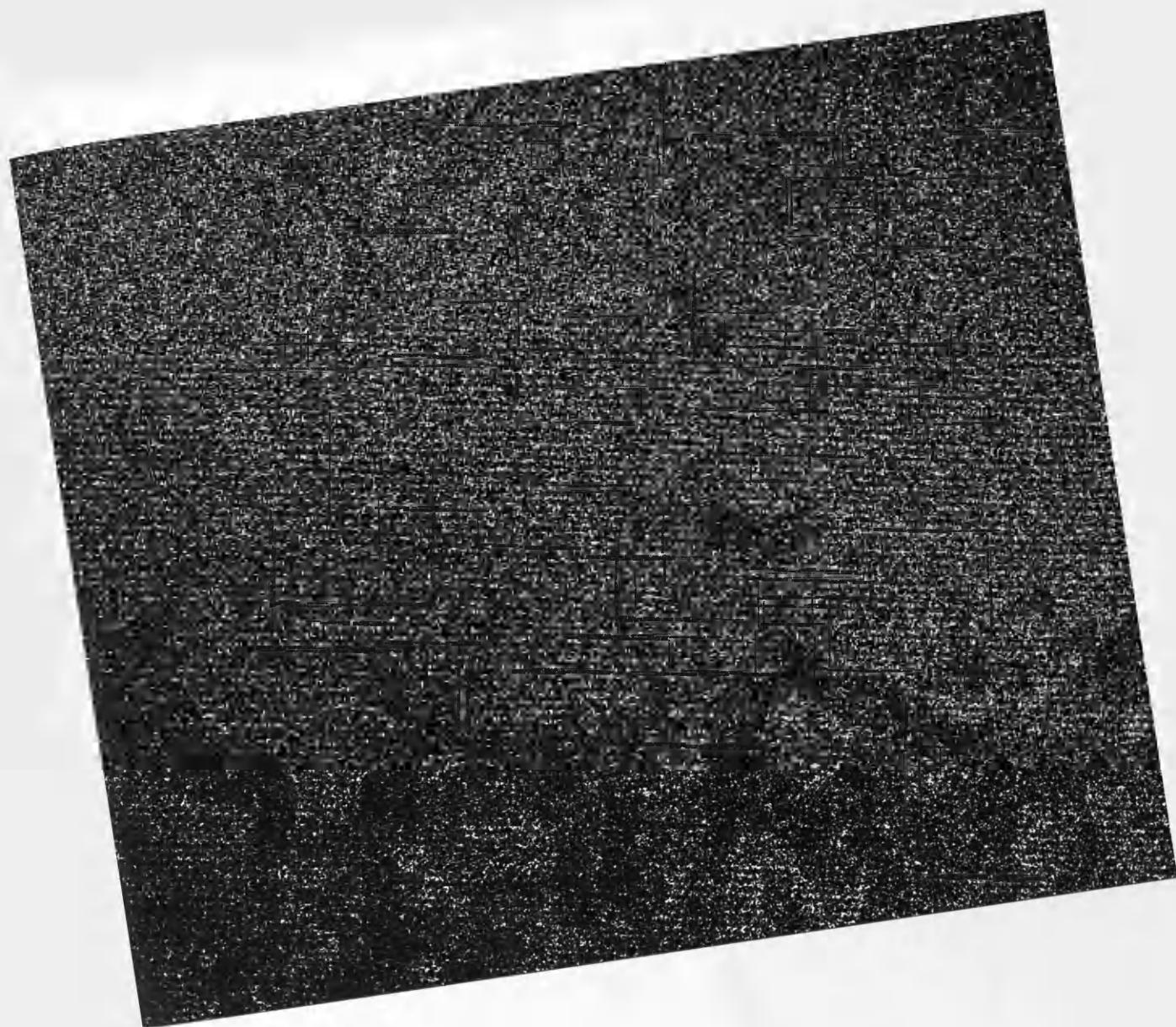


Plate 24 : Epitaxially grown crystal of paraffin solid solution
 C_{37}/C_{38} , mole ratio 1 : 1
x 310,.000

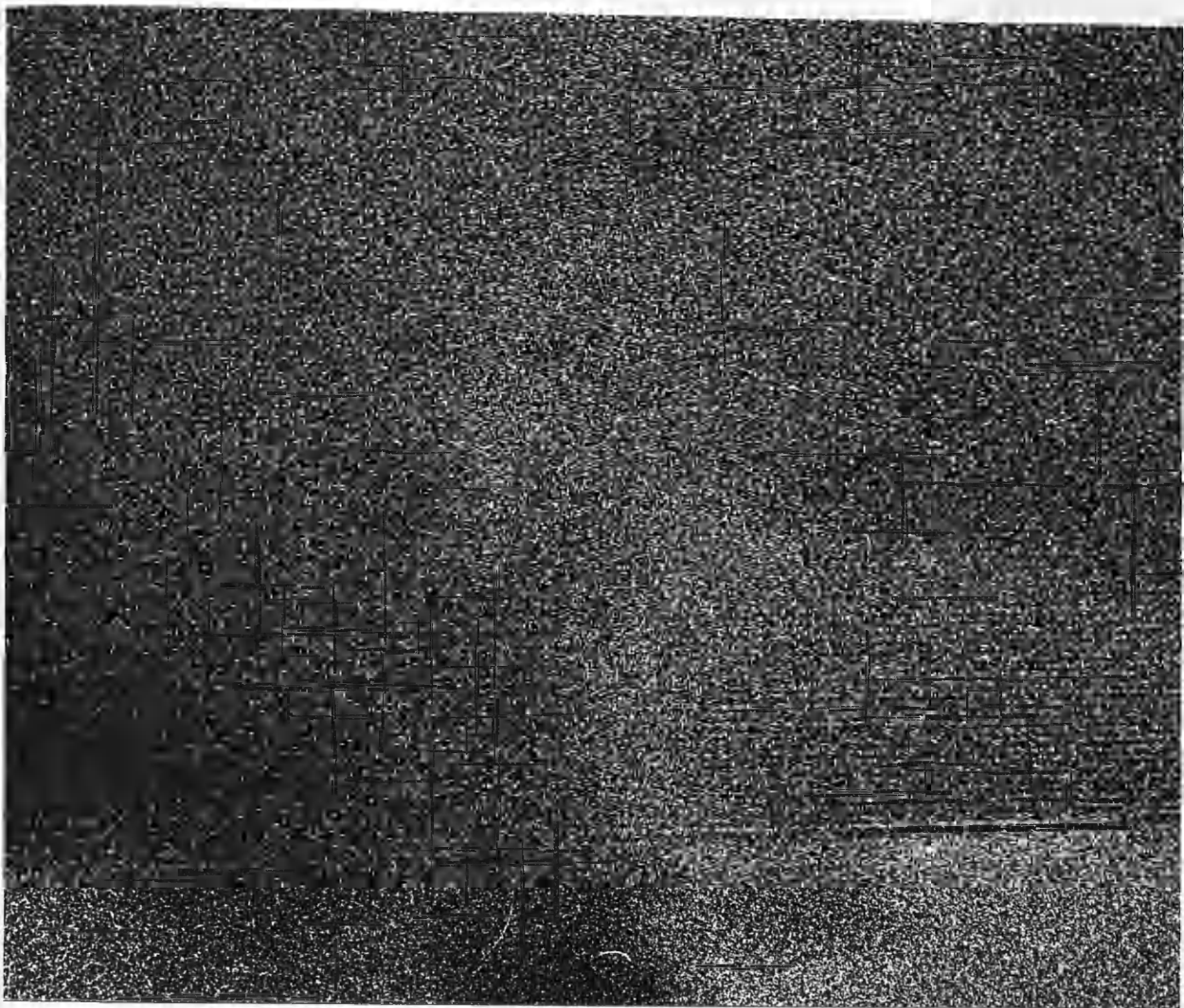


Plate 25 : Epitaxially-grown crystal of paraffin solid solution.

C_{32}/C_{36} , mole ratio 3 : 2
x 310,000

Plate 26 : Epitaxially-grown crystal of paraffin solid
solution.

C_{32}/C_{36} , mole ratio 1 : 1
x 263,500

Plate 27 : Epitaxially-grown crystal of paraffin solid
solution.

C_{32}/C_{36} , mole ratio 1 : 1
x 263,500



Plate 28 : Epitaxially-grown crystal of paraffin solid solution.

C_{32}/C_{36} , mole ratio 2 : 3
x 310,000

Plate 29 : Epitaxially-grown crystal of paraffin solid solution.

C_{32}/C_{36} , mole ratio 1 : 4
x 310,000



Plate 30 : Epitaxially-grown crystal of paraffin solid
solution.

C_{33}/C_{36} , mole ratio 1 : 9
x 102,000

Plate 31 : Epitaxially-grown crystal of paraffin solid
solution.

C_{33}/C_{36} , mole ratio 1 : 9
x 263,500

Plate 32 : Epitaxially-grown crystal of paraffin solid
solution.

C_{33}/C_{36} , mole ratio 1 : 4
x 310,000

Plate 33 : Epitaxially-grown crystal of paraffin solid solution.

C_{33}/C_{36} , mole ratio 1 : 4
x 310,000

Plate 34 : Epitaxially-grown crystal of paraffin solid
solution.

C_{33}/C_{36} , mole ratio 1 : 3
x 263,500

Plate 35 : Epitaxially-grown crystal of paraffin solid
solution.

C_{33}/C_{36} , mole ratio 1 : 1
x 102,000



Plate 36 : Epitaxially-grown crystal of paraffin solid
solution.

C_{33}/C_{36} , mole ratio 3 : 1
x 102,000

Plate 37 : Epitaxially-grown crystal of paraffin solid
solution.

C_{33}/C_{36} , mole ratio 3 : 1
x 263,500

Plate 38 : Epitaxially-grown crystal of paraffin solid
solution.

C_{33}/C_{36} , mole ratio 9 : 1
x 263,500

CHAPTER 8: CONCLUSIONS.

8.1 Radiation Damage.

8.2 The Paraffins.

CHAPTER 8: CONCLUSIONS.

8.1 Radiation Damage.

In the work of Fryer and Holland (1984), a layer of evaporated carbon was found to have a protective effect upon an organic film in the electron microscope at room temperature. Holland (1984) found that the nature of the encapsulating substance had no effect on the protective property; only the peripheral atoms of the specimen surface affect the rate at which the damage occurs. The protection in this case must therefore be regarded as a physical barrier to diffusing fragments rather than as a chemical scavenging effect.

The results obtained and discussed in Chapter 5 of this thesis show no evidence to support this theory. Results at room temperature show local variations in damage-resistance but do not correspond to a clear division between coated and uncoated areas of a single grid. This may be due to variations in thickness or in crystallinity, although it was attempted to choose areas with comparable diffraction patterns.

It has been suggested (Fryer 1982, private communication) that the protective effect of a carbon coat might lessen as the temperature of the specimen stage was lowered and the migration of the severed radicals of the specimen material was inhibited. Cooling the specimen does have a considerable effect on the

lifetime of the specimen under the beam, as many authors have already shown (see Section 2.4) but combining carbon encapsulation and specimen cooling appears to give no additional protective effect, at any temperature. Thus no lessening of protection could be observed as the specimen temperature approached that attainable by cooling with liquid helium.

Cooling of the specimen to liquid helium temperature does increase its lifetime beyond that attainable with liquid nitrogen cooling; however, the relative gain does decrease below 100K, a temperature which can be attained comparatively easily in a microscope stage.

8.2 - The Paraffins.

Images of paraffins crystallised epitaxially in the 0k1 orientation may be recorded at room temperature with sufficient contrast to view directly the interlamellar lattice spacing and the defects occurring in the bc plane. In this study the b-axis was not resolved in this orientation due to the phase contrast transfer function of the microscope which does not permit recording of such widely differing spaces. Further work might enable the conditions to be found whereby the bc face of the crystal might be imaged.

For the $hk0$ projection of the crystal, high resolution imaging requires low-dose, low-temperature conditions but a resolution of 2.48\AA can be detected by optical diffractometry. Densitometry and image processing can extract the information from the micrograph.

More defects are visible in the $0kl$ projection than in the $hk0$; this may be the result of lateral translations of molecules, which leave the $hk0$ projection unchanged. This explanation is supported by solid solution images in which the $hk0$ projection and diffraction pattern appear identical to those of pure paraffins; a void at the chain end plane does not seem to affect the image produced of the $hk0$ projection. Further investigation is required, however, to determine whether and to what extent "lattice defects" in this projection are an artefact of the image processing technique itself.

Lattice images of solid solutions of paraffins show no evidence of fractionation or separation of the two components into distinct crystalline regions, either for even-even or odd-even mixtures.

Features of the crystal for both pure and mixed crystals of paraffins include twinning, bends in the lattices, step-growth and amorphous regions interrupting crystalline areas, which may be screw-type dislocations.

Measurements from lattice images of the changes in interlamellar spacing in solid solutions of different concentrations differ from those obtained by electron diffraction (see Section 7.6). There are too few points on the graph of spacing versus composition to say whether the step-like expansion observed in electron diffraction measurements which occurs here, but there is some evidence of a negative deviation from Vegard's law at low concentrations of the longer molecule, which becomes a positive deviation as the proportion of the longer molecule increases.

- AGAR A. - British Journal of Applied Physics 11 (1960) 5.4.
- AHMED H. - Proc. 25th Anniv. Meeting of EMAG (1971), Inst. Phys. Conference Series No. 30.
- ANDERSON N.G. & DAWSON I.M. - Proc. Roy. Soc. A218 (1953) 255 (Part III).
- ASBACH G.I., GEIGER K. and WILKE W. - Colloid & Polym. Sci. 257 (1979) 1049-1059.
- BAHR G.F., JOHNSON F.B. & ZEITLER E. - Lab. Invest. 14 (1965) 1115.
- BERNSEN P. & REIMER L. - Ultramicroscopy 10 (1981) 199-210.
- BETHE H.A. - Handbook Phys. 24 (1) 1933, Stosstheorie.
- BOVIN J-O, WALLENBERG L.R. & SMITH D.J. - Proc. EMAG 1985: Inst. Phys. Conference Series No. 78.
- BOX H.C. in "Physical Aspects of Electron Microscopy and Microbeam Analysis", Eds. Siegel & Beaman, Wiley 1975.
- BOX H.C. & FREUND H.G. - J. Chem. Phys. 44 (1966) 2345-2348.
- BROCKES A. - Z. Physik 149 (1957) 353.
- BOUDET A. & KUBIN L.P. - Ultramicroscopy 8 (1982) 409-416
- CHIU W., KNAPEK E., JENG T.W. & DIETRICH I. - Ultramicroscopy 6 (1981) 291-296.
- CLARK W.R.K., CHAPMAN J.N., McLEOD A.M. & FERRIER R.P. - Ultramicroscopy 5 (1980) 195-208.
- COSSLETT V.E. - Berichte der Bunsen-Gesellschaft für Phys. Chem. 74 (1970) 1171.
- COSSLETT V.E. - J. Microsc. 113 (2) (1978) 113.
- COWLEY J.M. in "Physical Aspects of Electron Microscopy and Microbeam Analysis" ed. Siegel & Beaman, Wiley 1975.
- DAVISSON C.J. and GERMER L.H. - Phys. Rev. 30 (1927) 705-740.
- DAWSON I.M. & VAND V. - Nature 167 (1951).
- De BROGLIE L. - Phil. Mag. 47 (1924) 446-458.
- DOLE M. (Ed) "The Radiation Chemistry of Macromolecules" - Academic Press (1972)
- DOLE M., KEELING C.D. & ROSE D.G. - J.A.C.S. 76 (1954) 4304.

- DORSET D.L. - Z. Naturforschung 33a (1978) 964-982.
- DORSET D.L. - Acta. Cryst. A36 (1980) 592-600.
- DORSET D.L. - (a) Ultramicroscopy 12 (1983) 19-28
- DORSET D.L. - (b) Z. Naturforschung 38c (1983) 511-514.
- DORSET D.L. - (a) Journal of Electron Microscopy Technique 2 (1985) 89-128.
- DORSET D.L. - (b) Macromolecules 18 (1985) 2158.
- DORSET D.L. - Proc. EMAG, 1985, Inst. Phys. Conf. Ser. 78 411-416.
- DORSET D.L. - Macromolecules 20 (1987) 2782.
- DORSET D.L., MOSS B., WITTMANN J.C. & LOTZ B. (a) - Proc. Natl. Acad. Sci. U.S.A. 81 (1984) 1913-1917.
- DORSET D.L., HOLLAND F.M. & FRYER J.R. (b)- Ultramicroscopy 13 (1984) 305-310.
- DORSET D.L. & ZEMLIN F.- Ultramicroscopy 17 (1985) 229-236.
- DOWNING K.H. - Ultramicroscopy 11 (1983) 229-238.
- DOWNING K.H. & GLAESER R.M. - Ultramicroscopy 20 (1986) 269-278.
- DUBOCHET J., KNAPEK E. & DIETRICH I. - Ultramicroscopy 6 (1981) 77-80.
- EISENHANDLER C.B. & SIEGEL B.M. - J. Appl. Phys. 37 (1966) 1963.
- EGERTON R.F. - "Proc. 25th Scottish Universities Summer School in Physics" 1983 Eds. J.N. Chapman & A.J. Craven (1984).
- EGERTON R.F. - Phys. Stat. Sol. (a) 37 (1976) 663-668.
- EWEN B. , FISCHER E.W., PIESCZEK W. & STROBL G. - J. Chem. Phys. 61 (1974) 5265.
- FRANK F.C. & van der MERWE J.H., Proc. Roy Soc. A198 (1949) 276.
- FRIEDLANDER G., KENNEDY J.W. & MILLER J.M. - "Nuclear and Radiochemistry" Wiley (1964).
- FRYER J.R. - 9th International Congress on Electron Microscopy, Toronto 1978, Vol. 1.
- FRYER J.R. - "The Chemical Applications of Transmission Electron Microscopy", Academic Press 1979.
- FRYER J.R. - Ultramicroscopy 14 (1984) 227-236.

- FRYER J.R. & HOLLAND F.M. - Ultramicroscopy 11 (1983) 67-70.
- FRYER J.R. & HOLLAND F.M. - Proc. Roy. Soc. - A 393 (1984) 353-369.
- FRYER J.R., McNEE C. & HOLLAND F.M. - Ultramicroscopy 14 (1984) 357-358.
- FRYER J.R. & SMITH D.J., Proc. Roy. Soc. A381 (1982) 225-240.
- FUJIYOSHI Y., KOBAYASHI T., ISHIZUKA K., UYEDA N., ISHIDA Y. & HARADA Y. - Ultramicroscopy 5 (1980) 459-468.
- GLAESER R.M. - J. Ultrastructure Res. 36 (1971) 466-482.
- GLAESER R.M. - in "Physical Aspects of Electron Microscopy and Microbeam Analysis" Ch.12, Eds. Siegel & Beaman (1975)
- GLAESER R.M. & TAYLOR K.A. - J. Microsc. 112 (1978) 127-138.
- GRUBB D.T. - J. Mats. Sci. 9 (1974) 1715-1736.
- GRUBB D.T. & GROVES G.W. - Phil. Mag. 24 (1971) 815.
- GRUNDY P.J. & JONES G.A. - "Electron Microscopy in the Study of Materials" Arnold (1976).
- HARTMAN R.S., HARTMAN R.E., ALSBERG H. & NATHAN R. - 8th Int. Cong. on E.M., Canberra 1974, Vol II.
- HAYWARD S.B. & GLAESER R.M. - Ultramicroscopy 4 (1979) 201-210.
- HEIDE H.G. - Lab. Invest. 14 (1965) 1134.
- HEIDE H.G. - Ultramicroscopy 16 (1982) 125-154.
- HENDERSON R. & GLAESER R.M. - Ultramicroscopy 16 (1985) 139-150.
- HENGLEIN A. - Ultramicroscopy 14 (1984) 195-200.
- HIRSCH P.B., HOWIE A., NICHOLSON R.B., PASHLEY D.W. & WHELAN M.J. - "Electron Microscopy of Thin Crystals", Butterworths, 1965.
- HOBBS L. - Proc. of 25th Scottish Universities Summer School in Physics, Glasgow, 1983 Eds. J.N. Chapman and A.J. Craven (1984).
- HOLLAND F.M. - Ph.D. Thesis, University of Glasgow (1984).
- HOLLAND F.M., FRYER J.R. & BAIRD T. - Proc. EMAG (1983) Inst. Phys. Conf. Ser. 61 p.19.
- HOWITT D.G., GLAESER R.M. & THOMAS G. - Proc. 33rd EMSA (1976) 246-247.
- INGRAM P. - Makromol. Chem. 140 (1970) 287.
- INTERNATIONAL EXPERIMENTAL STUDY GROUP - J. Microscopy 141 (1986) 385

ISAACSON M.S. in "Physical Aspects of Electron Microscopy and Microbeam Analysis" Ch. 14, Eds. Siegel and Beaman, Wiley 1975.

JOINT COMMITTEE ON POWDER DIFFRACTION STANDARDS - Powder Diffraction
File 1971. Pennsylvania 1971.

KAY D.H. (ed) "Techniques for Electron Microscopy", 2nd edn.,
Blackwell 1965.

KELLER A. - Phil. Mag. 6 (1961) 329-343.

KITAIGORODSKII A.I. - "Molecular Crystals and Molecules", (vol. 29 of
"Physical Chemistry", gen. ed. E. Loebl),
Academic Press 1973.

KITAIGORODSKII A.I. - "Mixed Crystals" (gen. ed. M Cardona)
Springer-Verlag 1984.

KNAPEK E. & DUBOCHET J. - J. Mol. Biol. 141 (1980) 141-161.

KNOLL M. & RUSKA E. - Ann. der Physik 12 (1932) 607.

KOBAYASHI K. & SAKAOKU K. - Lab. Invest. 14 (1965) 1097.

KOBAYASHI T. & REIMER L. - Bull. Inst. Chem. Res. Kyoto University 53 (2)
(1975) 105.

LADD M.F.C. & PALMER R.A. - "Structure Determination by X-Ray
Crystallography", 2nd ed., Plenum Press 1985.

LEFRANC G., KNAPEK E. & DIETRICH I., Ultramicroscopy 10 (1982) 111-124.

LEPAULT J., DUBOCHET J., DIETRICH I., KNAPEK E. & ZEITLER E. - J. Mol.
Biol. 163 (1983) 511.

MARTINEZ J.P., LOCATELLI D., BALLADORE J.L. & TRINQUIER J. -
Ultramicroscopy 8 (1982) 437-440.

MATTHEWS J.W. (ed) "Epitaxial Growth (Part B)" Academic Press 1975.

MISELL D.L. "Practical Methods in Electron Microscopy" Vol. 7. of
"Image Analysis Enhancement and Interpretation",
gen. ed. A Glauert, North-Holland 1978.

MNYUKH Yu V. - Zh Strukt. Khim 1 (1960) 370.

MÜLLER A. - Proc. Roy. Soc. A124 (1929) 317.

MÜLLER A. - (a) Nature 125 (1930) 952.

MÜLLER A. - (b) Proc. Roy. Soc. A127 (1930) 417-430.

MÜLLER A. - Nature 3255, 129 (1932) 436.

- MÜLLER A. & LONSDALE K. - Acta. Cryst. 1 (1948) 129.
- MURATA Y., FRYER J.R., BAIRD T. & MURATA H. - Acta. Cryst. A33 (1977) 198-200.
- NICHOLSON W.A.P. - J. Microsc. 121 (1981) 141-147.
- NYBURG S.C. & LÜTH H. - Acta. Cryst. B28 (1972) 2992.
- NYBURG S.C. & POTWOROWSKI J.A. - Acta. Cryst. B29 (1973) 347.
- O'DONNELL J.H. & SANGSTER D.F. - "Principles of Radiation Chemistry" - Arnold 1970.
- OHNO T. - Ultramicroscopy 15 (1984) 319-324.
- ORTH H. & FISCHER E.W. - Die Makromol. Chemie 88 (1965) 188-214.
- PIESCZEK W., STROBL G.R. & MALZAHN K. - Acta Cryst. B30 (1974) 1278.
- POWDER DIFFRACTION FILE, Published by the Joint Committee on Powder Diffraction Standards, Pennsylvania, 1960.
- PRADÈRE J.F., REVOL J.F., NGUYEN L. and MANLEY R. St J., Ultramicroscopy 25 (1988) 69.
- REIMER L. - Z. Naturforsch 148 (1959) 566-575.
- REIMER L. - Z. Naturforsch B. 16 (1961) 166.
- REIMER L. - Lab. Invest. 14 (1965) 344-358.
- REIMER L. - "Physical Aspects of Electron Microscopy and Microbeam Analysis" Ch.13., Eds. Siegel & Beaman, Wiley 1975.
- REIMER L. & SPRUTH J. - Ultramicroscopy 10 (1982).
- RETIEF J.J., ENGEL D.W. and BOONSTRA E.G. - J. Appl. Cryst. 18 (1985) 156-158.
- RIGAMONTI R. - Gazz. Chim. Ital. 66 (1936) 174.
- ROBERTS G.G., VINCETT P.S. & BARLOW W.A. - Phys. Technol. 12 (1981) 69-75.
- ROSE A. - J. Opt. Soc. Am. 38 (1948) 196.
- RUSKA E. - Z. Physik 87 (1934) 580-602.
- SALIH S.M. & COSSLETT V.E. - Phil. Mag. 30 (1974) 225-228.
- SALIH S.M. & COSSLETT V.E. - J. Microsc. 105 (1975) 269-276.
- SCHAERER A.A., BAYLÉ G.G. & MAZEE M.M. - Recueil des Travaux Chimiques des Pays-Bas 75 (1956) 513.

- SHEARER H.M.M. & VAND V. - Acta. Cryst. 9 (1956) 379-384.
- SIEGEL G. - Z. Naturforsch. 27a (1972) 325-332.
- SLAGLE F.B. & OTT E. - J.A.C.S. 55.3 (1933) 4404.
- SMITH A.E. - J. Chem. Phys. 21 (1959) 2229.
- SMITH D.J., CAMPS R.A., FREEMAN L.A., HILL R., NIXON W.C. & SMITH K.C.A. - J. Microsc. 130 (2) (1982) 127-136.
- SPENCE J.H.C. - "Experimental High Resolution Electron Microscopy", Clarendon Press, 1981.
- STROBL G., EWEN B., FISCHER E.W. & PIESCZEK W. - J. Chem. Phys. 61 (1974) 5257.
- SYMONS M.C.R. - Ultramicroscopy 10 (1982) 15-24.
- TAYLOR C.A. & LIPSON H. "Optical Transforms - their Preparation and Application to X-ray Diffraction Problems", G. Bell & Sons 1964.
- TEARE P.W. - Acta. Cryst. 12 (1959) 294.
- TOMITA M., HASHIMOTO H., IKUTA T. ENDOH H. and YOKOTA Y - Ultramicroscopy 16 (1985) 9-18.
- UEDA R. & MULLIN J.B. (ed) - "Crystal Growth and Characterisation", Proceedings of the I.S.S.C.G. 2nd Spring School, Japan 1974, North-Holland 1975.
- UNWIN P.N.T. & HENDERSON R. - J. Mol. Biol. 94 (1975) 28.
- UYEDA N., KOBAYASHI T., SUITO E., HARADA Y. & WATANABE M. - J. Appl. Phys. 43 (1972) 5181-5188.
- UYEDA N., MURATA Y. & SUITO E. - Electron Microscopy 1 (1974) 692.
- VAINSHTAIN B.K. - "Structure Analysis by Electron Diffraction", Pergamon 1964.
- VAND V. - Acta. Cryst. 4 (1951) 104.
- VEGARD L. & DALE H. - Z. Krist. 67 (1928) 148.
- VENABLES J.A. & BASSETT D.C. - Nature 214 (1967) 1107.
- VESELY D. - Ultramicroscopy 14 (1984) 279-290.
- WADE R.H. - Ultramicroscopy 14 (1984) 265-270.
- WATT I.M. - "The Principles and Practice of Electron Microscopy", Cambridge University Press 1985.

WEST A.R. - "Solid State Chemistry and its Applications" Wiley 1984.

WILLIAMS R.C. & FISHER H.W. - J. Mol. Biol. 52 (1970) 121-123.

WITTMANN J.C., HODGE A.M & LOTZ B. - J. Polym. Sci. (Polym. Phys.)
21 (1983) 2495.

WITTMANN J.C. & LOTZ B - Proc. EMAG 1985, Inst. Phys. Conf. Ser. 78

WITTMANN J.C. & MANLEY R. St. J., J. Polym. Sc. (Polym. Phys.) 16 (1978)
1891-1895.

ZEITLER E. - Ultramicroscopy 10 (1982) 155-164.

ZEMLIN F., REUBER E., BECKMANN E., ZEITLER E. and DORSET D.L. -
Science 229 (1985) 461.

Direct lattice imaging of crystalline paraffins

*C H McConnell, * J R Fryer, **D L Dorset, ***F Zemlin

*University of Glasgow, Glasgow G12 8QQ. **Medical Foundation of Buffalo, Inc, 73 High Street, Buffalo, N.Y. ***Fritz-Haber Institut, Faradayweg 4-6. 1000 Berlin 33.

Introduction

Paraffins provide an interesting series of specimens for electron microscope studies, being in effect short-chain polymers and in some ways analogous to lipids and other biological substances. The structures of the different polymorphs of various paraffins have been determined by X-ray diffraction methods (Shearer and Vand 1955, Teare 1958) and the spiral growth of the $\text{nC}_{36}\text{H}_{74}$ crystal from solution was studied by electron microscopy by Dawson and Vand (1950).

Aliphatic hydrocarbons are extremely beam-sensitive, but it has been proved possible to obtain structural images of monolamellar crystals of $\text{nC}_{44}\text{H}_{90}$ at a resolution of 0.25nm using a low-dose technique (Zemlin et al 1985). The 001 lattice of $\text{C}_{36}\text{H}_{74}$ was imaged by Fryer, 1981.

In the present work, paraffins of various chain lengths were crystallised in two orientations, allowing lattice images to be made of the lamellar spacings as well as of the orthogonal (001) projection of the chain packing.

1. The hk0 Orientation.

Single, monolayer paraffin crystals grown from hexane solution were recorded in the hk0 orientation using the helium-cooled superconducting microscope at the Fritz-Haber-Institut, Berlin. Chain-lengths studied were $\text{C}_{82}\text{H}_{166}$, $\text{C}_{60}\text{H}_{122}$, $\text{C}_{44}\text{H}_{90}$ and $\text{C}_{36}\text{H}_{74}$, plus an example each of an odd-even and an even-even solid solution. Low magnification images of the lozenge-shaped crystals, grown from solution, of long-chain paraffins show striations in the $\langle 130 \rangle$ direction, as well as sectorisation similar to that observed with polyethylene (Dorset, 1985(b), Bassett and Keller, 1962).

To investigate this effect further, images were recorded with a magnification of 60,000X, using a minimum dose technique and with the specimen cooled to 15K. It was found that a satisfactory image could be obtained applying an electron dose of $12\text{e}^-/\text{\AA}^2$ to the specimen. It has been found that under these conditions, at 2.5Å resolution, the diffraction intensities which contribute to the image do not change their relative intensity until beyond $14\text{e}^-/\text{\AA}^2$ (Dorset and Zemlin, 1985).

The electron diffraction pattern of C_{36} in fig.1 is characteristic of all

the paraffins. A low-dose image is also shown (fig.2). The periodic information cannot be seen by eye but the light optical diffraction pattern (inset) shows a resolution of 2.5 \AA .

Selected areas of the micrographs were enlarged by a factor of 5, then digitised using a flat-bed Datacopy microdensitometer with a 25μ aperture. The images were then filtered using the "IMAGIC" programme of van Heel, (1981). A filtered image is shown in fig.3. Variations in contrast seem to indicate small changes in the surface structure of the crystal about 4 nm apart, although these are too small to account for the $\langle 130 \rangle$ striations, the cause of which is still under investigation. As is expected, the filtered images in this projection of the solid solutions are similar to those of the pure compounds.

2. Epitaxially Crystallised Solid Solutions.

The formation of solid solutions by crystallising two different chain lengths together in certain proportions has been reviewed by Mnyukh (1960) who stated the following conditions for their formation:

- (a) The form and dimensions of the two components must be similar. In the case of paraffins the chains must be nearly the same length.
- (b) The symmetry of the binary crystal structure must be the same as or lower than that of the pure component crystals.

Series of solid solutions of paraffins have been studied by Dorset (1985 a and b) who has constructed melting and freezing point curves to show that while the restriction on chain length difference appears to hold for the formation of true solid solutions, it is possible to combine a paraffin with an even number of carbon atoms in the chain with one with an odd number to make a solid solution. This is because the polymorphs involved are similar high energy crystal forms; fractionation is expected in the lowest energy forms, however.

In order to see the chain length directly, the 001 plane of the paraffin crystal must be projected on to the image screen. This is achieved by epitaxial crystallisation on benzoic acid, as described by Wittmann et al, (1983). Images were recorded using a JEOL 100B microscope at room temperature keeping the electron dose very low and using the dark field deflector switch to focus on an area of crystal adjacent to the one to be photographed. The paraffins chosen were C_{32}/C_{36} and C_{33}/C_{36} solid solutions in various proportions, as examples of even-even and odd-even solutions. Images were recorded with a magnification of 17,000X and their 001 spacings measured by optical diffraction, which in some cases extended to 3rd order. An example is shown in fig.4 of a 9:1 solution of $C_{33}H_{68}$ and $C_{36}H_{74}$, along with its optical diffraction pattern. Fig.5 (a and b) shows graphs of the observed spacings against the proportion of the larger component. The results appear to support Dorset's observation of continuous solution formation. For C_{32}/C_{36} the chain lengths lie above the straight line joining the values for the two pure components. It appears that the longer chain dominates and incorporates the shorter at all ratios. With the C_{33}/C_{36} system the results lie around the line, but because of the rather coarse sample of this curve, further work with intermediate compositions is needed to give a better indication of the behaviour of these solutions.

The images, once filtered, show defects in the lattices (fig.6). Pairs of defects are common, and the lattices are seen to bend to accommodate the strain. Some areas of crystal appear quite free of defects, but the concentration of defects does not appear to change much with the composition of the solid solution.

Conclusion

The above results show that important information about lattice defects and crystal texture can be directly obtained by electron microscopy from such beam-sensitive materials as the paraffins. So far we have examined both pure and polydisperse systems as a model of polyethylene crystal packing and anticipate future work of this kind on microcrystals of the polymer itself.

Thanks to the National Science Foundation, U.S.A. who partially supported this work (DMR81-16318) and to SERC for grant support (CHM).

References

- Bassett, D.C. and Keller A, Phil. Mag. 7th Series (1962) 1553.
 Dawson, I.M. and Vand V, Proc.Roy.Soc. 206A (1951) 555.
 Dorset, D.L. 1985 (a) Macromolecules (in press)
 Dorset, D.L. 1985 (b) These proceedings.
 Dorset, D.L. and Zemlin, F. Ultramicroscopy 1985 (in press).
 Fryer, J.R. Inst. Phys.Conf. Ser 61 EMAG 1981.
 Mnyukh, Yu V. J.Struct. Chem. (USSR) 1 (1960) 346.
 Shearer, H.M.M. and Vand, V. Acta.Cryst. (1956) 9 379.
 Teare, P.W. Acta.Cryst. (1959) 12 294.
 Van Heel, M and Keegstra, W. Ultramicroscopy 7 (1981) 113.
 Wittmann, J.C. ; Hodge, A. and Lotz, B. J.Polym.Sci(Polym.physics) 21 (1983) 2495.
 Zemlin, F.; Reuber, E.; Beckmann, E.; Zeitler, E. and Dorset, D.L. Science 229 (1985) 461.

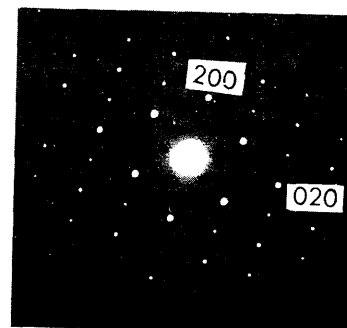


Fig. 1
Electron diffraction pattern of $hk0$ projection of $nC_{36}H_{74}$

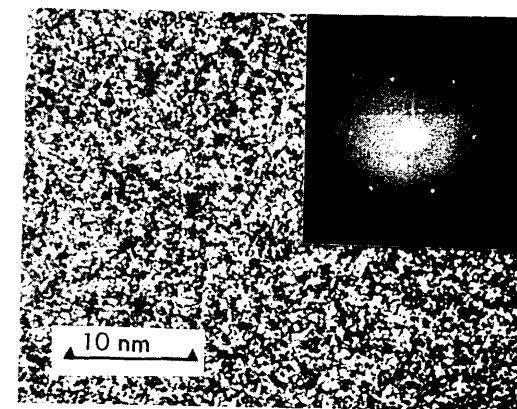


Fig. 2
Low-dose image of $hk0$ projection of $nC_{36}H_{74}$ with optical transform, showing 020 reflection.

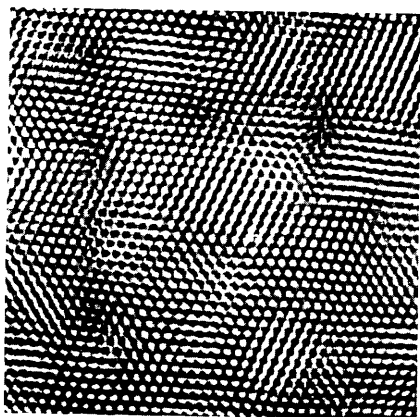


Fig.3 Filtered image of hk0 projection

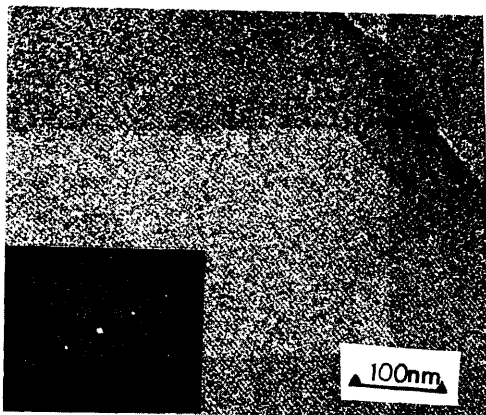


Fig.4 9:1 solution of C_{33}/C_{36}

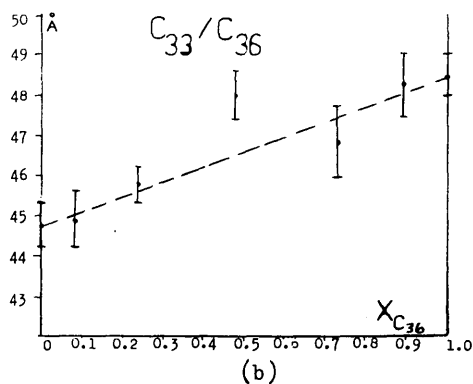
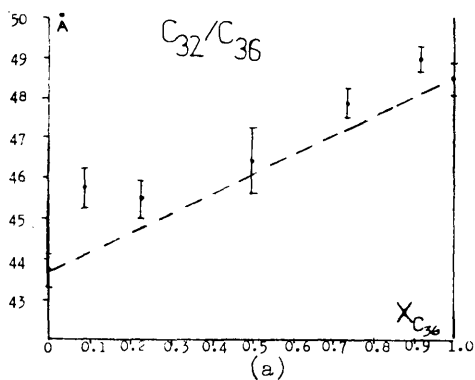


Fig.5 (a) and (b) 001 lattice spacing of solid solutions, plotted against mole fraction of $C_{36}H_{74}$

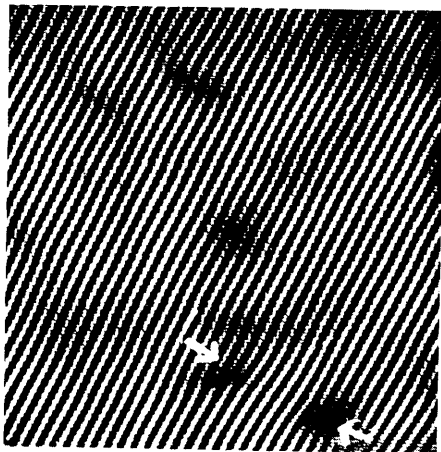


Fig.6 Filtered image of a solid solution, with defects

ELECTRON DIFFRACTION AND IMAGING OF EPITAXIALLY GROWN CRYSTALS OF MONO-GALACTOSYLDIACYLGLYCEROL

A. Sen*, E.L. Hurley*, S.W. Hui*, D.L. Dorset** and C.M. McConnell**

*Roswell Park Memorial Institute, Buffalo, New York 14263

**Medical Foundation of Buffalo, Buffalo, New York 14203

The molecular structure of 1,2-3-distearyl-monogalactosyldiacylglycerol (MGDG) was studied by electron microscopy and electron diffraction. MGDG was extracted from spinach leaves, purified and hydrogenated to a distearate compound. Crystals of MGDG were obtained in two orientations. Thin crystals grown from solutions by evaporation of non-polar solvent on the carbon coated grid showed the long axis of the molecules nearly perpendicular to the carbon film substrate. The acyl chains were packed in a hexagonal lattice commonly found in phospholipid crystals. In order to study the structure along the long axis of the molecule, an epitaxial method of crystal growth (1) was used to obtain crystals with the long axis of the molecule parallel to the carbon substrate. Epitaxial crystals were grown from solutions in naphthalene or benzoic acid on 400 mesh, carbon coated grids. After crystallization of the lipid, which is directed by the cooled aromatic substrate by lattice matching, naphthalene and benzoic acid were removed by sublimation under high vacuum. The epitaxial crystals were coated with a thin layer of carbon. The grids were examined in JEOL 100B electron microscope.

Crystals of MGDG of various thicknesses were observed. Electron diffraction patterns were obtained from thinner areas. Diffraction patterns were recorded on Kodak DEF-5 x-ray film. Regions which showed good diffraction patterns were photographed using low dose imaging techniques. The average dose per recording each image or diffraction pattern was below 10 electrons/nm².

The image of the crystals show periodic patterns with repeating electron light and dense lines (figure 1). The optical diffraction pattern of a region straddling two adjacent crystallites is shown in figure 2. The electron diffraction patterns obtained (figure 3) showed lamellar structures with repeat distance of 5.4 nm which agrees very well with previous x-ray diffraction studies of unoriented samples. Patterson function for the epitaxial crystals are determined from the measured intensity of electron diffraction patterns which have 12 to 15 orders of reflections. The phases of the reflections are determined either by model building or by the inverse Fourier transform of the image. The result yields an atomic density profile across the bilayer. This work demonstrates the use of the electron crystallography technique to study the molecular structure of lipids.

Reference

- (1) Dorset, D.L., Pangborn, W.A. and Hancock, A.J., *J. Biochem. Biophys. Methods* **8**, 29-40 (1983).

Electron micrograph of an area containing two differently oriented MGDG crystals epitaxially grown on naphthalene. Line spacing 5.4nm

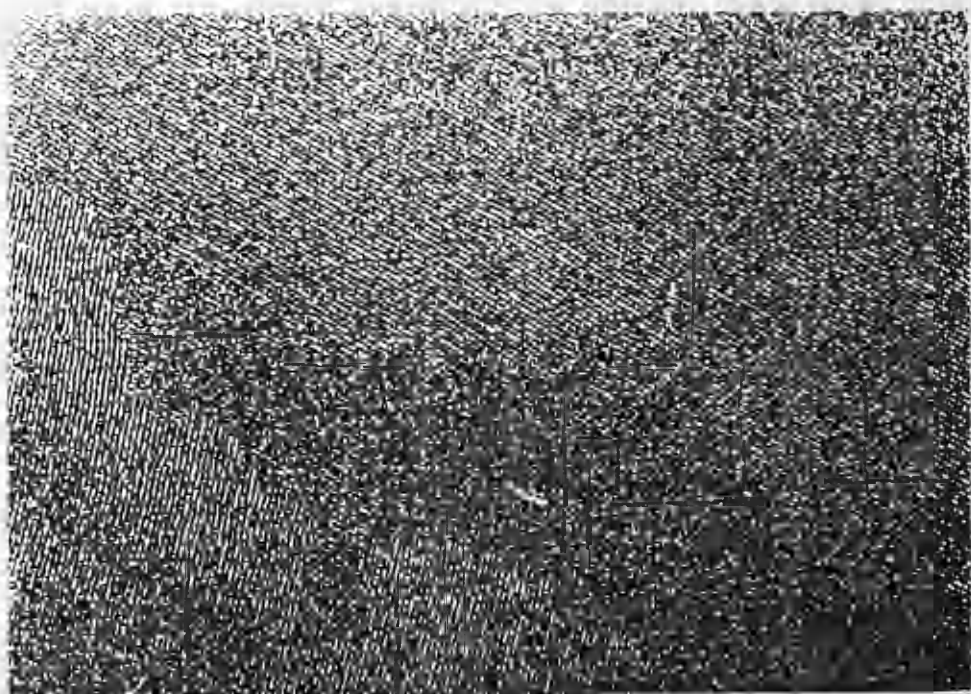


Figure 2. Optical diffraction pattern from electron micrograph of two adjacent MGDG crystals.

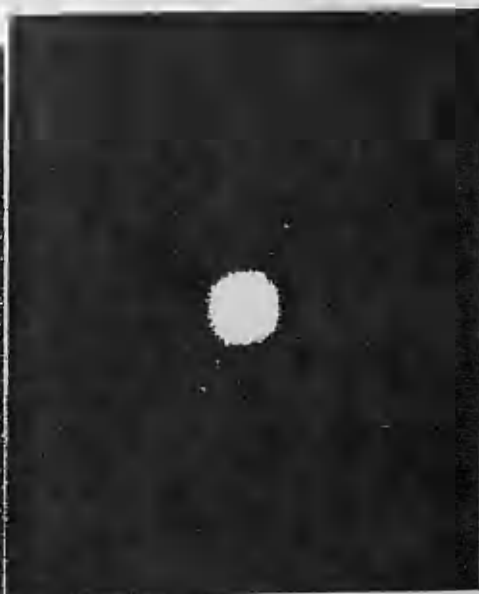


Figure 3. Electron diffraction pattern of an area containing two adjacent MGDG crystals epitaxially grown on naphthalene.